PhD Thesis

School of Chemistry

Cardiff University

DFT Investigation of the mechanism of hydrogenation by borenium based chiral FLPs

Thesis submitted in accordance with the requirements of the

Cardiff University for the degree of doctor in philosophy by:

Gitanjali Sharma

2020

Dedicated to my Family

ACKNOWLEDGMENT

At the outset I would like to thank my supervisor Dr James Platts. I am indebted to him for providing his guidance, advice and support during entire tenure of my PhD, that helped me to carry my research without any interruption.

I would like to thank Prof Peter Knowles and Dr Emma Richards for their periodical mentoring and advice that was very beneficial for me to keep track of my thesis. I would also like to thank Dr Paul Newman and Dr Rebecca Melen, who acquainted me with some new facets of FLP chemistry.

Thanks are due to administrative staff of chemistry department for always providing help and support.

Last but not the least I would like to thank my family for their continuous love, support, and prayers throughout my research that helped to cope any situation.

Publications in Support of Thesis

1. Computational design of an intramolecular frustrated Lewis pair catalyst for enantioselective hydrogenation, Journal of Theoretical and Computational Chemistry, 19, 2, 2050009-1, DOI: 10.1142/S0219633620500091.
2. G. Sharma, P. Newman and J. Platts, Journal of Molecular Graphics and Modelling, 2021, 105, 107846, DOI:10.1016/j.jmgm.2021.107846.

Abstract

In this thesis, hydrogenation of olefins and carbonyl compounds by borenium compounds based on camphor scaffolds “Frustrated Lewis Pairs” (FLPs) has been investigated using density functional theory. FLPs provide a novel substitute to the conventional catalysts that are quite expensive and sometimes toxic. The main aim of the present study was to design some new FLPs employing main group elements, as sustainable alternatives to transition metal catalysts for industry. The study has been done in three phases. The first part of the thesis (Chapter-3) deals with the design of chiral intramolecular FLPs. During this study various methods in DFT have been screened to find the most suitable method. M06-2X/6-31G(d) level of theory has been utilized to study the newly designed FLPs. The most stable FLPs were then selected for further studies. In the second part (Chapter-4) selected FLP systems were explored as possible catalyst for the hydrogenation of small achiral molecules of olefins and carbonyl compounds. The results demonstrated that the activation barriers for these reactions were quite moderate. In the third part of the study (Chapter-5), FLPs were used to study the hydrogenation of some prochiral olefins and carbonyls. Stereochemistry of these reactions was also investigated to understand the stereochemical preferences towards the substrate. The results indicated that the FLPs indeed have preference for specific face of the substrate. These observations open up a possibility of further exploration of FLPs for preparation of industrially useful chiral compounds by hydrogenation of prochiral substrates.

Contents

Chapter-1 Literature Survey

In 1923, G. N. Lewis proposed a generalized definition of the acid-base behaviour. Lewis acid is any species (molecule or ion) that can accept a pair of electrons, and a Lewis base is any species (molecule or ion) that can donate a pair of electrons. Lewis base donates a pair of electrons to Lewis acid to form a Lewis acid-base adduct, a compound that contains a coordinate covalent bond between the Lewis acid and the Lewis base. Frustrated Lewis Pairs (FLPs) are a category of sterically encumbered inter- or intra-molecular Lewis-acid/Lewis-base pairs that are not able to form classical adducts due to their size or electronic factors.

The inability of sterically overcrowded Lewis pairs to form classical adducts has been known since 1942 when Brown[1] and co-workers (Scheme 1.1) reported that lutidine formed an adduct with BF_3 but not with the less Lewis acidic and bulkier $B(CH_3)_3$.

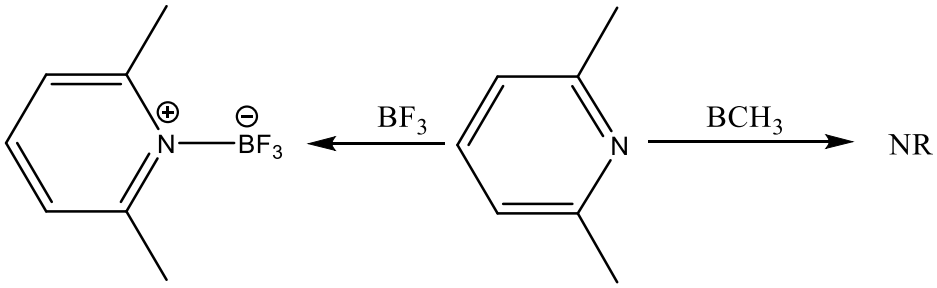

Scheme 1.1 Reaction of lutidine with Lewis acids.

In 1959 Wittig and Benz[2] (Scheme 1.2) found a PPh_3/BPh_3 pair that did not form classical adduct on mixing but were able to undergo 1,2-addition reactions by *in situ* generated benzyne and also showed that the $[CPh_3]^-/BPh_3$ pair adds to butadiene.

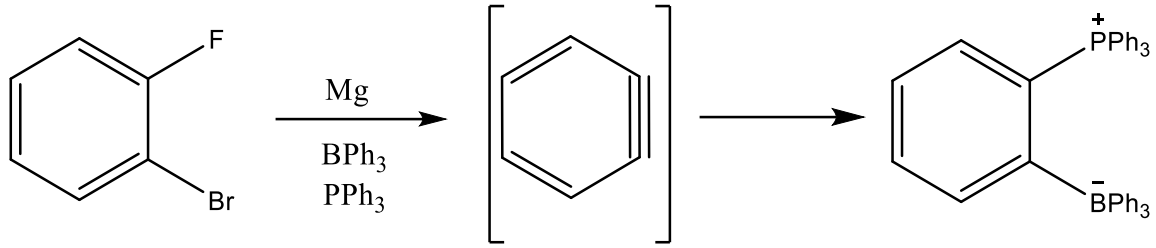

Scheme 1.2 1,2-Addition reaction of BPH_3/BPh_3 pair with benzyne.

In 1966 Tochtermann[3] (Scheme 1.3) observed that on addition of BPh_3 to a butadiene monomer/ triphenylmethane anion mixture, instead of a classical Lewis adduct, a trapped product was obtained upon the addition of BPh_3 and Ph_3CNa to butadiene. He described these systems as 'Antagonistisches Paar' meaning antagonistic pair.

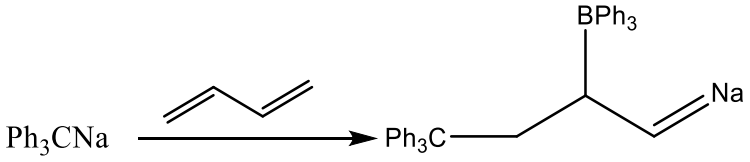

Scheme 1.3 Addition of BPh_3 to a butadiene monomer/ triphenylmethane anion mixture.

In 1996 Piers[4] reported $B(C_6F_5)_3$-catalysed hydrosilylation of ketones which is considered as the first example of Frustrated Lewis Pair (FLP) chemistry. Although discovered very early, it was not until 2006 that unprecedented reactivity of FLPs was uncovered by Stephan and his group (Scheme 1.4). They reported intra[5]- as well as inter[6]-molecular FLPs that were able to split dihydrogen.

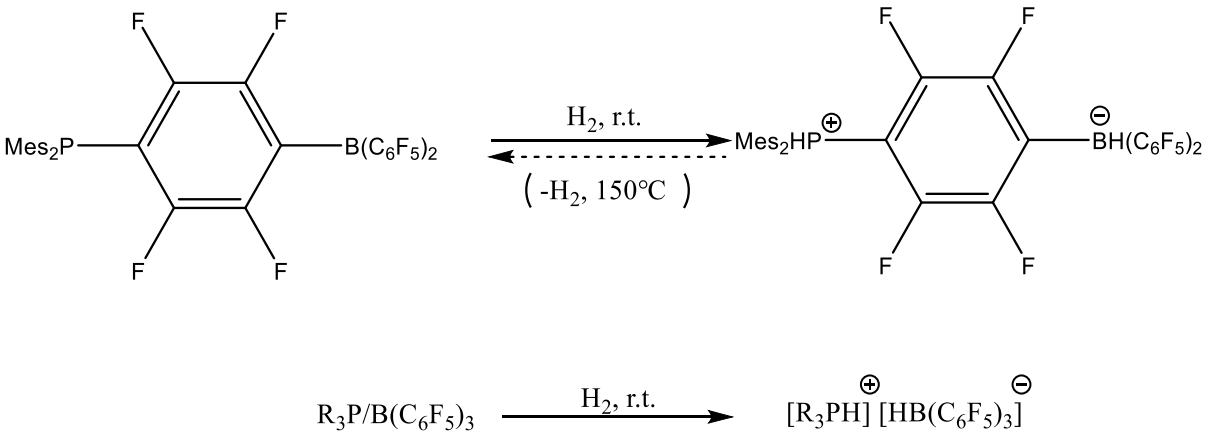

Scheme 1.4 Splitting of dihydrogen by intra- and intermolecular FLPs.

For effective heterolytic cleavage of dihydrogen and other small molecules FLP design included a combination of sterically crowded strong Lewis acid and Lewis base where steric demands prevented the classical adduct formation. The term FLP was also coined by Stephan[7] and co-workers in 2007. Since then, a lot of work has been reported on FLPs but the remainder of this chapter reviews recent efforts to use theoretical methods, usually but not exclusively based on density functional theory (DFT) to model FLP chemistry, focussing mainly on transformations that are catalysed by different classes of FLP. The theoretical basis of DFT will be covered in Chapter 2.

1.1 Theoretical Studies of Hydrogenation by FLPs

Mane[8] and co-workers (Figure 1.1) have studied FLP catalysts used for hydrogenation of unsaturated compounds. They have done computational investigations which may help to make them more efficient by reducing the frustration, steric demand and acid/base strength i.e. Less Frustrated Lewis Pairs (LFLPs). They have employed M06-2X/TZVP//PBE-D3/TZVP approach for studying this new generation of FLPs. Studies of hydrogenation of unsaturated compounds indicate that turn over

frequencies (TOF) are significantly increased if LFLPs are used instead of FLPs though sometimes unwanted side reactions may be present if steric demand is reduced without reducing the frustration.

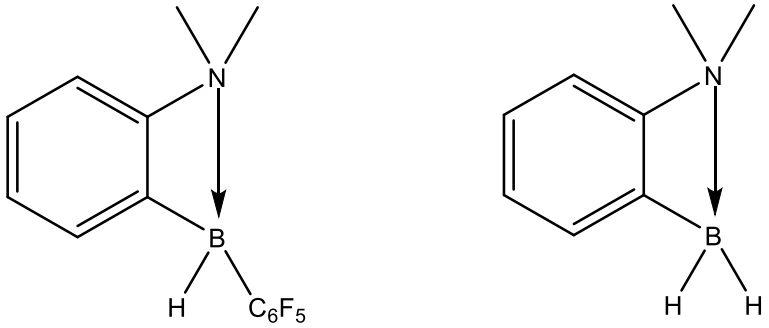

FLP LFLP

Figure 1.1 LFLP (and its corresponding FLP for comparison) used in this study.

Dong[9] and co-workers have reported dialkylsilylenes (Figure 1.2) that behave like an FLP when combined with either Lewis acid or Lewis base due to the amphoteric nature of silylene. Feasibility of the proposed mechanism was checked by comparing the relative energies of the intermediates and products at the M06-2X/6-311+G(d,p) level. Studies reveal that the new FLP can split dihydrogen successfully. Although the dihydrogen step is slightly endothermic but the final step involving the formation of the product is exothermic.

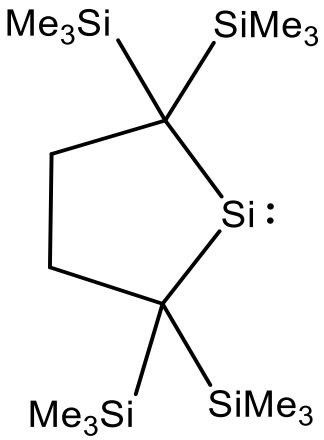

Figure 1.2 Dialkylsilylene used in this experiment that behaves like an FLP when combined with either Lewis acid or Lewis base.

Dorko[10] and co-workers have synthesized and studied a series of triaryl-boranes with a general BX_2Y (Figure 1.3) structure for FLP hydrogenation. They have characterized these molecules exhaustively and by substituting meta- and para-hydrogen atoms to fluorines or chlorines too using experimental and theoretical techniques. Hydrogen ion affinities of these molecules were calculated using B3LYP-D3/6-311G(d,p) level and then compared with experimental results. Single point energy calculation for each localized structure was done on B3LYP-D3/6-311++G(3df,3pd) level. Results indicate that although Lewis acidity increased on replacing hydrogen to fluorine in meta-positions, however it negligibly changed on hydrogen to chlorine replacement.

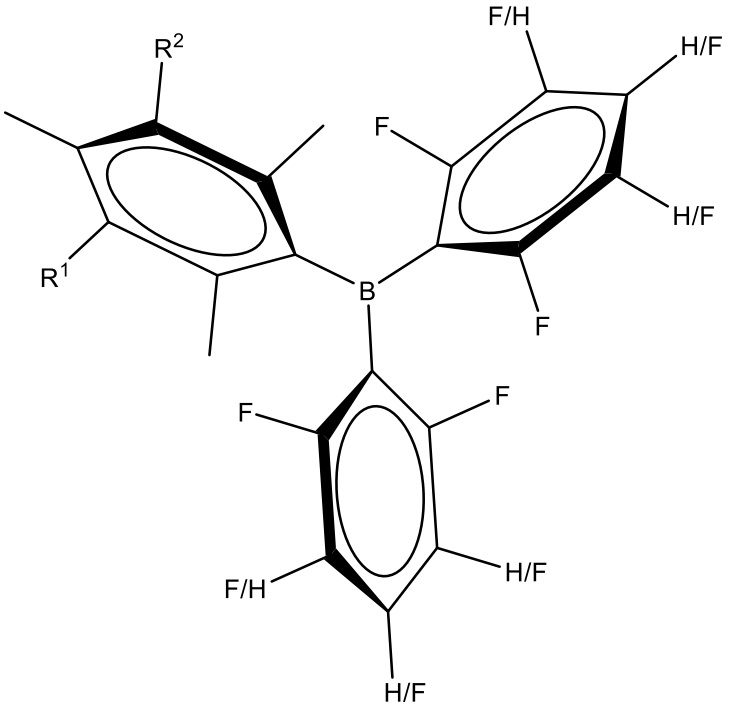

Figure 1.3 General structure of the triarylboranes studied.

Chernichenko[11] and co-workers have reported some novel 2-(Dialkylamino) phenylboranes containing BXZ group (Figure 1.4), where X, Z = C_6F_5, Cl, H, which are able to cleave H_2 under mild conditions. Their computational studies using DFT (ωB97X-D/6-311G(d,p) level) reveal that FLPs having boron attached with C_6F_5 or Cl group have activation barriers much lower than if it were attached with a hydrogen which may be attributed to the stabilization acquired due to dimerization in the first two

cases.

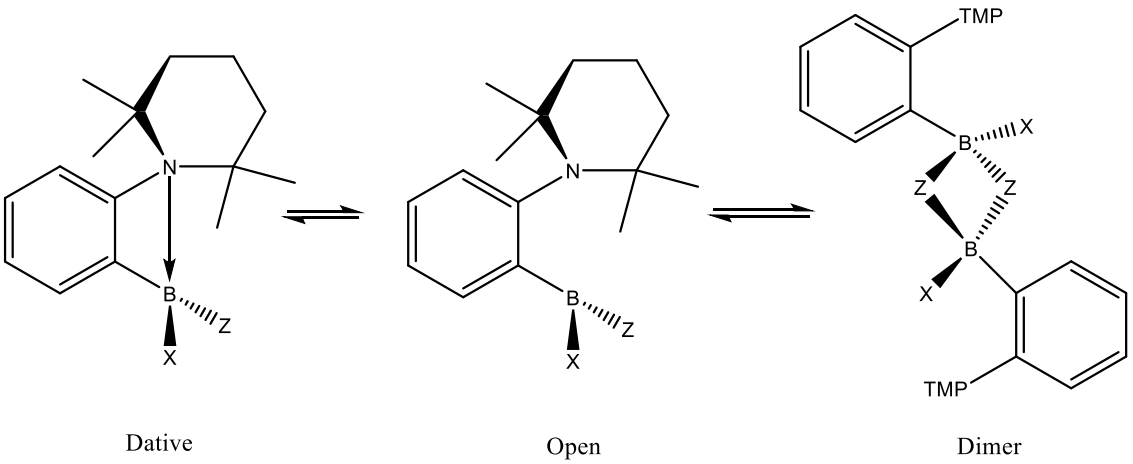

Figure 1.4 2-(Dialkylamino)phenylboranes containing BXZ group that may exist in dative, open or dimer form.

DFT based metadynamics (DFT-MD) study[12] have been done on DFT-D level of theory to map free energy surface (FES) at finite temperature which in turn helped to map out lowest energy pathway for hydrogen activation by FLPs ($tBu_3P/B(C_6F_5)_3$ in particular) (Scheme 1.5). The results obtained by dynamics study are different from the static calculations. While the results of earlier static DFT calculations have predicted the role of FLP to provide strength to cleave the H−H bond in a cooperative way, the dynamics suggest that after initial polarization hydride transfer to boron (which is rate determining step of the reaction) and proton transfer to phosphorus occurs by electron transfer.

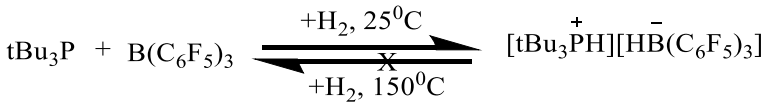

Scheme 1.5 Hydrogen activation by $tBu_3P/B(C_6F_5)_3$ FLP.

Rochette[13] and co-workers have reported reduction of hydroborane (Scheme 1.6) in a dimer formed by crystallization of ansa-aminohydroborane $1\text{-}NMe_2\text{-}2\text{-}(BH_2)\text{-}C_6H_4$ without usage of any catalyst. ωB97XD/6-31++G** level of theory with solvation model based on density (SMD) model of toluene solvent has been utilized to delineate the mechanism of this transformation. Results indicate that it is the FLP moiety in the dimer which activates the B-H bond and thus leads to synchronous formation of B-B bond of diborane and expulsion of H_2 on heating.

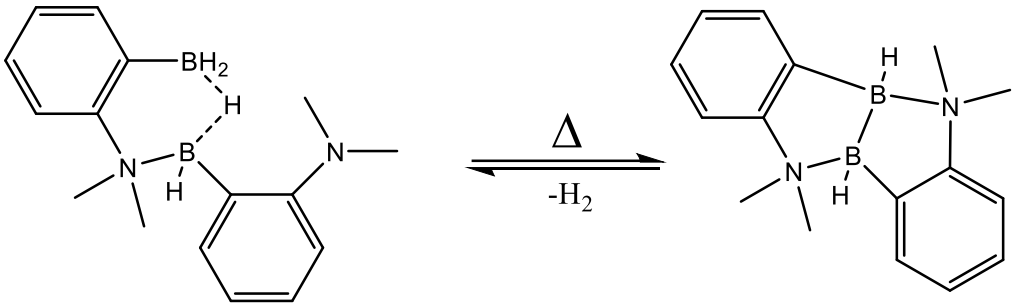

Scheme 1.6 Reduction of hydroborane in a dimer formed by ansa-aminohydroborane.

Courtemanche[14] and co-workers have reported an unusual multidentate FLP [bis(2-(TMP) phenyl] chloroborane (TMP = 2,2,6,6-tetramethylpiperidine) (Scheme 1.7) which reacts with H_2 to form a zwitterionic intermediate reversibly. This further releases HCl to form another novel FLP Bis(2-(TMP)phenyl) borane. ωB97XD functional along with 6-31G** basis set was used. It has been found that the new FLP is quite efficient in activation of dihydrogen. It has also been shown that the isomer in which proton directly faces hydride is more endergonic as compared to the crystallized one.

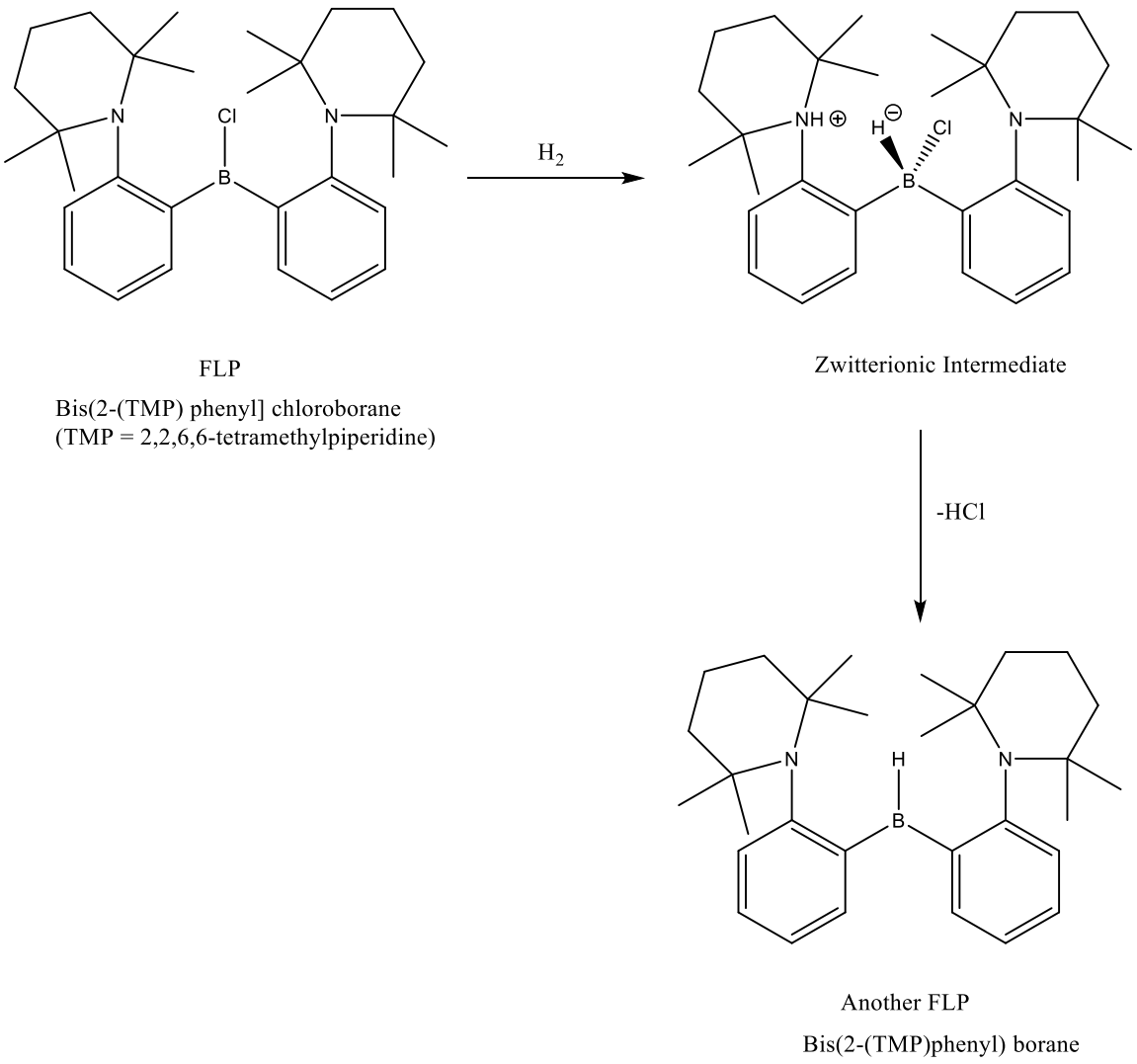

Scheme 1.7 Hydrogen activation by bis(2-(TMP) phenyl] chloroborane (TMP = 2,2,6,6-tetramethylpiperidine) FLP.

Using theoretical methods Wang and co-workers[15] have tried to design novel metal free hydrogen storage compounds (Figure 1.5) employing C/P and B/N FLPs. BP86-GD3BJ/6-311++G(3d,2p) method was used to optimize the structures while MP2/cc-pVTZ method was used to calculate the single point energies. Computations revealed that B/N pairs are not as frustrated as corresponding C/P compounds and hydrogenation is directly proportional to the difference between the two relevant atomic charges. Studies also reveal that hydrogenation is easier between the atoms which undergo small change of the atomic charges after the additive reaction.

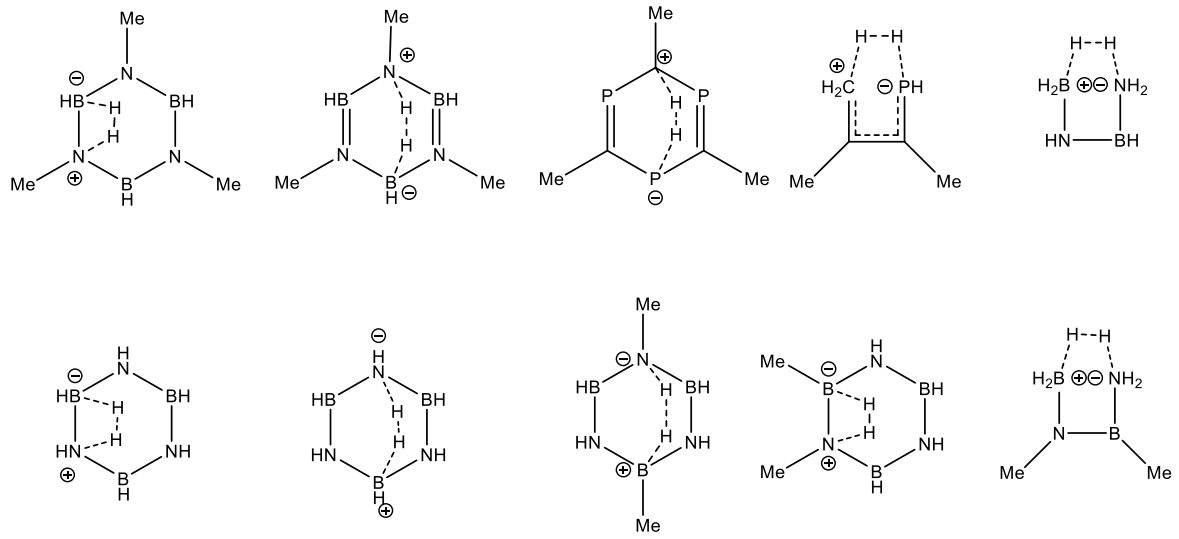

Figure 1.5 Metal free hydrogen compounds.

Yepes and co-workers[16] have computationally investigated heterolytic splitting of H_2 using a new class of α, α-disubstituted geminal aminoborane-based FLPs (Figure 1.6). Meta-hybrid M06-2X exchange-correlation functional combined with the def2-TZVPP basis set have been employed to explore the reaction mechanism. Activation strain model of reactivity combined with the energy decomposition analysis method has been utilized to quantitatively study the physical factors controlling the activation pathway. Studies revealed that this is a concerted reaction in which good electron withdrawing groups or soft/poor π donors at boron significantly reduce the activation barrier.

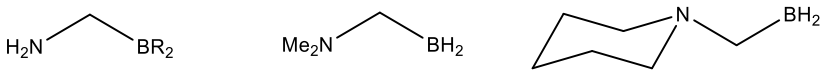

Figure 1.6 α, α-Disubstituted geminal aminoborane-based FLPs

Zhivonitko and co-workers[17] have reported novel FLPs derived from ansa-aminoboranes (AAB) which are known as ‘‘molecular tweezers’’ (Figure 1.7) because they stretch, but do not completely split, H_2 molecules. ωB97X-D/6-311G** level of theory was used for geometry optimizations and for calculating coupling constants

between the NH and BH protons of BorylCAT (the AAB with smallest boryl site -BH_2)–H_2. Studies reveal that all these new metal free catalysts have ability to provide parahydrogen-induced polarization (PHIP) which in turn is able to substantial increase in NMR signals and eventually may be used for *in vivo* MRI applications.

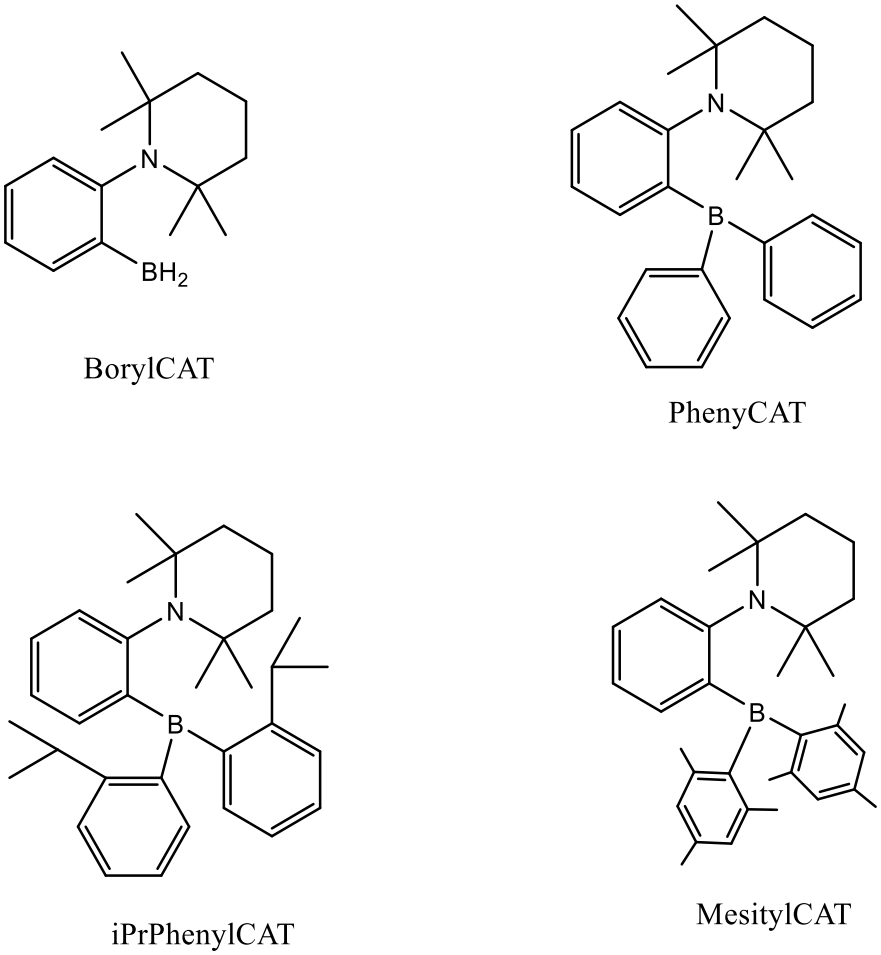

Figure 1.7 Molecular Tweezers used in reference 17.

Perez and co-workers[18] have used DFT to study of the mechanism of hydrogen activation using some novel FLPs (Figure 1.8). ωB97X-D/6-311G(d,p) level of theory was used for these studies, and to analyse reactivity indices namely electronic chemical potential, hardness, electrophilicity and nucleophilicity followed by activation energies and finally catalytic activity of the hydrogenated FLPs. Results of the studies

reveal that the activation of hydrogen via these FLP catalysts occurs with low activation energies via a polarized TS in one step.

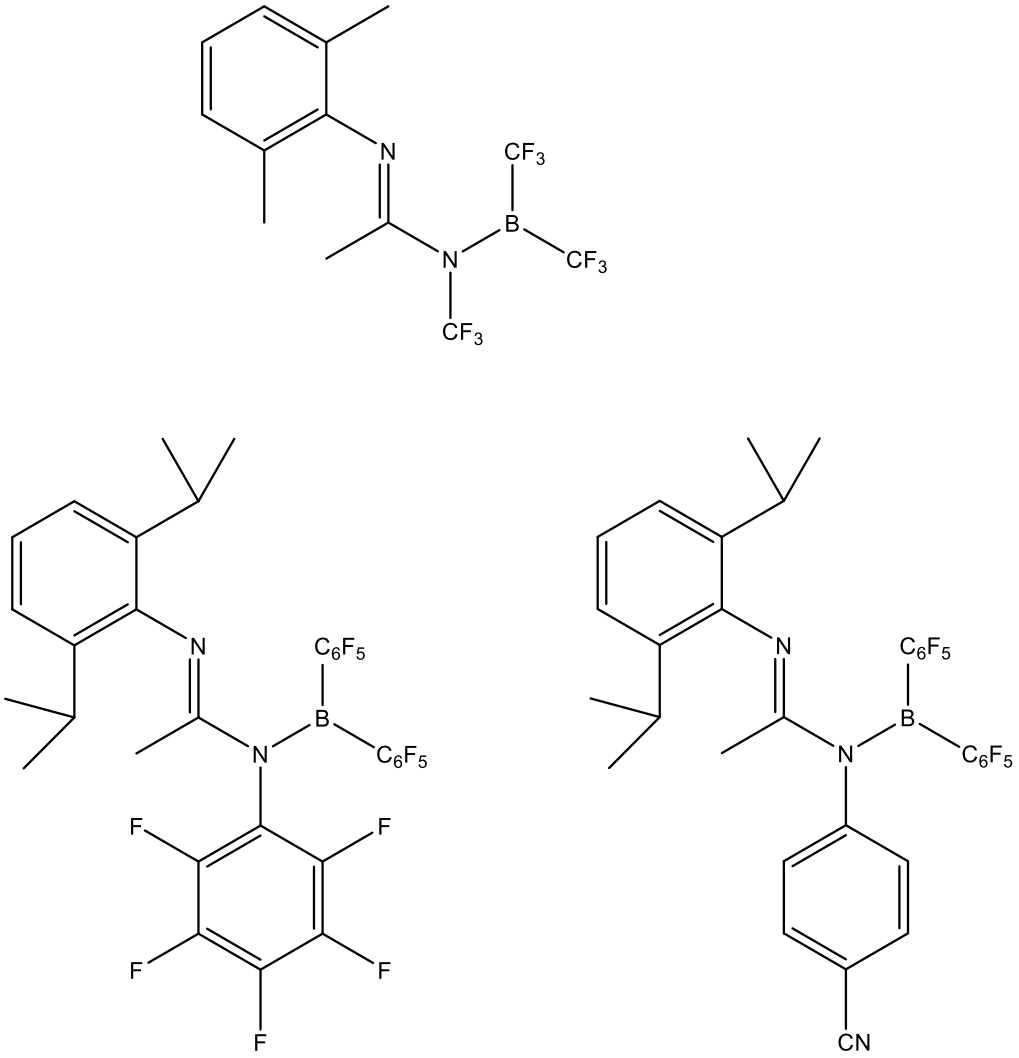

Figure 1.8 FLPs used in reference 18

Clark and co-workers[19] have reported N-methylacridinium salts (Lewis acids) (Figure 1.9) which forms FLPs with weak base like 2,6-lutidine which is able to activate H_2, even in the presence of H_2O. Hydrogen ion affinities of these compounds have been computed at M06-2X/6-311G(d,p) level, using polarizable continuum model (PCM) model of dichloromethane (DCM) solvent. Computationally as well as experimentally these salts have proven to have an appropriate HIA to be useful as carbocationic Lewis

acids in FLPs for H_2 activation and hydride transfer. Some of these salts are also able to catalyse hydrosilylation of unhindered imines due to their low acidity towards hard Lewis bases. Some of these salts can be used as cheap, air- and moisture-stable catalysts for dehydrosilylation of alcohols.

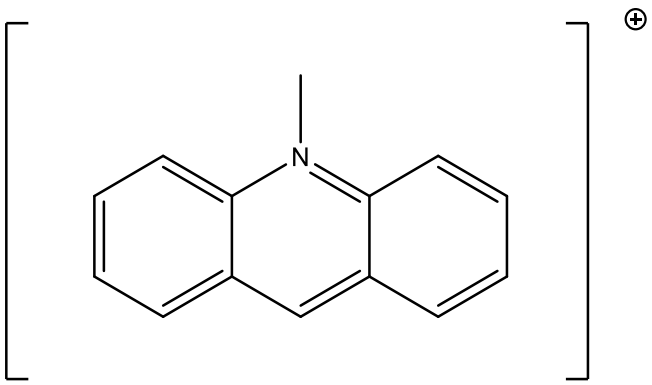

Figure 1.9 N-Methylacridinium salts (Lewis acids) that form FLPs with weak base like 2,6-lutidine.

Rokob and co-workers[20] have attempted to interpret the facile heterolytic cleavage of H_2 by FLPs with the help of two alternative reactivity models. Both of the proposed models have one similarity that they assume that the reaction takes place via reactive intermediates with preorganized acid/base partners, but the difference lies in the mode of action. Electron transfer (ET) model envisages hydrogen activation by synergistic electron donation processes involving simultaneous active centres and the bridging hydrogen. Electric field (EF) model on the other hand suggests the heterolytic bond cleavage by polarization due to strong EF present in the cavity of the reactive intermediates. The study was done using density functional theory (DFT) with the dispersion-corrected, range-separated hybrid ωB97X-D exchange-correlation functional. For geometry optimization, vibrational frequency determination, electronic structure analysis, and calculation of EFs, 6-311G(d,p) basis set was used, and for

single-point energies 6-311++G(3df,3pd) basis set was employed. The results of the studies indicate that the electric-field-based reactivity model supersedes the previously published framework suggesting synergistic donor→σ*(H_2) and σ(H_2)→ acceptor electron donations as key elements.

Hounjet and co-workers[21] (Scheme 1.8) have reported activation of H_2 by dialkyl ether/$B(C_6F_5)_3$ catalysts which have been utilized for hydrogenations of 1,1-diphenylethylene. To understand the mechanism, optimizations were carried out at TPSS-D3/def2-TZVP levels while single point calculations used B2PLYP-D3/def2-QZVP levels. Thermal corrections for free energy and zero point vibrational energy (ZPVE) were added and solvation free energy corrections were done using conductor like screening model for real solvents (COSMO-RS) model. It has been found that the barrier for the complex formed as result of H_2 activation is quite accessible which on dissociation leads to ions $[Et_2O\cdots H\cdots OEt_2]^+$ and $[HB(C_6F_5)_3]^-$ which in turn leads to hydrogenation.

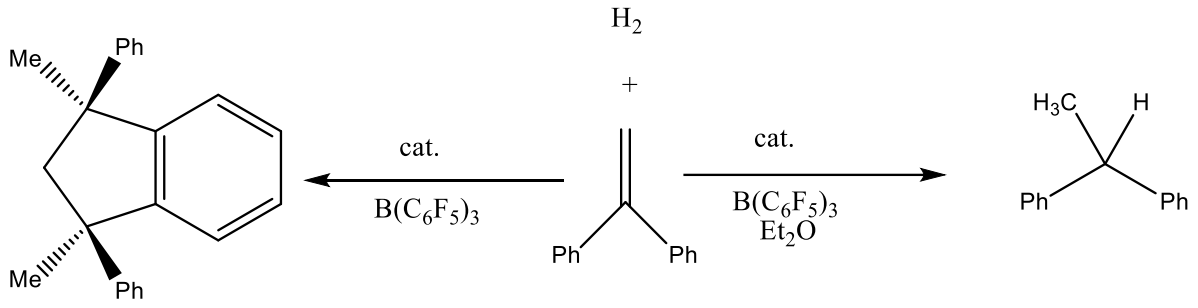

Scheme 1.8 Reaction of 1,1-diphenylethylene in presence of $B(C_6F_5)_3$ with (right) and without (left) diethyl ether.

Greb and co-workers[22] have studied metal free hydrogenation of various olefins utilizing FLPs which are able to activate H_2 at the lowest possible temperatures (Scheme 1.9) and have utilized this reaction for metal free hydrogenation of various olefins. They employed B2PLYP-D3(BJ)/def2-TZVP//TPSS-D3(BJ)/def2-TZVP level of theory for calculation of energies. It was observed that in the case of phosphines the Lewis pair adduct and the zwitterionic hydrogen activation product is endergonic but reduction of the olefinic double bond is shown to be highly exergonic which is necessary for an efficient catalytic cycle.

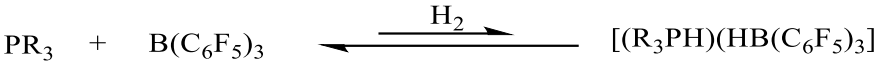

Scheme 1.9 Reversible activation of hydrogen in temperature range between -60^{0}C and -80^{0}C.

Guo and co-workers[23] carried out DFT calculations to study the possibility of using FLPs as bifunctional metal-free dehydrogenation catalysts (Scheme 1.10) of ammonia-borane NH_3BH_3 (AB). N/B pair was chosen to explore the possibility that FLPs release H_2 from AB. According to these authors, the mechanism involves two steps: in the first, AB is dehydrogenated by the N/B pair to form the NH/BH compound and NH_2BH_2 at low temperature, and then in the next step H_2 is released from the NH/BH compound at 110 °C and the N/B pair regenerates. All calculations were performed with the B3LYP method using 6-31G(d,p) basis set. Calculations show that the dehydrogenation of AB by the N/B pair has the lowest free-energy barrier as compared to the uncatalyzed reaction which leads to a possibility that FLPs can act as bifunctional catalysts to release H_2 from AB under appropriate conditions.

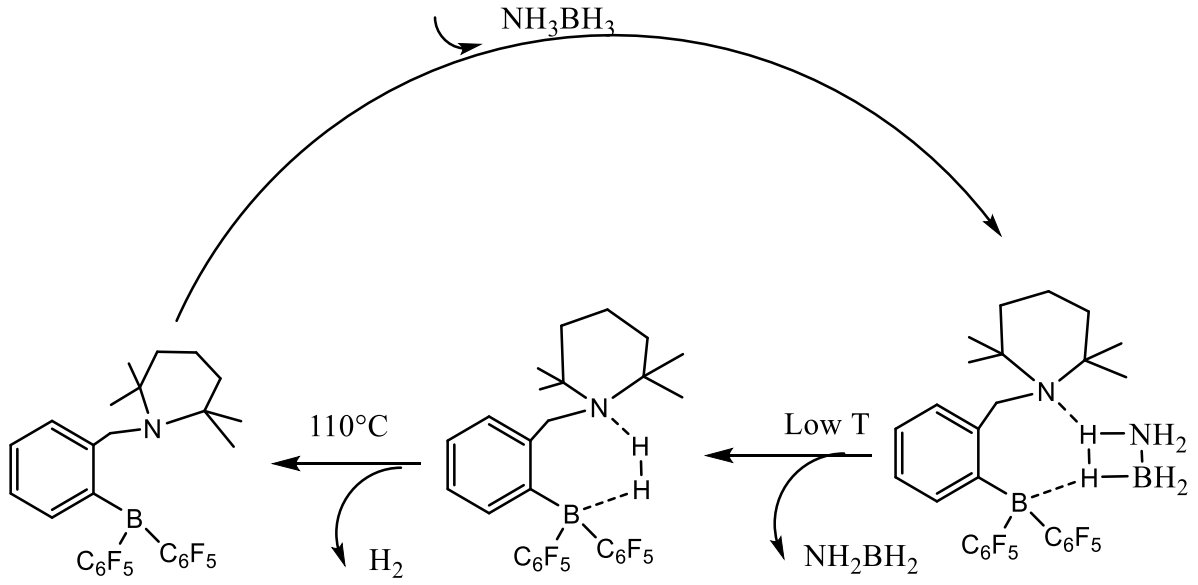

Scheme 1.10 Catalysis by metal free bifunctional dehydrogenation catalysts.

Rokob and co-workers[24] (Figure 1.10) have calculated the acid-base strength of non-linked and linked FLPs in order to analyse their ability to undergo heterolytic hydrogen splitting reactions with the help of quantum chemical calculations. The geometries of all species have been optimized using density functional theory at the M05-2X/6-31G(d) level. In the non-linked FLPs the calculated reaction free energies correlated well with the cumulative acid−base strengths as the products are very similar to them in structure but in the case of intramolecular FLPs system lose less entropy when reacting with H_2 than do unbound, non-linked systems. As a consequence, smaller acid−base strength and stabilization may be sufficient to produce reactive compounds.

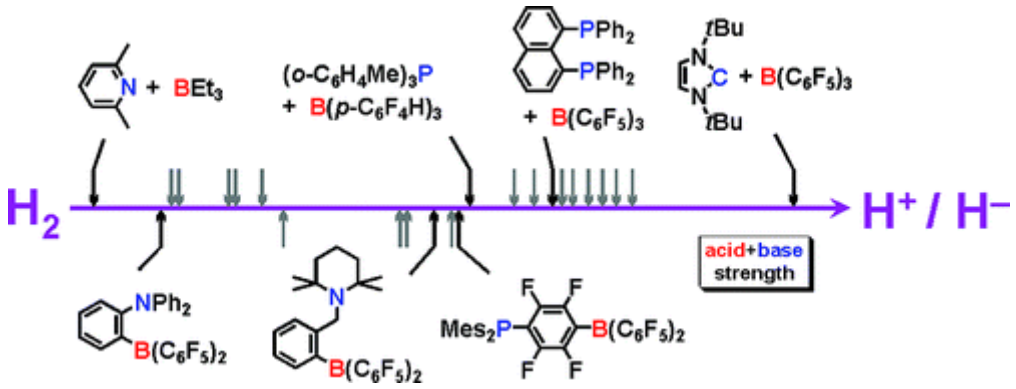

Figure 1.10 Scale of heterolytic hydrogen splitting from ref 24

Chase and co-workers[25] investigated the capability of N-heterocyclic carbene (1,3-di-tert-butyl-1,3-imidazol-2-ylidene) to activate H_2 [using $B(C_6F_5)_3$] and N-H bond using various amino boranes. [(1,3-di-tert-butyl-1,3-imidazol-2-ylidene) H] [$HB(C_6F_5)_3$] salt was formed because of H_2 activation and various amido boranes by N-H bond activation. Molecules were optimized using 3-21G basis set or 6-31+G(d) basis set in which peripheral H atoms are treated by 3-21G basis set. Re-optimization of the structures was done by using two-layer ONIOM technique using the MPW1K DFT model. Single point energies were calculated using M06/6-311++G(d,p) level of theory. It has been observed that N-H bond activation depends on the type of amine substituents and if they are electron-donating then amino boranes are formed by the loss of C_6F_5H.

Ghara and co-workers[26] have reported hydrogenation of CO_2 by a bridged B/N FLP (Figure 1.11). They have elucidated the two possible pathways for the reaction at M06-2X-D3/6-31G(d) level of theory. Energy decomposition analysis (EDA) along with the natural orbital for chemical valence (NOCV) method at BP86-D3/TZ2P//M06-2X-D3/6-31g(d) level of theory reveal that the HOMO of the FLP donates electron density to the

LUMO of H_2, the HOMO of which in turn donates electron density to the LUMO of CO_2, and several occupied MOs of CO_2 donate electron density to the LUMO of FLP at the TS.

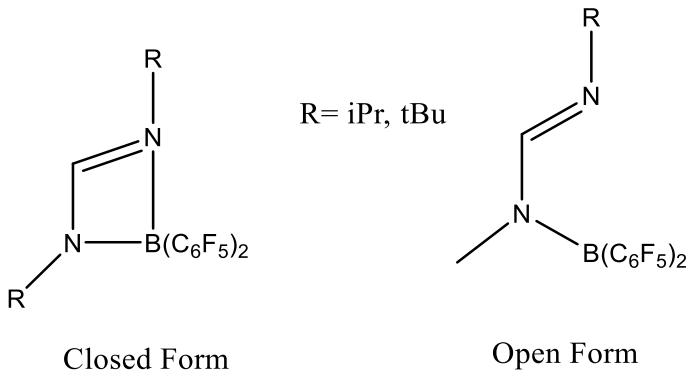

Figure 1.11 Bridged B/N FLP used for hydrogenation of CO_2.

1.2 Silylation and Borylation by FLPs

Fasano and co-workers[27] have reported a new family of Lewis acids i.e. N-Me-benzothiazolium salts (Scheme 1.11) which can undergo FLP type catalysis and are reported to activate Si-H σ bonds. M06-2X/6-311G(d,p) method and H/D scrambling experiments have been used to screen various Lewis acids by changing C2 aryl substituents in these cations. Studies revealed that Lewis acidity of these cations towards hydride is comparable to triarylboranes but is less towards hard Lewis bases. They have been found to be effective for Si-H bond activation and as catalysts for the (de)hydrosilylation of imines.

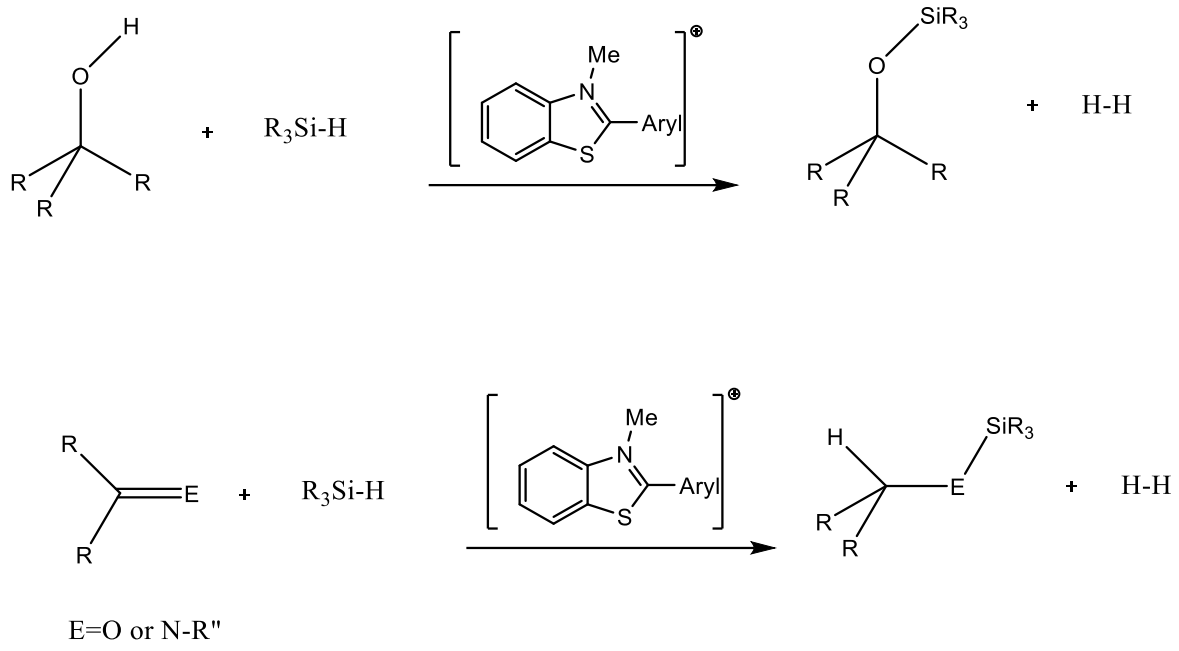

Scheme 1.11 Benzothiazolium cation catalysed hydrosilylation and dehydrosilylation using stoichiometric silane.

Cabrera-Trujillo and co-workers[28] have reported geminal FLPs having borole fragment that are able to activate many small molecules like H_2, CO_2, CS_2, HCRCH, SiH_4 and CH_4 and form corresponding adducts as result (Scheme 1.12). They have utilized GIAO-B3LYP/def2-SVP//M06-2X/def2-SVP level of theory to understand the whole mechanism of activation. DFT indicates that gain in aromaticity along the reaction co-ordinate is the key factor that enhance the activity of these FLPs.

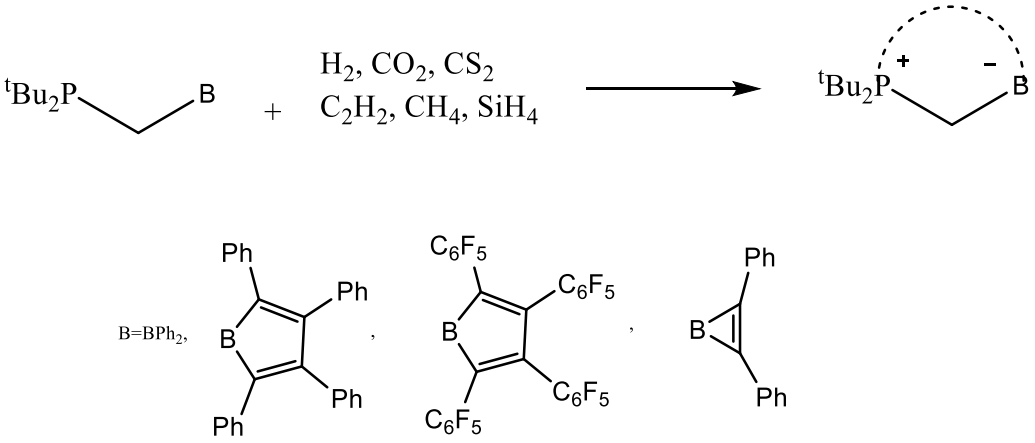

Scheme 1.12 Geminal FLPs having borole fragment that activate many small molecules like H_2, CO_2, CS_2, HCRCH, SiH_4 and CH_4

Rochette and co-workers[29] have reported metal free borylation of thiols with the help of ambiphilic FLP $(NMe_2\text{-}C_6H_4\text{-}BH_2)_2$ which can be applied for one pot Michael additions from these reactants (Scheme 1.13). ωB97XD functional along with 6-31++G** basis set have been utilized to investigate the mechanism of the reaction. Studies reveal that release of H_2 is the driving force in this reaction.

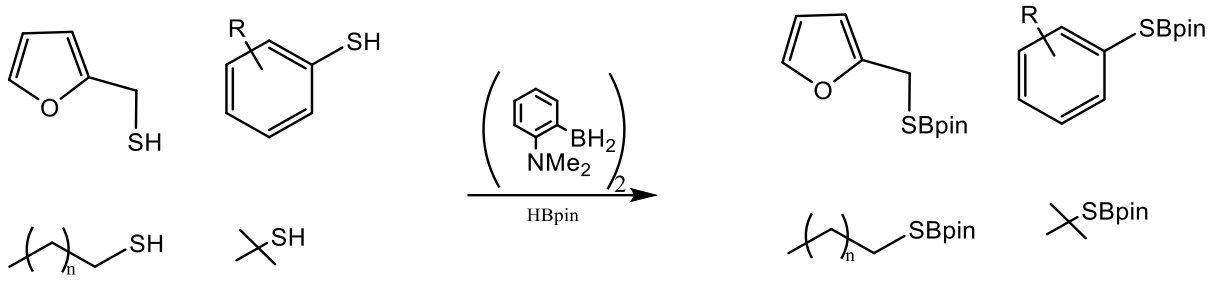

Scheme 1.13 Borylation of thiols with the help of ambiphilic FLP.

Lavergne and co-workers[30] have reported two new ambiphilic aminoboranes, $(1\text{-}Pip\text{-}2\text{-}BH_2\text{-}C_6H_4)_2$ (Pip = piperidyl) and $(1\text{-}NEt_2\text{-}2\text{-}BH_2\text{-}C_6H_4)_2$ (NEt_2 = diethylamino), FLPs (Figure 1.12) that were used for borylation of heteroarenes. These new FLPs had less steric hindrance as compared to their previously synthesized analogues. ωB97XD/6-31+G** (SMD, chloroform) method was utilized to study the energies of the species involved. The results of the computational studies reveal that these new catalysts were much more effective than their older bulkier versions. Calculations also indicate that the rate determining step maybe the dissociation of dimer and removal of hydrogen.

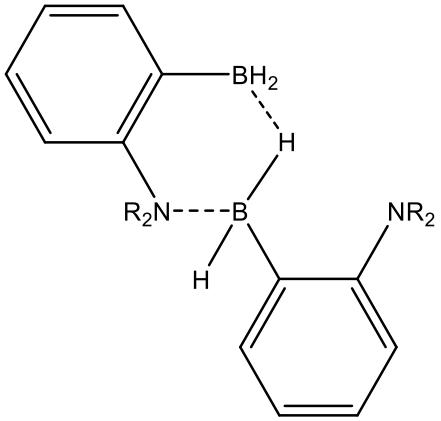

NR_2=piperidyl, NEt_2

Figure 1.12 Ambiphilic aminoboranes, (1-Pip-2-BH_2-C_6H_4)$_2$ (Pip = piperidyl) and (1-NEt_2-2-BH_2-C_6H_4)$_2$ (NEt2 = diethylamino), FLPs.

Tang and co-workers[31] have reported 1,1-hydroboration of Ph_2CN_2 with $HB(C_6F_5)_2$ and have also isolated diazomethane–borane adduct involved (Scheme 1.14). Dispersion-corrected PBEh-3c (DSD-BLYP/def2-TZVPP//PBEh-3c+COSMO-RS) DFT method was utilized to study the reaction system. This method was employed to study not only the diazomethane-borane adduct but also an exergonic carbene adduct of $B(C_6F_5)_3$ formed by the loss of N_2 from the former. Calculations reveal that the 1,1-hydroboration proceeds via concerted mechanism which involves H-atom migration from boron to the proximal nitrogen. Isolation of adduct may be helpful in metal free N_2 capture.

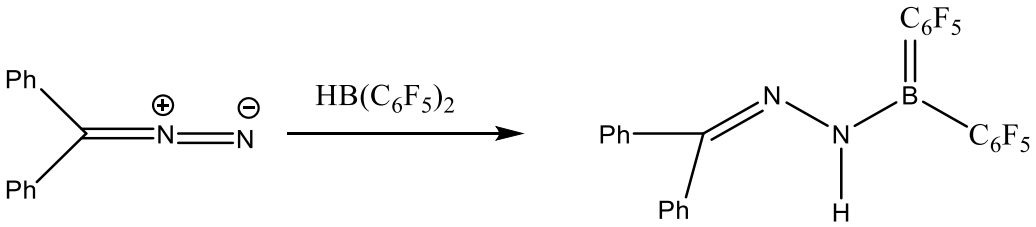

Scheme 1.14 1,1-hydroboration of Ph_2CN_2 with $HB(C_6F_5)_2$

Ye and co-workers[32] have utilized $Mes_2PCH_2CH_2B(C_6F_5)_2$ P/B FLPs and $HB(C_6F_5)_2$ to reduce carbon monoxide to give FLP stabilized borane product which readily inserts sulfur dioxide into the B–O bond (Scheme 1.15). DFT analysis at the PW6B95-D3(BJ)/def2-QZVP + COSMO-S(CH_2Cl_2)// PBEh-3c level of theory have been utilized to study the mechanism of insertion and the results indicate that insertion is initiated by opening of B^2-O linkage rather than B^1-O linkage as former requires lower energy.

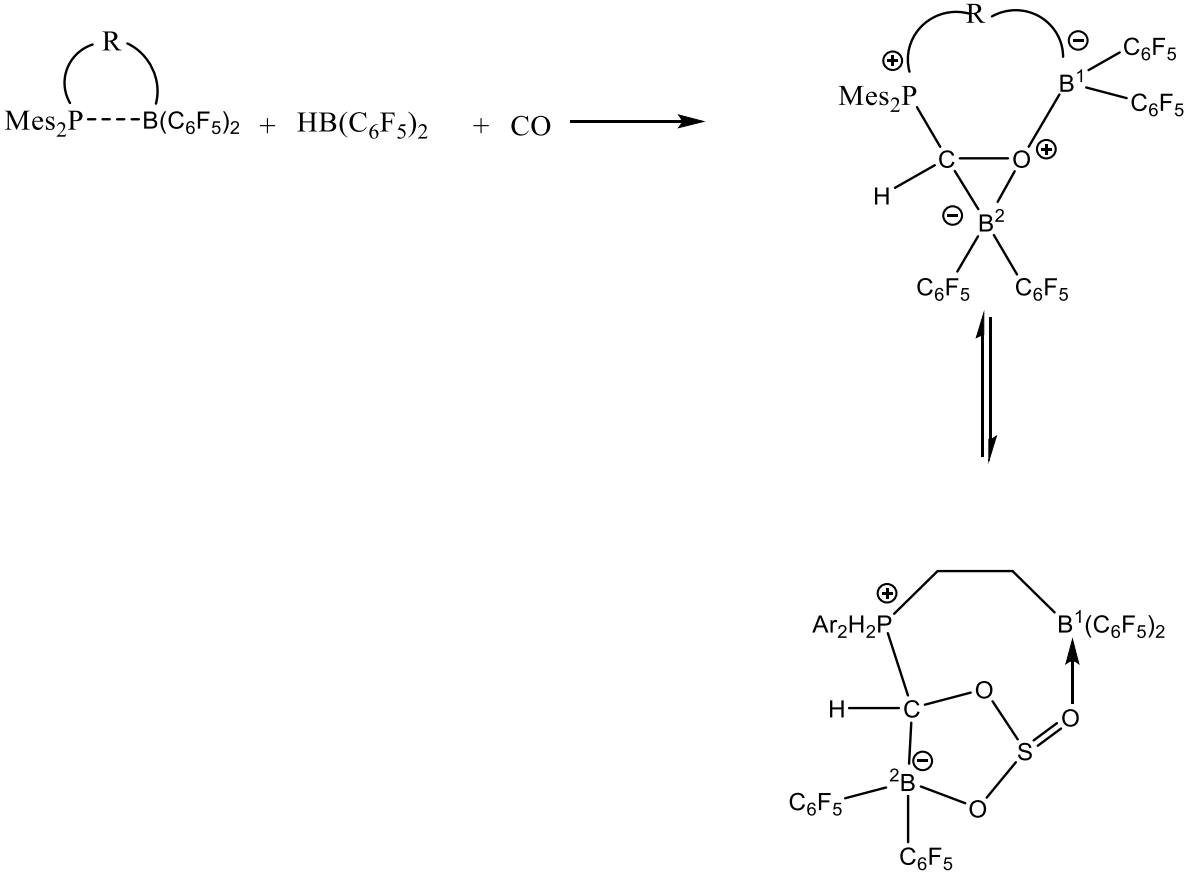

Scheme 1.15 Reduction of carbon monoxide to give FLP stabilized borane product which readily inserts sulfur dioxide into the B–O bond.

McQuilken and co-workers[33] (Figure 1.13) have synthesized new FLP isomers by hydroboration of bulky isocyanates with Piers borane ($HB(C_6F_5)_2$). The hydroboration of smaller isocyanates leads to anticipated N/B FLP adducts while the hydroboration of bulky isocyanates leads to the formation of a new class of isomers (confused FLPs).

which are substrate free aminoboranes having short covalent N-B bond without any direct O-B interaction. This confused FLP isomer was studied using PW6B95-D3/def2-QZVP (COSMO-RS, fluorobenzene)//PBEh-3c level of theory. The studies revealed that the confused FLP isomer has lower free energy as compared to its normal counterpart although this intramolecular arrangement places sterically demanding ^{Ph2tBu}ArN moiety adjacent to the $B(C_6F_5)_2$ group. These compounds isomerize to the normal FLP isomer which then shows typical N/B FLP-type reactivity with isocyanates and isocyanides but the confused isomer itself does not lead to facile reactions with substrates like H_2 or CO_2. The plausible reason for this observation can be the kinetic and thermodynamic barriers between these isomers which may be required for substrate capture.

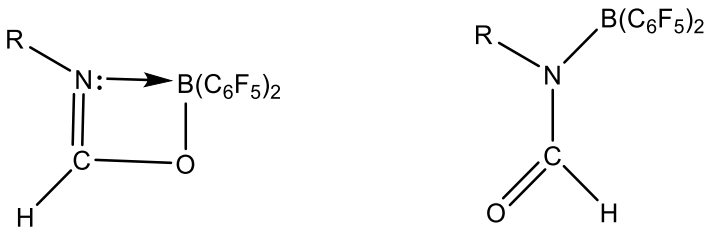

$R=^{iPr2}Ar=2,6\text{-}iPr_2C_6H_3$

$^{Ph2tBu}Ar=2,6\text{-}Ph_2\text{-}4\text{-}tBuC_6H_2$

Anticipated FLP Confused FLP

Figure 1.13 Anticipated and confused isomer (FLP).

1.3 Polymerization by FLPs

Ottou and co-workers[34] have shown that organic Lewis pairs involving tris(2,4,6-trimethoxyphenyl) phosphine (TTMPP) as a Lewis base, and N-(trimethylsilyl)bis (trifluoromethane sulfonyl) imide (Me_3SiNTf_2) as a Lewis acid can directly initiate the polymerization of methyl methacrylate (MMA) at room temperature in toluene (Scheme 1.16). M06-2X (SMD-toluene)/6-311++G**//M06-2X/6-31G** level of theory enabled

them to choose the silane (Me_3SiNTf_2 rather than Me_3SiOTf) capable of activating MMA, locating two FLP structures and a transition state connecting them. Theoretical calculations indicated the reaction to proceed via FLP mediated preorganized complex in which phosphine interacted with activated MMA by multiple hydrogen bonds.

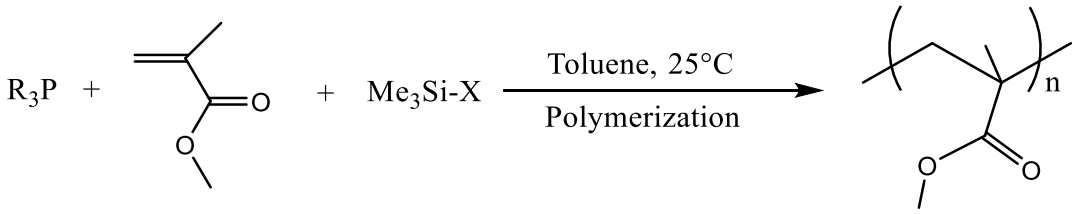

R= n-butyl, *tert*-butyl, 2,4,6-trimethoxyphenyl

X=trifluoromethanesulfonate (OTf), bis-(trifluoromethane)sulfonimide (NT_2)

Scheme 1.16 Polymerization of methyl methacrylate (MMA) at room temperature in toluene using phosphine in conjunction with a silane.

1.4 Formation of heterocycles by FLPs

Boom *et. al.*[35] have reported (Scheme 1.17) four, five and six membered heterocycles by the reaction of phenyl-, mesityl-, tert-butyl and trimethylsilyl azide with geminal FLP ($tBu_2PCH_2BPh_2$). Calculations to study the mechanism have been done on wB97X-D/6-31G* level of theory. Results of the calculations reveal that all products proceed via a six-membered ring structure that is thermally stable with an N-phenyl group but rearranges when bulky substrates are used instead.

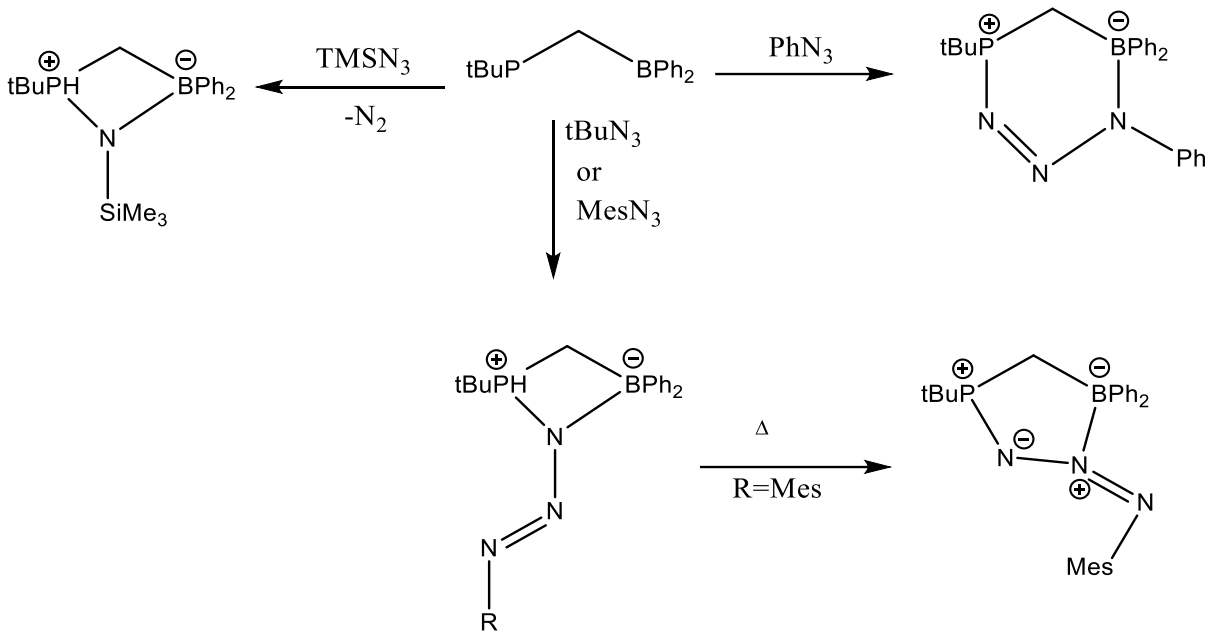

Scheme 1.17 Heterocycles by the reaction of phenyl-, mesityl-, tert-butyl and trimethylsilyl azide with geminal FLP ($tBu_2PCH_2BPh_2$).

Zhu and co-workers[36] (Figure 1.14) have reported the formation of several heterocycles by addition reactions of P-O-B based intramolecular FLPs ($R_2POBcat$) with small molecules like PhOH, CO_2, CS_2, PhNCO, MesCNO, O_2, 9,10-phenanthrenedione, and diazomethanes. These reactions were computationally monitored using TPSS-D3/def2-TZVP + COSMO(DCM) level of theory. It has been found that these FLPs react readily despite perceived poor reactivity of the boron centre. This study also provided facile route for diazomethane capture.

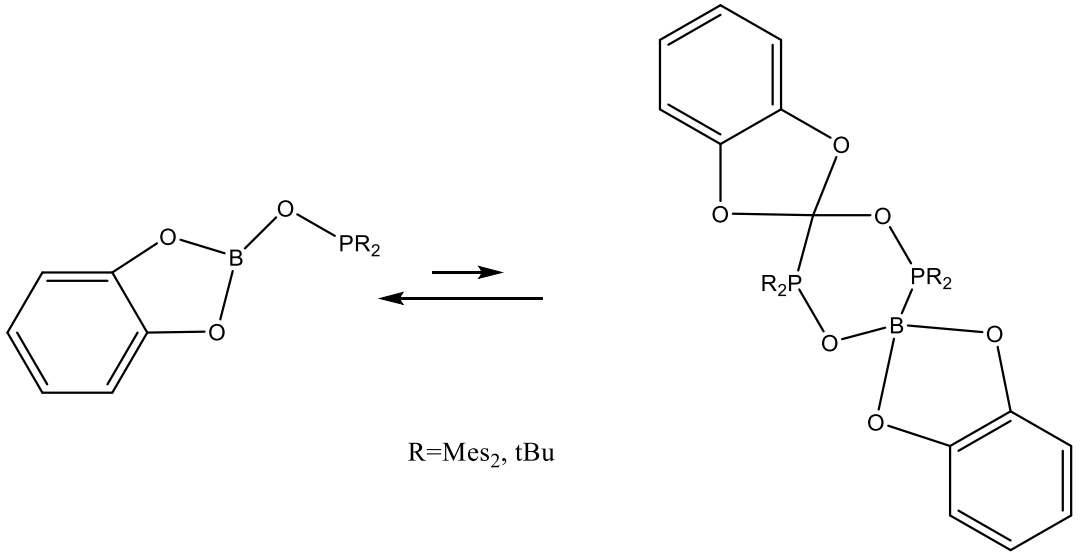

Figure 1.14 P-O-B based intramolecular FLPs

Rochette and co-workers[37] have reported cleavage of a Csp^3-H bond in the C-H bond of methyl in α position of a nitrogen atom by ambiphilic FLP $(2\text{-}NMe_2\text{-}C_6H_4)_2BH$ to form new N-B heterocycle (Scheme 1.18). Computational studies were done using ωB97XD/6-31++G**, SMD (benzene) level of theory to understand the ability of FLP to activate intramolecular Csp^3-H bond. Studies indicate that simultaneous release of H_2 along with product formation makes the thermodynamics favourable although the products are a little higher in energy.

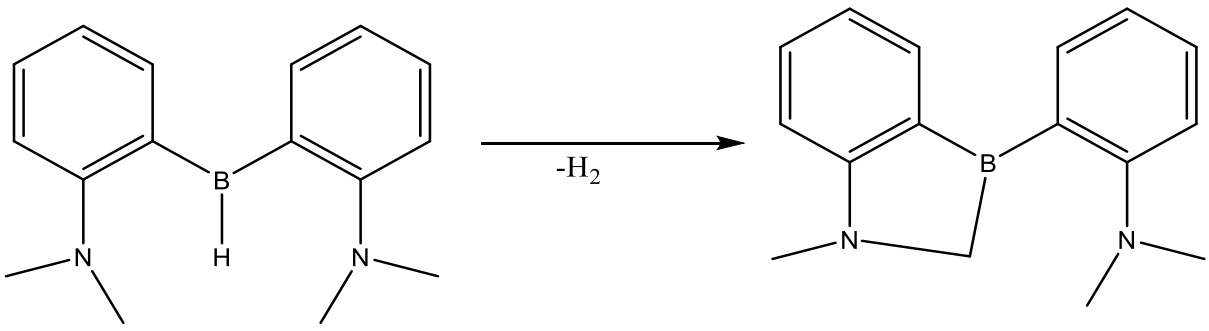

Scheme 1.18 Cleavage of a Csp^3-H bond in α position of a nitrogen atom by ambiphilic FLP $(2\text{-}NMe_2\text{-}C_6H_4)_2BH$ to form new N-B heterocycle.

1.5 Reaction of FLPs with small gaseous molecules

Sajid and co-workers[38] (Scheme 1.19) have reported addition of SO_2 to intermolecular FLP $tBu_3P/B(C_6F_5)_3$, which lead to the formation of zwitterionic adduct ($tBu3P^+–S(O)–OB^-(C_6F_5)_3$) and six membered addition products in the case of intramolecular vicinal P/B FLPs. The reaction was investigated computationally by (B2PLYP-D3/def2-TZVP//TPSS-D3/def2-QZVPP + COSMO-RS solvent). The investigations revealed that [B]–O–(O)S–[P] conformational isomers (equatorial and axial) were a slightly more stable than the hypothetical [B]–S(O)–O–[P] regioisomers (equatorial and axial). Furthermore, kinetic barrier for FLP-SO_2 adduct formation was remarkably low.

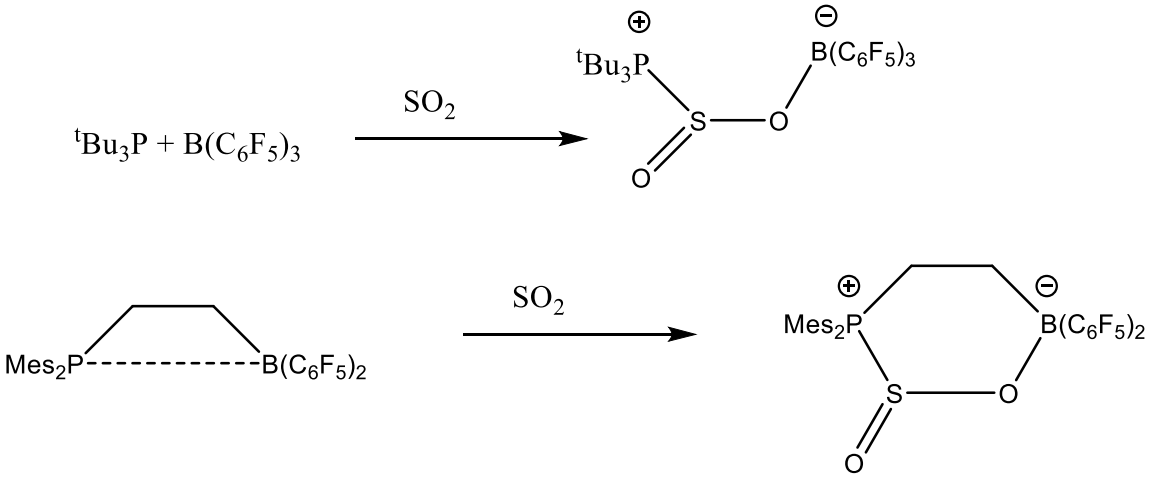

Scheme 1.19 Zwitterionic adducts formed by inter- and intramolecular FLPs.

Adenot and co-workers[39] (Scheme 1.20) have reported FLPs having skeleton of guanidine 1,5,7-triazabicyclo[4.4.0]dec-5-ene (TBD) and the substituted derivatives $[TBD–SiR_2]^+$ and $TBD–BR_2$. They have compared the ability of these FLPs to activate SO_2 with CO_2 activation. They have employed M06/6-311+G* level of theory with PCM solvent to study the activation by these FLPs. Experimental as well as theoretical

studies have revealed that although the adducts formed with SO_2 are similar to those with CO_2 but are thermodynamically more stable.

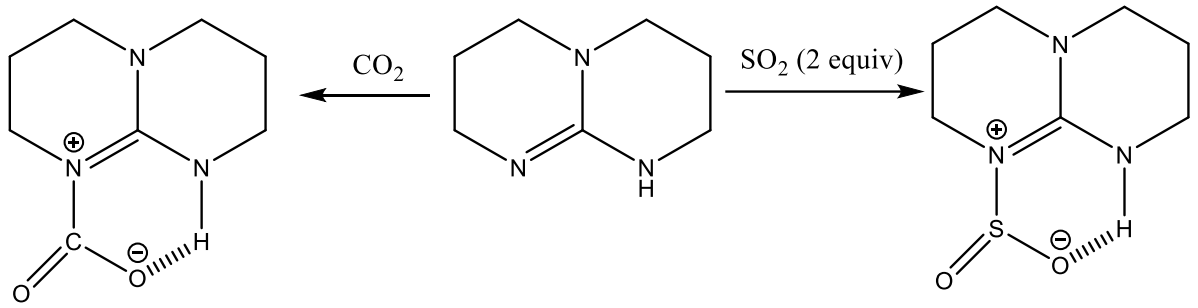

Scheme 1.20 Activation of CO_2 and SO_2 by 1,5,7-triazabicyclo[4.4.0]dec-5-ene (TBD).

Wang and co-workers[40] have reported some new macrocyclic dimers and trimers formed by carbonylated trifunctional P/B/B FLPs having some bulky aryl groups like Dmesp (2,6-dimesitylphenyl), Tipp (2,4,6-triisopropylphenyl) and Mes* (2,4,6-tritertbutylphenyl) at Phosphorous (Figure 1.15). Structures involved in the study were optimized using PBEh-3c method while PW6B95-D3 level of theory along with def2-TZVP basis set was employed for single point calculations. Solvation free energies were computed with COSMO-RS method. DFT studies indicate that the CO insertion key step in these reactions is exergonic, and that this eventually leads to macrocyclic ring closure.

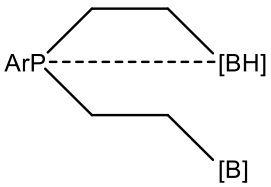

[B]: $B(C_6F_5)_2$

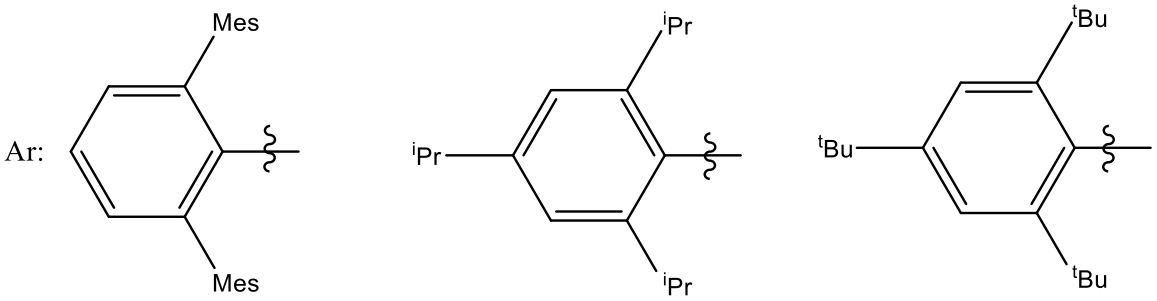

Mes: 2,4,6-trimethylphenyl

Dmesp (2,6-dimesitylphenyl), Tipp (2,4,6-triisopropylphenyl) and Mes* (2,4,6-tritertbutylphenyl)

Figure 1.15 Trifunctional P/B/B FLPs having some bulky aryl groups like Dmesp (2,6-dimesitylphenyl), Tipp (2,4,6-triisopropylphenyl) and Mes* (2,4,6-tritertbutylphenyl) at phosphorus.

Peuser and co-workers[41] (Figure 1.16) have synthesized the formate complexes formed by reaction between CO_2 and P/B FLPs. They utilized meta-GGA density functional TPSS and def2-TZVP basis set along with dispersion correction (DFT-D2) to study the activation of CO_2 by these FLPs. This revealed that the FLPs can successfully capture CO_2 and formate fragments, but also that the adducts cannot be derivatized because of their thermal instability.

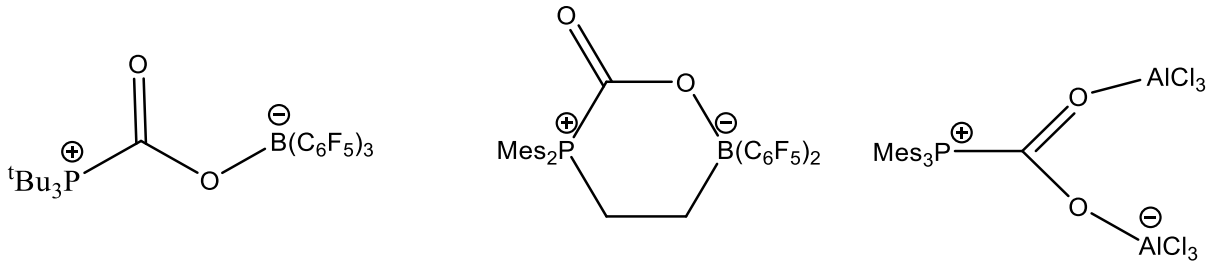

Figure 1.16 Complexes of FLP with CO_2.

Momming and co-workers[42] have studied reversible and metal free binding of CO_2 with inter- and intra-molecular B/P FLP to form carbonic acid derivatives (Scheme 1.21). Both the reactions were studied using B97-D/TZVPP', B2PLYP-D/TZVPP', and B2PLYP-D/QZVP (-g, -f) levels of theory. Their studies indicate that formation of P-C and B-O bond is concerted and synchronous. The reaction is found to be overall exothermic.

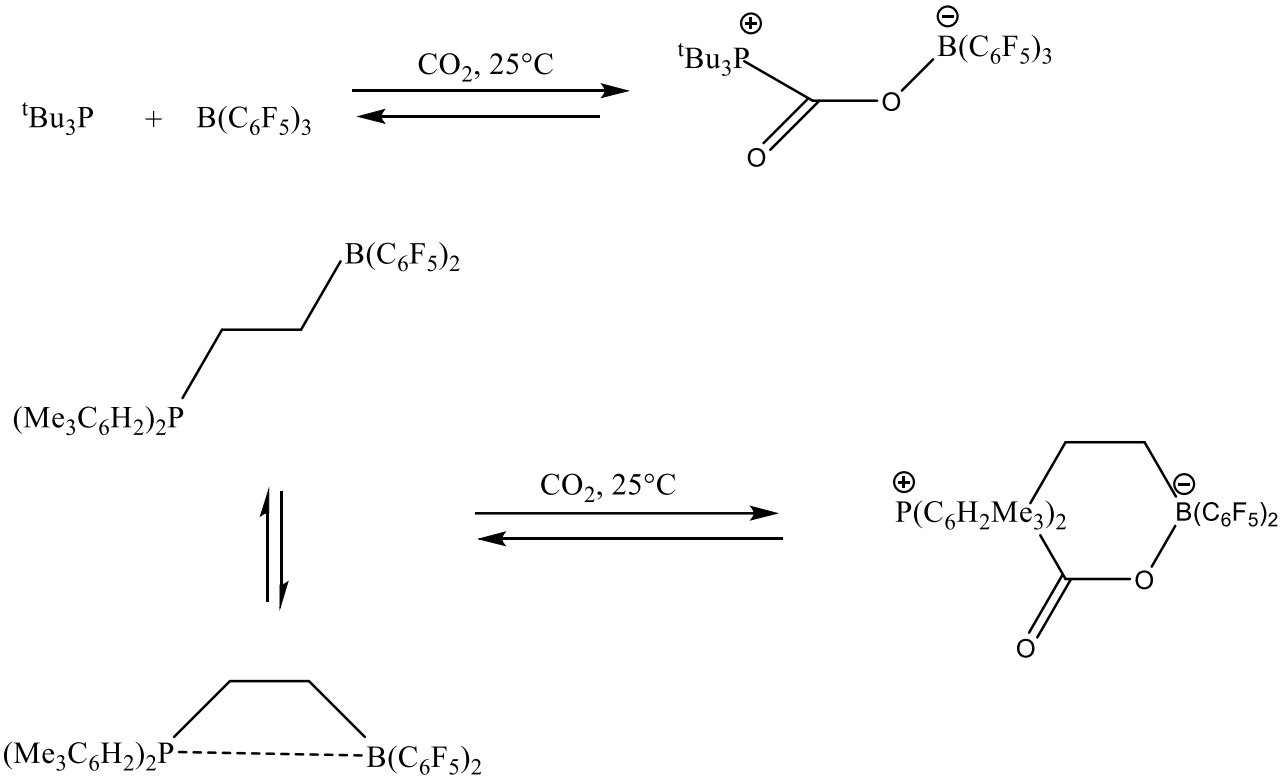

Scheme 1.21 Reversible uptake of CO_2 by FLPs.

Pereira and co-workers[43] have done kinetic and computational study of the reaction of NO with the intramolecular bridged P/B FLP *endo*-2-(dimesitylphosphino)-*exo*-3-bis(pentafluorophenyl)boryl-norbornane to give a persistent FLP-NO aminoxyl radical (Scheme 1.22). The free energies in this study have been calculated on TPSS-D3/ def2-TZVP level along with thermal and solvent corrections in toluene and on higher PW6B95-D3 level of theory. Calculations show this FLP to have an unfavourable orientation for concerted reaction. The observed barrier is rationalized in terms of the reversible formation of a [B]-NO complex intermediate followed by a slower isomerization–ring closure step to the cyclic aminoxyl radical.

[P] = $PMes_2$, [B] = $B(C_6F_5)_2$

Scheme 1.22 Reaction of NO with the intramolecular bridged P/B FLP *endo*-2-(dimesitylphosphino)-*exo*-3-bis(pentafluorophenyl)boryl-norbornane to give a persistent FLP-NO aminoxyl radical.

Sajid and co-workers[44] (Scheme 1.23) have reported a novel intramolecular cyclohexylene-bridged P/B FLP [Mes_2P-C_6H_{10}-$B(C_6F_5)_2$] that reacts rapidly with NO to give the persistent FLP-NO aminoxyl radical which further undergoes a H-atom abstraction (HAA) reaction with 1,4-cyclohexadiene to give the diamagnetic FLP-NOH. According to the authors this new FLP-NO radical exhibits greater oxygen centred HAA/O-atom functionalization chemistry owing to significant polarization of the

unpaired electron density toward the O atom. Geometrical optimizations in this case were performed at the TPSS level using the basis set def2-TZVP and single-point calculations at the B2PLYP level. Both methods were enhanced with D3 dispersion correction. DFT calculations point towards the stability of the FLP-NO linkage. The results also indicate that new FLP-NO radicals exhibit greater oxygen centred HAA/O-atom functionalization chemistry as compared to other known aminoxyl radicals like TEMPO.

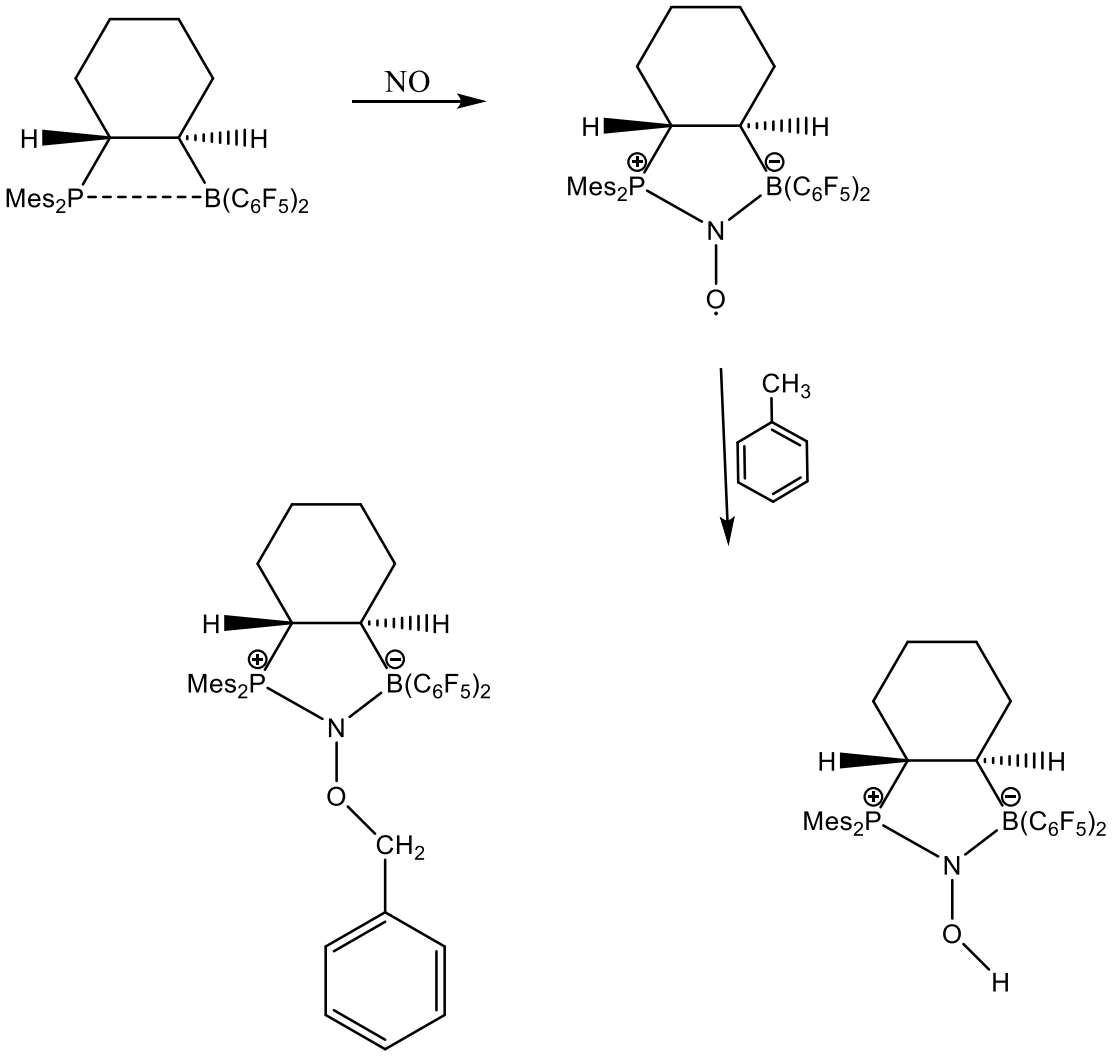

Scheme 1.23 Reaction of intramolecular cyclohexylene-bridged P/B FLP with NO.

Otten and co-workers[45] (Scheme 1.24) have reported the complexes formed by reaction of N_2O with equimolar mixture of tBu_3P and $B(C_6F_5)_3$ to form PNNOB linkages. B3LYP/6-31G(d) level of theory have been utilized to investigate the type of bonding these complexes. Studies indicate that in these complexes tBu_3P and $B(C_6F_5)_3$ fragments are arranged in a transoid geometry with respect to N=N bond.

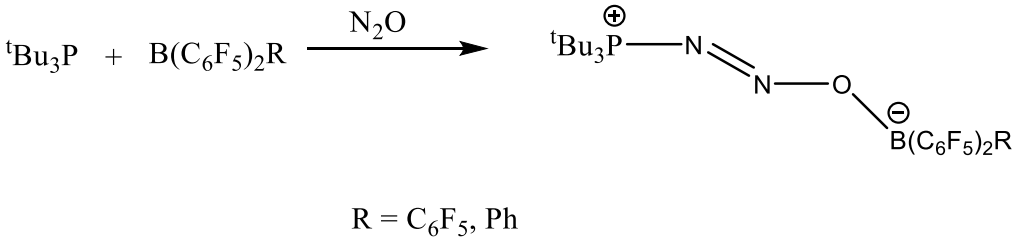

R = C_6F_5, Ph

Scheme 1.24 PNNOB formed by reaction of FLP with N_2O.

1.6 Reaction of FLPs with alkenes

Guo and co-workers[46] (Figure 1.17) have studied addition reactions of FLPs with olefins. Studies have been carried out on two different reaction systems: A three-component system involving a sterically demanding phosphane [P(*t*Bu)$_3$], borane [$B(C_6F_5)_3$], and ethylene and a two-component system involving olefin derivative of phosphane [CH2=CH–$(CH_2)_3$P(*t*Bu)$_2$] and $B(C_6F_5)_3$. The details of these mechanisms were calculated using B3LYP using 6-311++G(d,p) basis set for C=C and H atoms bound to C=C, B, and P, and those carbon atoms bonded to B or P, and 6-31G basis set for the rest of atoms. Results of the calculations reveal that in a two-component system the reaction proceeds in a concerted manner while in a three-component system reaction is initiated by the weak association of $B(C_6F_5)_3$ between ethylene leading to the formation of a transient species which is then followed by a transition state similar to the concerted mechanism of two-component system. Studies also

indicate that in a two-component reaction CH_2=CH group and in a three-component reaction C_2H_4 may act as bridge for electron transfer from the Lewis base centre P to the Lewis acid centre B.

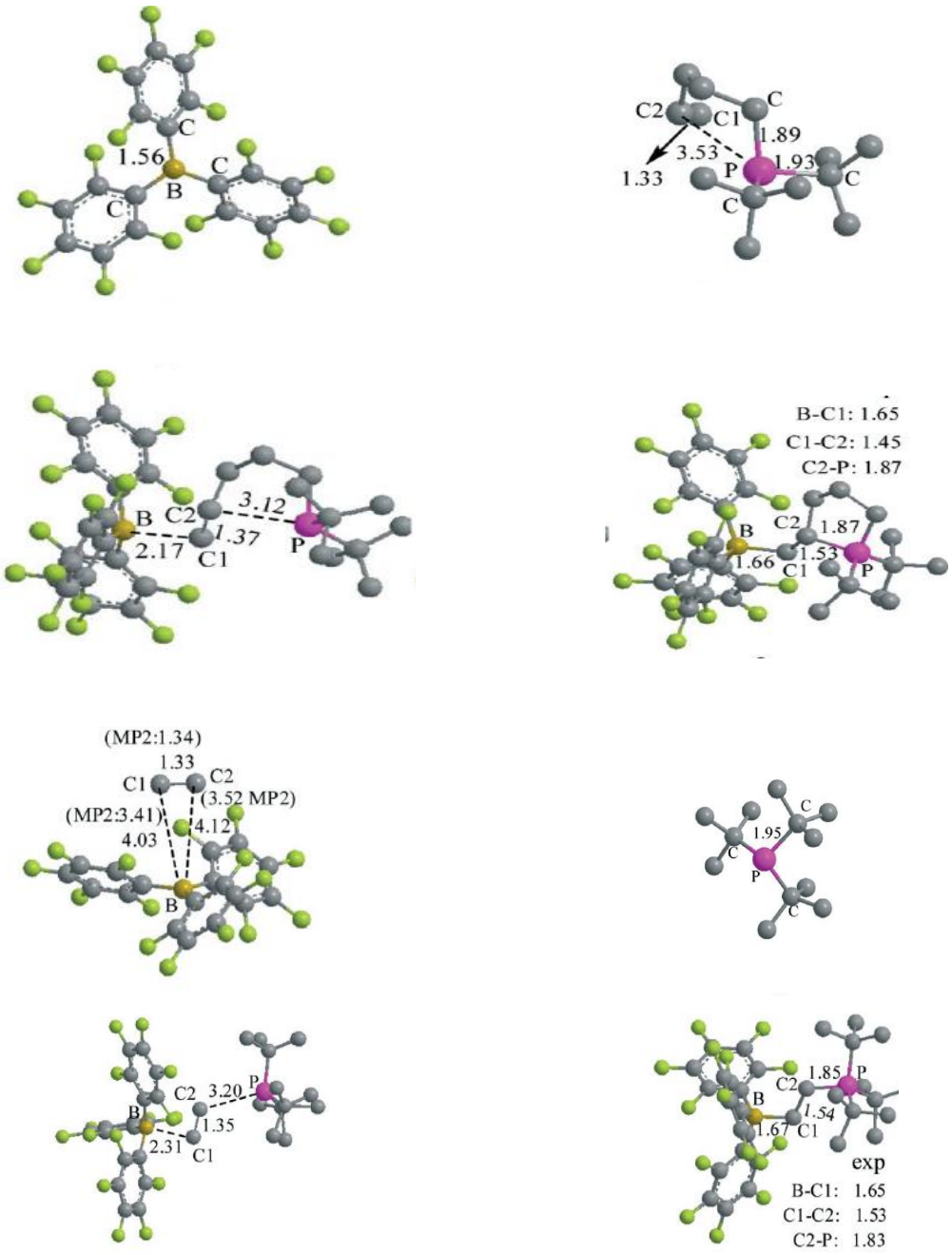

Figure 1.17 Calculated transition states and products from reference 46.

1.7 Reaction of FLPs with terminal alkynes

Iashin and coworkers[47] (Scheme 1.25) have reported a new FLP formed by reaction between 1,2,2,6,6-pentamethylpiperidine (PMP) and boron trifluoride unit. This pair reacts with terminal acetylenes to give the products of C(sp)-H borylation as tetra- or trialkynylboron compounds and pentamethylpiperidinium tetrafluoroborate. Details of the mechanism were investigated using the dispersion-corrected range-separated hybrid functional wB97X-D along with the 6-311G(d,p) basis set. Since PMP shows efficient C-H borylation and can also be readily recovered, it represents an atom-efficient approach for synthesis of new organofluoroborate compounds.

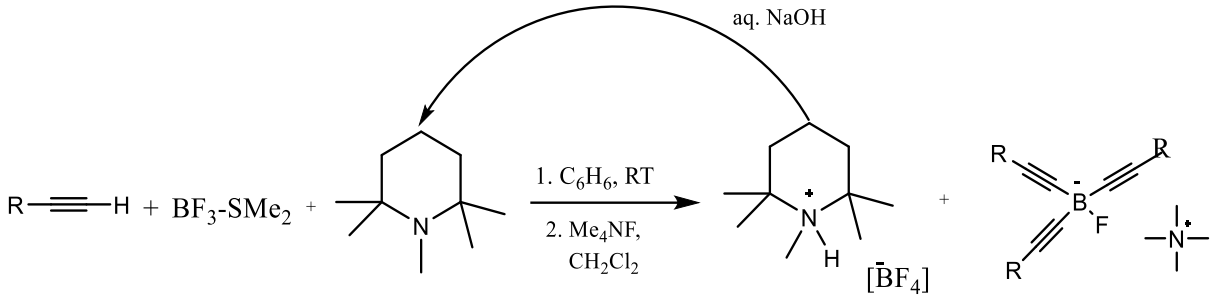

Scheme 1.25 Reaction of FLP with terminal acetylenes to give the products of C(sp)-H borylation as tetra- or trialkynylboron compounds and pentamethylpiperidinium tetrafluoroborate.

Chernichenko and co-workers[48] (Scheme 1.26) have utilized computational techniques to elucidate the mechanism for chemoselective and stereoselective hydrogenation of internal alkynes into the respective cis-alkenes under mild conditions using ansa-aminohydroborane as a catalyst. Dispersion-corrected ωB97X-D exchange-correlation functional, was utilized to study the possible reaction pathways.

The 6-311G(d,p) polarized triple-ζ valence basis set was used for geometry optimizations while the larger 6-311++G(3df,3pd) basis set was utilized for single point energy calculations. Calculations along with the experimental results have revealed the mechanism to be of three steps: Firstly, hydroboration of alkyne (substrate binding), followed by heterolytic H_2 cleavage with formed vinylborane, and finally intramolecular protodeborylation of vinyl substituent which recovers catalyst and releases the *cis*-alkene.

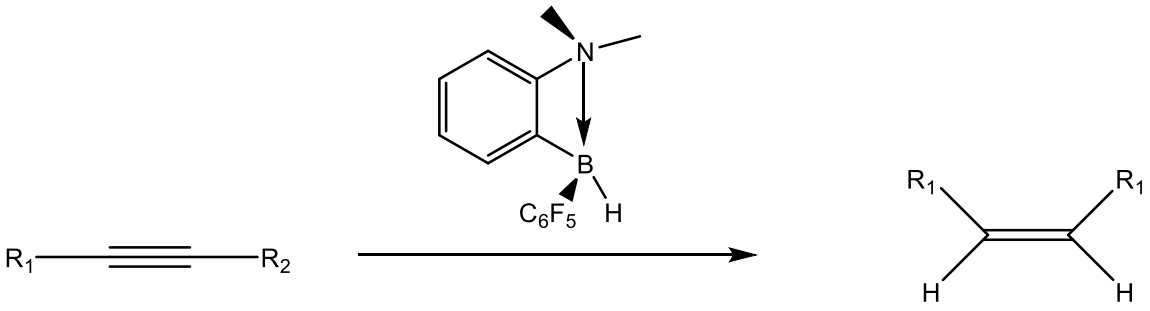

Scheme 1.26 Hydrogenation of internal alkynes into the respective cis-alkenes under mild conditions using ansa-aminohydroborane as a catalyst.

1.8 Regio-selectivity, steric effects, London dispersion and Covalent Interactions in FLPs

Using M06-2X with triple-zeta split-valence basis set, 6-311+G(d), Liu and co-workers[49] have utilized electrostatic potential to predict regioselectivity and steric force to stereochemical inclination of numerous chemical processes including FLPs like $Me_2P\text{-}CH_2CH_2\text{-}BMe_2$.

Bistoni and co-workers[50] have done detailed theoretical investigations on a series of classical adducts as well as FLPs formed by tris(pentafluorophenyl)borane and

various substituents like phosphines, carbenes and amines to understand the role of London dispersion in these compounds. For this study they have utilized domain based local pair natural orbital coupled-cluster (DLPNO-CCSD(T)) method along with Local Energy Decomposition (LED) analysis. Studies have confirmed that London dispersion forces govern the stability in classical adducts as well as FLPs. It has been found that by increasing the steric bulk near the basic centre this effect is augmented, but steric hindrance increases the energy required to bring the fragments close to one another for interaction. Hence tuning is required by choosing the substituents carefully.

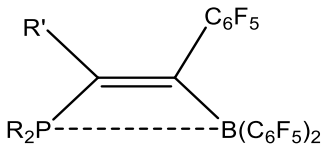

1. R=mes, R'=Ph
2. R=Ph, R'=Ph
3. R=Ph, R'=*n*-propyl
4. R=Ph, R'=PPh2
5. R=mes, R'=tolyl
6. R=Ph, R'=me

Figure 1.18 FLPs composed of substituted vinylene linked intramolecular phosphane–borane adducts.

Wiegand and co-workers[51] have studied covalent interactions between the Lewis acid and Lewis base functionalities in a series of FLPs composed of substituted vinylene linked intramolecular phosphane–borane adducts (Figure 1.18) using solid-state nuclear magnetic resonance techniques and DFT calculations. The geometry optimizations were performed on a DFT meta-GGA (TPSS) level of theory (starting with the crystal structure if available) employing D3 dispersion correction and Ahlrich's def2-TZVP basis set. The calculations of the electric field gradients were performed on a GGA DFT level (functional B97-D). Studies indicate complete suppression of covalent interactions between the Lewis acid and base centres may not be present. In fact, they suggest that the residual electron density between the reaction centres may be a necessary requirement for the typical FLP behaviour.

1.9 Reactions by some novel boron compounds

Clarke and co-workers[52] have reported the formation of some novel di- and triazaborines formed by insertion of NHC-carbene in B-H bond of 9BBN (9-Borabicyclo [3.3.1] nonane) followed by ring expansion (Scheme 1.27). M06-2X/6-311G(d,p) level of theory with PCM model for THF have been used to probe the regioselectivity observed in this mechanism. It has been found that the initial migration of hydride from B to carbene constitutes the rate determining step. It is thought that the regioselectivity seen in this mechanism may be attributed to the energy difference between alkyl migration and ring expansion step which favours migration in ylide formed from attack of N1.

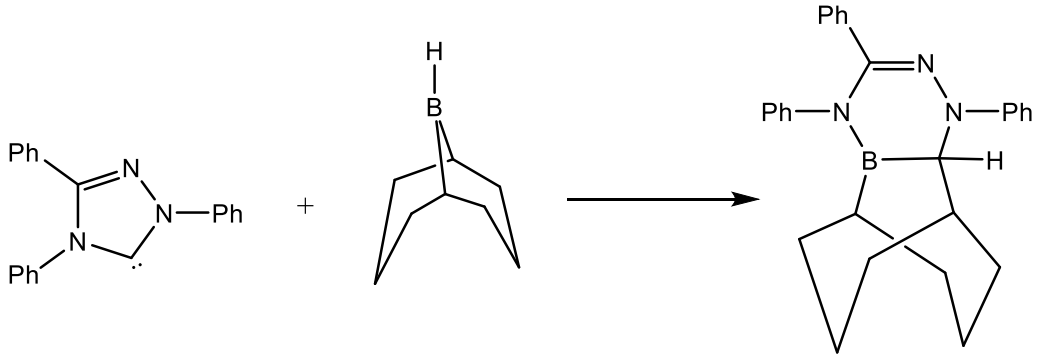

Scheme 1.27 Insertion of NHC-carbene in B-H bond of 9BBN (9-Borabicyclo [3.3.1] nonane) followed by ring expansion.

Devillard and co-workers[53] (Scheme 1.28) have utilized intramolecular pyridine-stabilized silylium hydroborate ion-pair, formed by reaction between tertiary silane 2-[(diphenylsilyl)methyl]-6-methylpyridine and tris(pentafluorophenyl)borane (BCF), to cleave CO bond in carbon monoxide. Cleavage leads to the formation of a complex (B-(diarylmethyl)-B-aryl-boryloxysilane) with double C-C_{sp2} bond formation which further reacts with pinacol to form bis(pentafluorophenyl)-methane. This reaction system has been studied computationally using BP86-D3/def2-TZVP. Studies reveal

that deoxygenation of CO leading to the formation of new C-C bonds is possible without using transition metals.

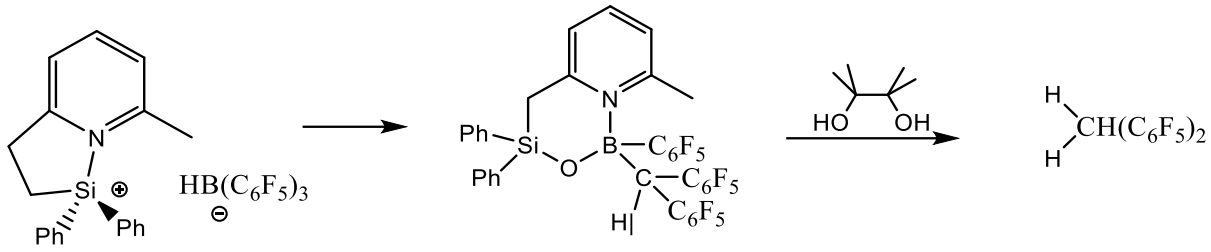

Scheme 1.28 Cleavage of CO by intramolecular pyridine-stabilized silylium hydroborate ion-pair.

Thakur and co-workers[54] (Scheme 1.29) have reported an abnormal N-heterocyclic carbene (*a*NHC), 1,3-bis(2,6-diisopropylphenyl)-2,4-diphenylimidazol-5-ylidene which along with $B(C_6F_5)_3$ is capable of activating CO_2 and N_2O much more effectively than sterically demanding *n*NHC/$B(C_6F_5)_3$ system containing 1,3-di-*tert*-butylimidazolin-2-ylidene. aNHC/$B(C_6F_5)_3$ reagent system is also capable of effective ring opening in tetrahydrofuran and tetrahydrothiophene. M05-2X/6-311G level of theory was utilized. The calculations revealed that the adduct is energetically much less stable than the products it forms afterwards. It is envisaged that this may indeed be the driving for the reaction.

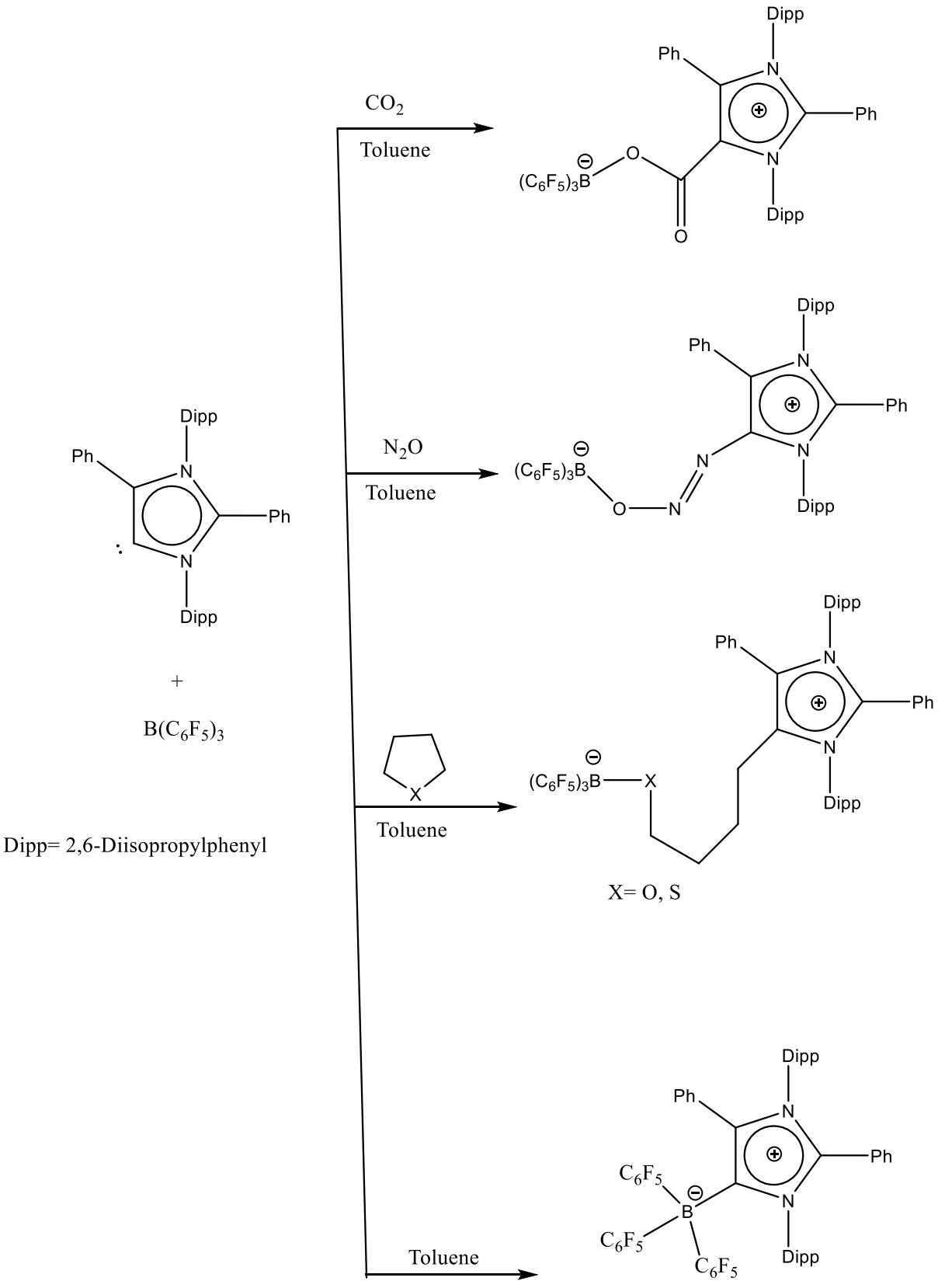

Scheme 1.29 Activation of CO_2, N_2O and THF by an abnormal N-heterocyclic carbene (*a*NHC).

Zeng and co-workers[55] have explored pincer-type phosphorus compounds theoretically for the hydrogenation of carbon dioxide with ammonia−borane. Geometry optimization was done utilizing B3PW91 functional while electronic energies were computed by ONIOM(CCSD(T):MP2) or CCSD(T). Studies reveal that these compounds are quite efficient for hydrogenation which proceeds via phosphorus - ligand cooperative catalysis. Further, the activity of the catalyst is more if phosphorus has NNN ligand rather than ONO ligand.

Von Grotthuss and co-workers[56] have reported a new class of molecules prepared by injecting two electrons to 9,10-dihydro-9,10-diboraanthracene (DBA) which show ambiphilic behaviour like metals towards hydrogen. B2GP-PLYP-D/CBS (T, Q)// SMD-PBE0D/6-31+G(d,p) level of theory have been utilized to investigate the intricacies of the mechanism. Studies have revealed that this new class of MGA's (Main Group Ambiphiles) unlike FLPs undergo homolytic cleavage (like transition metals) under mild conditions. Li_2[DBA]/H_2 system has been shown to successfully convert Me_3SiCl into Me_3SiH.

1.10 References

1. H. Brown, H. Schlesinger and S. Cardon, *Journal of the American Chemical Society*, 1942, 64, 325-329.

2. G. Wittig and E. Benz, *Chemische Berichte*, 1959, 92, 1999-2013.

3. W. Tochtermann, *Angewandte Chemie International Edition in English*, 1966, 5, 351-371.

4. D. Parks and W. Piers, *Journal of the American Chemical Society*, 1996, 118, 9440-9441.

5. G. Welch, R. Juan, J. Masuda and D. Stephan, *Science*, 2006, 314, 1124-1126.

6. G. Welch and D. Stephan, *Journal of the American Chemical Society*, 2007, 129, 1880-1881.

7. J. McCahill, G. Welch and D. Stephan, *Angewandte Chemie International Edition*, 2007, 46, 4968-4971.

8. M. Mane and K. Vanka, *ChemCatChem*, 2017, 9, 3013-3022.

9. Z. Dong, Z. Li, X. Liu, C. Yan, N. Wei, M. Kira and T. Müller, *Chemistry - An Asian Journal*, 2017, 12, 1204-1207.

10. É. Dorkó, B. Kótai, T. Földes, Á. Gyömöre, I. Pápai and T. Soós, *Journal of Organometallic Chemistry*, 2017, 847, 258-262.

11. K. Chernichenko, B. Kótai, M. Nieger, S. Heikkinen, I. Pápai and T. Repo, *Dalton Trans.*, 2017, 46, 2263-2269.

12. L. Liu, B. Lukose and B. Ensing, *Journal of Physical Chemistry C*, 2017, 121, 2046-2051.

13. É. Rochette, N. Bouchard, J. Légaré Lavergne, C. Matta and F. Fontaine, *Angewandte Chemie International Edition*, 2016, 55, 12722-12726.

14. M. Courtemanche, É. Rochette, M. Légaré, W. Bi and F. Fontaine, *Dalton Transactions*, 2016, 45, 6129-6135.

15. K. Wang, K. Tang and J. Zhang, *International Journal of Hydrogen Energy*, 2016, 41, 18963-18970.

16. D. Yepes, P. Jaque and I. Fernández, *Chemistry - A European Journal*, 2016, 22, 18801-18809.

17. V. Zhivonitko, K. Sorochkina, K. Chernichenko, B. Kótai, T. Földes, I. Pápai, V. Telkki, T. Repo and I. Koptyug, *Physical Chemistry Chemical Physics*, 2016, 18, 27784-27795.

18. P. Pérez, D. Yepes, P. Jaque, E. Chamorro, L. Domingo, R. Rojas and A. Toro-Labbé, *Physical Chemistry Chemical Physics*, 2015, 17, 10715-10725.

19. E. Clark and M. Ingleson, *Angewandte Chemie International Edition*, 2014, 53, 11306-11309.

20. T. Rokob, I. Bakó, A. Stirling, A. Hamza and I. Pápai, *Journal of the American Chemical Society*, 2013, 135, 4425-4437.

21. L. Hounjet, C. Bannwarth, C. Garon, C. Caputo, S. Grimme and D. Stephan, *Angewandte Chemie*, 2013, 125, 7640-7643.

22. L. Greb, P. Oña-Burgos, B. Schirmer, S. Grimme, D. Stephan and J. Paradies, *Angewandte Chemie*, 2012, 124, 10311-10315.

23. Y. Guo, X. He, Z. Li and Z. Zou, *Inorganic Chemistry*, 2010, 49, 3419-3423.

24. T. Rokob, A. Hamza and I. Pápai, *Journal of the American Chemical Society*, 2009, 131, 10701-10710.

25. P. Chase, A. Gille, T. Gilbert and D. Stephan, *Dalton Transactions*, 2009, 7179.

26. M. Ghara and P. Chattaraj, *Structural Chemistry*, 2019, 30, 1067-1077.

27. V. Fasano, J. Radcliffe, L. Curless and M. Ingleson, *Chemistry - A European Journal*, 2016, 23, 187-193.

28. J. Cabrera-Trujillo and I. Fernández, *Chemical Communications*, 2019, 55, 675-678.

29. É. Rochette, H. Boutin and F. Fontaine, *Organometallics*, 2017, 36, 2870-2876.

30. J. Légaré Lavergne, A. Jayaraman, L. Misal Castro, É. Rochette and F. Fontaine, *Journal of the American Chemical Society*, 2017, 139, 14714-14723.

31. C. Tang, Q. Liang, A. Jupp, T. Johnstone, R. Neu, D. Song, S. Grimme and D. Stephan, *Angewandte Chemie International Edition*, 2017, 56, 16588-16592.

32. K. Ye, M. Bursch, Z. Qu, C. Daniliuc, S. Grimme, G. Kehr and G. Erker, *Chem.Commun.*, 2017, 53, 633-635.

33. A. McQuilken, Q. Dao, A. Cardenas, J. Bertke, S. Grimme and T. Warren, *Angewandte Chemie International Edition*, 2016, 55, 14335-14339.

34. W. Nzahou Ottou, E. Conde-Mendizabal, A. Pascual, A. Wirotius, D. Bourichon, J. Vignolle, F. Robert, Y. Landais, J. Sotiropoulos, K. Miqueu and D. Taton, *Macromolecules*, 2017, 50, 762-774.

35. D. Boom, A. Jupp, M. Nieger, A. Ehlers and J. Slootweg, *Chemistry – A European Journal*, 2019, 25, 13299-13308.

36. D. Zhu, Z. Qu and D. Stephan, *Dalton Transactions*, 2020, 49, 901-910.

37. É. Rochette, M. Courtemanche and F. Fontaine, *Chemistry - A European Journal*, 2017, 23, 3567-3571.

38. M. Sajid, A. Klose, B. Birkmann, L. Liang, B. Schirmer, T. Wiegand, H. Eckert, A. Lough, R. Fröhlich, C. Daniliuc, S. Grimme, D. Stephan, G. Kehr and G. Erker, *Chem. Sci.*, 2013, 4, 213-219.

39. Adenot, N. von Wolff, G. Lefèvre, J. Berthet, P. Thuéry and T. Cantat, *Chemistry – A European Journal*, 2019, 25, 8118-8126.

40. L. Wang, S. Dong, C. Daniliuc, L. Liu, S. Grimme, R. Knitsch, H. Eckert, M. Hansen, G. Kehr and G. Erker, *Chemical Science*, 2018, 9, 1544-1550.

41. I. Peuser, R. Neu, X. Zhao, M. Ulrich, B. Schirmer, J. Tannert, G. Kehr, R. Fröhlich, S. Grimme, G. Erker and D. Stephan, *Chemistry - A European Journal*, 2011, 17, 9640-9650.

42. C. Mömming, E. Otten, G. Kehr, R. Fröhlich, S. Grimme, D. Stephan and G. Erker, *Angewandte Chemie International Edition*, 2009, 48, 6643-6646.

43. J. Pereira, M. Sajid, G. Kehr, A. Wright, B. Schirmer, Z. Qu, S. Grimme, G. Erker and P. Ford, *Journal of the American Chemical Society*, 2013, 136, 513-519.

44. M. Sajid, A. Stute, A. Cardenas, B. Culotta, J. Hepperle, T. Warren, B. Schirmer, S. Grimme, A. Studer, C. Daniliuc, R. Fröhlich, J. Petersen, G. Kehr and G. Erker, *Journal of the American Chemical Society*, 2012, 134, 10156-10168.

45. E. Otten, R. Neu and D. Stephan, *Journal of the American Chemical Society*, 2009, 131, 9918-9919.

46. Y. Guo and S. Li, European Journal of Inorganic Chemistry, 2008, 2501-2505.

47. V. Iashin, K. Chernichenko, I. Pápai and T. Repo, *Angewandte Chemie International Edition*, 2016, 55, 14146-14150.

48. K. Chernichenko, Á. Madarász, I. Pápai, M. Nieger, M. Leskelä and T. Repo, *Nature Chemistry*, 2013, 5, 718-723.

49. S. Liu, C. Rong and T. Lu, *Phys. Chem. Chem. Phys.*, 2017, 19, 1496-1503.

50. G. Bistoni, A. Auer and F. Neese, *Chemistry - A European Journal*, 2016, 23, 865-873.

51. T. Wiegand, H. Eckert, O. Ekkert, R. Fröhlich, G. Kehr, G. Erker and S. Grimme, *Journal of the American Chemical Society*, 2012, 134, 4236-4249.

52. J. Clarke, P. Eisenberger, S. Piotrkowski and C. Crudden, *Dalton Transactions*, 2018, 47, 1791-1795.

53. M. Devillard, B. de Bruin, M. Siegler and J. van der Vlugt, *Chemistry - A European Journal*, 2017, 23, 13628-13632.

54. A. Thakur, P. Vardhanapu, G. Vijaykumar, P. Kumar Hota and S. Mandal, *European Journal of Inorganic Chemistry*, 2016, 2016, 913-920.

55. G. Zeng, S. Maeda, T. Taketsugu and S. Sakaki, *Journal of the American Chemical Society*, 2016, 138, 13481-13484.

56. E. von Grotthuss, M. Diefenbach, M. Bolte, H. Lerner, M. Holthausen and M. Wagner, *Angewandte Chemie International Edition*, 2016, 55, 14067-1407.

Chapter-2 Theoretical Background

2.1 Background

The basis of computational chemistry is Schrödinger equation, which was postulated in 1926 by Erwin Schrödinger[1] to model the spectrum of the hydrogen atom. This equation is exactly solvable for one electron systems like hydrogen, but it has been extended to larger systems as well. Time independent Schrödinger equation is written as:

$$\hat{H}(r,R)\psi(r,R) = E(R)\psi(r,R) \qquad 2.1$$

Here, $\hat{H}$ is the Hamiltonian operator, E is the total energy and ψ is the wave function. The operator explicitly depends on electronic coordinates (r) and nuclear coordinates (R). Hamiltonian operator is the sum of two operators: the kinetic energy operator and the potential energy operator.

$$\hat{H} = \hat{T} + \hat{V} \qquad 2.2$$

Kinetic energy operator requires taking into account momentum operator and is written as follows:

$$\hat{T} = -\frac{h^2}{2m}\left(\frac{\partial^2}{\partial x^2} + \frac{\partial^2}{\partial y^2} + \frac{\partial^2}{\partial z^2}\right) \qquad 2.3$$

Where m is the mass. Mathematicians call the set of second order derivative operators in the kinetic energy operator the Laplacian, and indicate it by ∇^2. In those terms, the kinetic energy operator can be written more concisely as:

$$\hat{T} = -\frac{h^2}{2m}\nabla^2 \qquad 2.4$$

In the absence of external influences like electric field, magnetic field and relativistic effects, the Hamiltonian operator can be split into kinetic energy of the nuclei ($\hat{T}_N$) and the electrons ($\hat{T}_e$), and the potential energy of the nuclear-nuclear repulsion ($\hat{V}_{NN}$), the electron-electron repulsion ($\hat{V}_{ee}$) and the electron-nuclear attraction ($\hat{V}_{eN}$).

$$\hat{H} = -\sum_{\mathrm{i}} \frac{\hbar}{2m_e} \nabla_i^2 - \sum_{\mathrm{k}} \frac{\hbar}{2m_k} \nabla_k^2 - \sum_{\mathrm{i}} \sum_{\mathrm{k}} \frac{e^2 Z_k}{r_{ij}} + \sum_{\mathrm{i<j}} \frac{e^2}{r_{ij}} + \sum_{\mathrm{k<l}} \frac{e^2 Z_k Z_l}{r_{kl}} \qquad 2.5$$

Where i and j denote electrons, k and l are nuclei, $\hbar$ is Planck's constant divided by 2π, m_e and m_k are masses of the electron and nucleus, e is the charge of the electron and Z is the atomic number and r_{kl} is the distance between nucleus k and l.

The most basic concept in solving the quantum mechanical problems is Born-Oppenheimer approximation. This approximation is based on the fact that mass of the atomic nucleus is much more than the mass of the electron and hence we can neglect kinetic energy term (due to acceleration of atomic nuclei) from Hamiltonian equation[2] as it is very small. Thus, the Schrödinger equation after application of Born-Oppenheimer approximation becomes:

$$\hat{H}_{elec}(r, R)\psi_e(r, R) = E_e(R)\psi_e(r, R) \qquad 2.6$$

Here, $\psi_e(r, R)$ is the electronic wavefunction that is a function of electronic as well as nuclear coordinates. Electronic coordinates (r are independent variables whereas the nuclear coordinates (R) are parameters. This approximation is applied only for the fixed atoms in the molecule and therefore not enough for solving many electronic systems. Hence, further approximations are needed.

Hartree in 1927[3-5], proposed a new Self Consistent Field (SCF) method to calculate wave function and energy of atoms using fundamental physical parameters (*ab initio*) rather than empirical parameters. His solutions came to be known as Hartree method

or Hartree product. Later, Fock improved Hartree's method by using "antisymmetrized wavefunctions" (called the Hartree-Fock method)[6] instead of simple one-electron wavefunctions. This gave rise to equation similar to Schrödinger equation:

$$\hat{F}|\varphi_i\rangle = \epsilon_i|\varphi_i\rangle \qquad 2.7$$

Where, $\hat{F}$ is Fock operator and $|\varphi_i\rangle$ are Hartree-Fock orbitals corresponding to energy ϵ_i. The Fock operator is a one-electron operator and solving a Hartree-Fock equation gives the energy and Hartree-Fock orbital for one electron. The wavefunction written as a Slater determinant of spin-orbitals is necessary to derive Fock operator.

$$\hat{F} = \hat{H}^0 + \sum_{J=1}^{N}\left(2\hat{J}_J - \hat{K}_J\right) = -\frac{\hbar^2}{2m}\bar{V}^2 - \frac{Ze^2}{4\pi\epsilon_0 r} + \sum_{J=1}^{N}\left(2\hat{J}_J - \hat{K}_J\right) \qquad 2.8$$

Where, $\hat{J}$ is the Coulomb operator**,** representing the electron-electron repulsion energy due to each of the two electrons in the j[th] orbital. $\hat{K}$ is the exchange operator, representing the electron exchange energy due to the antisymmetry of the total n-electron wavefunction. In the Hartree-Fock approximation, the electron correlation energy is avoided. The difference between the *HF* energy and energy for the full Schrödinger equation is called correlation energy.

2.2 Density Functional Theory (DFT)

Density Functional Theory (DFT) is based on the electron density rather than the wavefunction as this is a physically observable quantity unlike the wavefunction and depends only on 3 coordinates instead of 3N degrees of freedom.

A functional is denoted as follows:

$$y = F[f(x)] \qquad 2.9$$

Here, the value of y is dependent on another function. The first $f(x)$ function becomes the input for the functional, that is, a function of a function.

In DFT methods, the energy of the molecule is a functional of the electron density. Electron density is a function, with three variables: x, y and z-position of the electrons. Regardless of the number of electrons, the electron density is always only dependent on those three numbers. The functional (F) of electron density gives us the energy of the molecule.

$$Electron\ Density = \rho(x, y, z) \quad 2.10$$

$$Energy = F[\rho(x, y, z)] \quad 2.11$$

The Thomas-Fermi (TF) model proposed by Thomas[7] and Fermi[8] in 1927 is the predecessor to modern DFT. In this method, they used the electron density $\rho(r)$ as the basic variable. The total energy of the electrons is the sum of their kinetic and potential energies.

$$E = T + U_{eN} + U_{ee} \quad 2.12$$

Where T is the kinetic energy of the non-interacting electrons in a homogeneous electron gas (HEG), U_{eN} is the potential energy of an atom's electrons, due to electron-nucleus Coulomb interaction, U_{ee} is the potential energy of the electrons due to their mutual repulsion. The total energy of a system in an external potential $V_{ext}(r)$ is written as a functional of the electron density $\rho(r)$.

The limitation of the Thomas-Fermi model was that exchange and correlation among electrons was not considered. In 1930 Dirac[9] modified Thomas-Fermi equation by adding local exchange. The ground state density and energy can be obtained by minimizing the Thomas-Fermi-Dirac equation is subject to conservation of the total

number (N) of electrons. The major drawback of this theory is that fails to describe bonding between atoms, thus molecules and solids cannot form in this theory. Although this model had its limitations, its concept to use electron density as the basic variable illustrated the way DFT works.

In 1964 a landmark paper by Hohenberg and Kohn[10] appeared in the Physical Review that reported theorems that represent the major theoretical pillars on which all modern-day density functional theory is erected. The first theorem states that the external potential $V_{ext}(\vec{r})$ is (to within a constant) a unique functional of $\rho(\vec{r})$' since, in turn $V_{ext}(\vec{r})$ fixes $\widehat{H}$ we see that the full many particle ground state is a unique functional of $\rho(\vec{r})$. The second theorem states that $F_{HK}[\rho]$, the functional that delivers the ground state energy of the system, delivers the lowest energy if and only if the input density is the true ground state density.

The major drawback of the DFT was that although the attempt of pure (or "orbital free") DFT to compute the energy of interacting electrons, as a functional of the density was correct in principle, it was not very accurate. In addition, there was lack of accurate approximation for kinetic energy functional. Kohn and Sham[11] in 1965 gave equations in order to take advantage of the power of DFT without sacrificing accuracy (i.e. including exchange and correlation effects) to map the problem of the system of interacting electrons onto a fictitious system of "non-interacting electrons". In 1998 Walter Kohn was honoured with a Nobel Prize for development of DFT.

The local density approximation is the simplest approximation over all other approximations for the E_{XC} term. It is the basis of all approximate exchange-correlation functionals. At the centre of this model is the idea of a uniform electron gas. This is a system in which electrons move on a positive background charge distribution such

that the total ensemble is neutral. In LDA, the XC energy per electron at a point r is considered the same as that for a homogeneous electron gas (HEG) that has the same electron density at the point $\vec{r}$. The total exchange-correlation functional $E_{xc}[\rho(r)]$ can be written as

$$E_{xc}^{LDA}[\rho] = \int \rho\,(\vec{r})\epsilon_{XC}(\rho(\vec{r}))\,d\vec{r} \qquad 2.13$$

Here, ϵ_{xc} $(\rho(\vec{r}))$ is the exchange-correlation energy per particle of a uniform electron gas of density $\rho(\vec{r})$. This energy per particle is weighted with the probability $\rho(\vec{r})$ that there is an electron at this position. The quantity ϵ_{xc} $(\rho(\vec{r}))$ can be further split into exchange and correlation contributions,

$$\epsilon_{xc}\,(\rho(\vec{r})) = \epsilon_X(\rho(\vec{r})) + \epsilon_C(\rho(\vec{r}) \qquad 2.14$$

The accuracy of the LDA for the exchange energy is within 10%, while the smaller correlation energy is generally overestimated by up to a factor 2. These two errors partially cancel each other. As the electron density in molecules is not constant as in uniform electron gas, the performance of LDA for molecules is worse compared to the other approximations that will be discussed in the forthcoming sections, especially in chemical bond energies. Different local density approximations were proposed including Vosko-Wilk-Nusair[12] (VWM), Perdew-Zunger[13] (PZ81), Cole-Perdew[14] (CP) and Perdew-Wang[15] (PW92) depending on the analytic forms used for ϵ_C. For unrestricted systems, the LDA extended to local spin-density approximation (LSD), in which exchange-correlation energy per particle in a homogenous, spin-polarized electron gas with spin-up and spin-down electrons considered separately.

The major drawback of the LDA was that it neglected the inhomogeneities of the real charge density which could be very different from the HEG. Hence the first logical step to go beyond LDA was to supplement the density with information about the gradient of the charge density, $\nabla \rho(\vec{r})$ in order to account for the non-homogeneity of the true electron density. The exchange-correlation energy in this form is termed as Generalized Gradient Approximation (GGA). Widely used GGAs include the forms proposed by Becke[16] (B88), Perdew *et al.*[17] and Perdew, Burke and Enzerhof[18] (PBE). GGA is better than LDA in predicting bond length and binding energy of molecules, crystal lattices etc, in systems where the charge density varies rapidly. However, sometimes GGA overcorrects LDA results in ionic crystals. Both LDA and GGA perform badly in materials where the electrons tend to be localized and strongly correlated such as transition metal oxides and rare-earth elements and compounds. This drawback leads to approximations beyond LDA and GGA.

Functionals that are more accurate than GGA include the meta-GGA functionals that include second derivative of the electron density (the Laplacian), whereas GGA includes only the density and its first derivative, *e.g* Tao, Perdew, Staroverov, and Scuseria[19] (TPSS). In general, meta-GGAs tend to outperform GGAs for atomisation energies and barrier heights, and a few can even incorporate some 'medium-range' dispersion. However, meta-GGA functionals tend to be more sensitive to the integration grid relative to GGAs, and care must be taken when dealing with weakly interacting systems.

The next improvement in this field were hybrid functionals, a class of approximations that incorporate a portion of exact exchange from Hartree–Fock theory with the rest of

the exchange–correlation energy from other sources (ab initio or empirical). In 1993, a hybrid functional was derived by the mixing of exact exchange with LSD and GGA functional, weighted by three empirical parameters (B3). This functional is called B3LYP ("Becke, 3-parameter, Lee–Yang–Parr")[20,21], is expressed as,

$$E_{xc}^{B3LYP} = (E_x^{LDA} + a_0\,(E_x^{HF} - E_x^{LDA}) + a_x\,(E_x^{GGA} - E_x^{LDA}) + E_c^{LDA} + a_c\,(E_c^{GGA} - E_c^{LDA}) \quad 2.15$$

Where $a_0 = 0.20,\ a_x = 0.72\ and\ a_c = 0.81.$ E_x^{GGA} and E_c^{GGA} are generalized gradient approximations: the Becke 88 exchange functional and the correlation functional of Lee, Yang and Parr for B3LYP, and E_c^{LDA} is the VWN local-density approximation to the correlation functional.

The most recent functionals in this category are meta-hybrid GGA functionals, which are constructed empirically by fitting their parameters for contribution of HF and higher order derivatives of ρ. The M06[22] suite of functionals is a set of four meta-hybrid GGA and meta-GGA functionals. The family includes the functionals M06-L, M06, M06-2X and M06-HF, with a different amount of exact exchange for each one. M06-L is fully local without HF exchange (thus it cannot be considered hybrid), M06 has 27% HF exchange, M06-2X 54% and M06-HF 100%.

The advantages and usefulness of each functional are

- M06-L: Fast, good for transition metals, inorganic and organometallics.
- M06: For main group, organometallics, kinetics and non-covalent bonds.
- M06-2X: Main group, kinetics.
- M06-HF: Charge-transfer TD-DFT, systems where self-interaction is pathological.

2.3 Basis Set

A major approximation in computational chemistry is the one used for representation of molecular orbitals. A basis set is a set of functions (called basis functions) which are combined in linear combinations to create molecular orbitals. The exact molecular orbital is constructed from infinite basis set. In the calculations, the exact molecular orbital is replaced by a finite set of algebraic functions. Basis functions are usually called as atomic orbital (AO) basis. Two types of basis functions are generally used, Slater type orbitals (STOs) and Gaussian Type orbitals (GTOs). The expression for given STO is:

$$\phi_{STO}(r,\theta,\gamma) = NY_{l,m}(\theta,\gamma)r^{n-1}e^{-\zeta r} \qquad 2.16$$

Where *N* is a normalized constant, ζ called exponent. The *r*, θ, γ are spherical coordinates. The *n*, *l* and *m* are principal, angular momentum and magnetic quantum numbers respectively. As STOs are computationally demanding, it was realized by Frank Boys that STOs could be approximated as linear combinations of Gaussian-type orbitals (GTOs) instead. The expression for GTO is:

$$\phi_{GTO}(r,\theta,\gamma) = NY_{l,m}(\theta,\gamma)r^{2n-2-1}e^{-\zeta r^2} \qquad 2.17$$

The only difference between the STO and GTO is in the "*r*". The GTO squares the "*r*" so that the product of the gaussian "primitives" (original gaussian functions) is another gaussian. By doing this, we have an equation we can work with and so the equation is much easier. However, the price we pay is loss of accuracy. To compensate for this loss, it is observed that the more gaussian functions we combine, the more accurate our equation. The smallest basis set is called as the minimal basis set, and it contains one function for each atomic orbital of an atom, i.e. one s-function for hydrogen and helium and two s-functions and one set of p-functions for the first row in the periodic table. All basis set equations in the form STO-NG (where N represents the number of

GTOs combined to approximate the STO) are considered to be "minimal" basis sets. In the minimal basis set it is assumed that all the orbitals are of same shape which is in really not true.

The "extended" basis sets, are then employed that consider more orbitals of the molecule and account for size and shape of molecular charge distributions. Double zeta basis set treats all the orbitals separately. Each orbital is expressed as the sum of two STOs in which both the equations are similar apart from the value of zeta. The zeta value accounts for how diffuse (large) the orbital is. The two STOs are then added in some proportion. The constant 'd' determines how much each STO will count towards the final orbital. The size of the atomic orbital can range anywhere between the value of either of the two STOs.

$$\phi_{2s}(r) = \phi_{2s}^{STO}(r, \zeta_1) + d\phi_{2s}^{STO}(r, \zeta_2 \qquad 2.18$$

For example, in the above case of 2s orbital each STO represent different size of orbital as the value of zeta is different. The value of 'd' accounts for the percentage of the second STO to add in. The linear combination of two STOs then gives us the atomic orbital. Since each of the two equations are the same, the symmetry remains constant. The triple and quadruple-zeta basis sets work the same way, except use three and four Slater equations instead of two.

Often these calculations are very tedious and consume much time. Therefore, the matter is simplified by calculating equations only for the valence electrons and not for the core electrons as they do not change between atom and molecule for which

minimal basis set is adequate and hence, they are represented by only one Slater orbital. This method is called split valence basis set method. Doubling the number of basis functions for valence electrons can improve the basis set and is called valence double zeta basis. If there are three times as many basis functions as in a minimum basis, it is called a triple zeta valence, and quadruple zeta valence for four times and so on.

Additional improvements can also be made to the basis sets using polarization functions and/or diffuse functions. Bonding between atoms induces a deformation of the electron cloud around each atom, called polarization. To incorporate this feature, functions with higher angular momentum are added to the basis set. For example, the addition of a p function to H allows polarization. In the same way a d-function can be added to a basis set containing p valence orbitals, f-functions for d-valence orbitals. For example, to the 6-31G basis set d-functions on main group elements and p-functions on H can be added, the basis set becoming 6-31G(d,p). The diffuse functions are represented by a + (for example 6-31+G or 6-31++G) that describe the part of atomic orbitals distant from the nuclei that can have a very important role when considering anions or diffuse electronic clouds in second or third row transition metals.

2.4 Potential Energy Surface (Optimization, TS, Scans)

Potential energy surface (PES) is the relationship between energy of the molecule and its geometry. PES is constructed on the basis of Born-Oppenheimer approximation, according to which electrons move much faster than the nuclei since nuclei have much more mass than the electrons. Therefore, nuclei are fixed as compared to the movement of the electrons. A detailed understanding of the mechanism of a reaction

requires knowledge of the PES. The most interesting points on PES's are the stationary points, where the gradients with respect to all internal coordinates are zero.

In a given PES, minima correspond to stable or quasi-stable species, i.e., reactants, products and intermediates. Transition states are saddle points which are minima in all dimensions but one; a maximum in that dimension. Higher-order saddle points are a minimum in all dimensions but n, where n >1; maximum in the other n dimensions. The Hessian index is the number of negative eigenvalues of the force constant matrix. For a stationary point, this corresponds to the number of internal degrees of freedom along which that point is a potential energy maximum. The Hessian index is 0 for minima, 1 for transition states, and >1 for higher-order saddle points.

A geometry optimization, when run to completion, will provide a stationary point geometry. Typically, this is a potential energy minimum. However, the optimization might get stuck on a saddle point. A vibrational analysis can verify the nature of the stationary point via the Hessian index.

Study of the reaction mechanism generally starts with the optimization of reactants and products. The optimized structures of the reactants and products are then modified to give starting guess for intermediates and the transition states. Sometimes a scan of whole length of coordinate, allowing other coordinates to relax in response to the scan, can also be used to probe the reaction mechanism. QST2 and QST3 methods lead to relatively more reliable transition state structures. In addition, multiple isomers for a particular structure also need to be optimized carefully as they often have very small energy difference between them. The relative stability of structures can

change depending on the local environment, the method used and the basis set. Optimized or TS structures have to be confirmed by a second calculation the "frequency analysis" which gives us the Hessian. We must also ensure that we are following the "right" reaction path, i.e. that the transition state we have found connects a particular reactant and product. This is achieved by carrying out an "Intrinsic Reaction Coordinate" or IRC analysis. The rate determining step is identified as the step having the highest barrier along the lowest energy reaction path.

2.5 Solvent model

The applicability of DFT as described so far is limited to gas-phase studies. To overcome this limitation, theoretical studies of molecular structure in condensed phase have become increasingly popular and different approaches have been developed. There are two major categories of solvent models: discrete models and a continuum model. The discrete or explicit model includes the solvent molecules in the calculations which means that all the effects of the solvent are calculated at the same level as the solute.

Unlike the discrete approach, in continuum or implicit model the solute/solvent energy is perturbed by the electrostatic interaction from a dielectric continuum solvent which means that the solvent is represented by a statistical average of the solvent molecules' conformation and properties. Continuum models[23] can make useful contributions when the solvent can be modelled by a single function i.e. it is not varying significantly from the bulk and the solvent is not an active constituent in the reaction or process. The polarizable continuum model (PCM) is a commonly used implicit model that is

based on Poisson-Boltzmann equation, which is an expansion of Poisson's equation. Solvation Models (SMx) (where x is an alphanumeric label to show the version) based on Born equation and the Solvation Model based on Density (SMD) are also widely used. The COSMO solvation model[24] is another popular implicit solvation model that uses a fast and robust approximation to the exact dielectric equations and reduces outlying errors as compared to PCM.

2.6 NBO, AIM and NCI Analysis

Natural bond orbital (NBO)[25] analysis is used in computational chemistry to calculate the distribution of electron density in atoms and in bonds between atoms. NBO analysis is based on a method for optimally transforming a given wave function into localized form, corresponding to the one-centre ("lone pairs") and two-centre ("bonds") elements of the chemist's Lewis structure picture. In NBO analysis, the input atomic orbital basis set is transformed via natural atomic orbitals (NAOs) and natural hybrid orbitals (NHOs) into natural bond orbitals (NBOs). The NBOs obtained in this fashion correspond to the widely used Lewis picture, in which two-centre bonds and lone pairs are localized. By comparing a set of molecules, we can predict the donor or acceptor effect of a particular substituent. It is a helpful tool for understanding the delocalization of the electron density, hyperconjugation effects and is very useful to to measure an inter- or intramolecular interaction.

Quantum theory of atoms in molecules (QTAIM)[26-28] analysis was developed by Bader and its basic motive is to exploit charge density or electron density of molecules as a vehicle to study the nature of bonding in molecular systems. The topology of the

electron density is used to define where one atom ends and the next begins. Each subsystem (or atom) is surrounded by a surface, through which the gradient vector field of the electron density $\vec{\nabla}\rho$ has no flux. The interatomic surfaces have the basic property that $\vec{\nabla}\rho$ is perpendicular to the unit vector normal to the surface, termed the local zero-flux equation,

$$\vec{\nabla}(\vec{r}).\vec{n}(\vec{r}) = 0 \qquad 2.19$$

Using 3 dimensions and the topology of the electron density, Bader described 4 types of critical points.

1. (3, -3) critical point: This is the position of a nucleus. The point therefore is also called a nuclear critical point.
2. (3, -1) critical point: This point is between two neighbouring atoms defining a bond between them. This point is therefore also called a bond critical point.
3. (3, +1) critical point: This point is to be found in the middle of several bonds forming a ring. It is also called a ring critical point.
4. (3, +3) critical point: This point is found when several rings form a cage and is therefore called a cage critical point.

This model predicts an exact quantum mechanical description where in a molecule bonds are. The topology works equally for covalent bonds as for non-covalent bonds. There is only one disadvantage that we need the electron density first to identify the critical points in space, but this can be obtained from HF, *ab initio* or DFT calculations. QTAIM is very useful tool to characterize the nature of bonding. In addition to the correct topological pattern of electron density, the integrated properties of atoms in molecules provide finer details on the bonding.

Non-Covalent Interactions (NCI) is a visualization index based on the Electron density (ρ) and the reduced density gradient (s). It is used to visualize non-covalent inter- and intramolecular interactions in three-dimensional space. NCI plots able to reveal both attractive and repulsive interactions in the shape of isosurfaces the reduced density gradient coloured by a scale of strength. Favourable and unfavourable interactions can be differentiated by the sign of second density Hessian eigenvalue (λ2) times the density (ρ) that is (sign(λ2)ρ). Attractive and repulsive interactions are identified as regions where λ2<0 and λ2>0, respectively. Weak van der Waals interactions by λ2≈0. To visualise these regions, often a colour code based on sign(λ2)ρ is used: blue for strong attractive interactions (λ2<0), green for weak van der Waals interactions(λ≈0) and red for strong repulsive interactions (λ2>0).

2.7 References

1. E. Schrödinger, *Annalen der Physik*, 1926, 384, 361-376.

2. M. Born and R. Oppenheimer, *Annalen der Physik*, 1927, 389, 457-484.

3. D. Hartree, *Mathematical Proceedings of the Cambridge Philosophical Society*, 1928, 24, 89-110.

4. J. Slater, *Physical Review*, 1928, 32, 339-348.

5. J. Slater, *Physical Review*, 1930, 35, 210-211.

6. V. Fock, *Zeitschrift für Physik*, 1930, 61, 126-148.

7. L. Thomas, *Mathematical Proceedings of the Cambridge Philosophical Society*, 1927, 23, 542-548.

8. E. Fermi, *Rend. Accad. Naz. Lincei*, 1927, 6, 602-607.

9. P. Dirac, *Mathematical Proceedings of the Cambridge Philosophical Society*, 1930, 26, 376-385.

10. P. Hohenberg and W. Kohn, *Physical Review*, 1964, 136, B864-B871.

11. W. Kohn and L. Sham, *Physical Review*, 1965, 140, A1133-A1138.

12. S. Vosko, L. Wilk and M. Nusair, *Canadian Journal of Physics*, 1980, 58, 1200-1211.

13. J. Perdew and A. Zunger, *Physical Review B*, 1981, 23, 5048-5079.

14. L. Cole and J. Perdew, *Physical Review A*, 1982, 25, 1265-1271.

15. J. Perdew and Y. Wang, *Physical Review B*, 1992, 45, 13244-13249.

16. A. Becke, *Physical Review A*, 1988, 38, 3098-3100.

17. J. Perdew, J. Chevary, S. Vosko, K. Jackson, M. Pederson, D. Singh and C. Fiolhais, *Physical Review B*, 1992, 46, 6671-6687.

18. J. Perdew, K. Burke and M. Ernzerhof, *Physical Review Letters*, 1996, 77, 3865-3868.

19. J. Tao, J. Perdew, V. Staroverov and G. Scuseria, *Physical Review Letters*, 2003, 91.

20. C. Lee, W. Yang and R. Parr, *Physical Review B*, 1988, 37, 785-789.

21. A. Becke, *The Journal of Chemical Physics*, 1993, 98, 5648-5652.

22. Y. Zhao and D. Truhlar, *Theoretical Chemistry Accounts*, 2007, 120, 215-241.

23. B. Mennucci and R. Cammi, *Continuum solvation models in chemical physics*, John Wiley & Sons, Chichester, England, 2007.

24. A. Klamt and G. Schüürmann, *J. Chem. Soc., Perkin Trans. 2*, 1993, 799-805.

25. F. Weinhold, C. Landis and E. Glendening, *International Reviews in Physical Chemistry*, 2016, 35, 399-440.

26. R. F. W. Bader, *Accounts of Chemical Research*, 1985, 18, 9-15.

27. R. F. W. Bader, *Chemical Reviews*, 1991, 91, 893-928.

28. R. F. W. Bader, *Atoms in molecules*, Clarendon Press, Oxford [England], 2003.

Chapter-3 Design of Intramolecular Chiral Frustrated Lewis Pairs (FLPs)

Catalysts form an indispensable part of innumerable industrial processes. The majority of these catalysts are transition metals[1] that are quite precious and/or scarce. In recent years there has been emphasis on trying main group elements as an alternative[2,3] to make these processes economically and environmentally more sustainable. Literature survey done in Chapter 1 revealed that FLPs composed of main group elements present themselves as viable alternatives to conventional catalysts. Exploration of FLP chemistry by DFT techniques is a new and promising field. We therefore sought to employ DFT methods to design some new chiral intramolecular FLPs for hydrogenation of substrates like olefins, carbonyl compounds and imines. The core skeleton envisaged for these FLPs was modified borenium carbene based on camphor scaffold, since this gives access to chirally pure species from naturally abundant chemical feedstock.

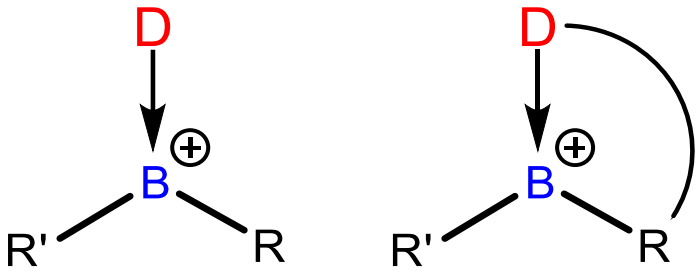

Figure 3.1 Donor stabilized (left) and a tethered donor stabilized borenium (right).

The proposed system consist of a $[B(R\text{^}D)R']^+$ core. where the R^D fragment represents a covalently bonded species with a secondary donor to assist in stabilising the borocation through formation of a coordinate bond. The backbone of the secondary ligand is inherently chiral and it is this part of the molecule that will provide the stereo-control necessary to produce efficient, asymmetric, intramolecular FLP catalysts. The

incorporation of both Lewis acid and Lewis base in a single molecule will enable catalyst loadings to be greatly reduced and hence improved performance relative to intermolecular FLPs.

Hence, the overall aim of this project was to design some new stereoselective intramolecular chiral catalysts. Myriad of acid and base linkers were tried so that in the near future our synthetic labs can utilize the results of these studies to select the best linkers for the actual synthesis of these compounds.

3.1 Selection of DFT Method

It is well known that selection of a proper functional for a given system from diverse variety of density functional approximations available is the basis for obtaining accurate results. Therefore, it was necessary to screen an appropriate functional before the start of the study. Initially two molecules **1** and **2** that were already synthesized[4] and characterized by experimental methods were selected as they had somewhat similar core structure as our envisaged FLPs. Several parameters for molecule **1** and **2** (Figure 3.2) were calculated using various computational techniques and were compared with the experimental values. All the calculations in thesis were done on Gaussian 09[5] software.

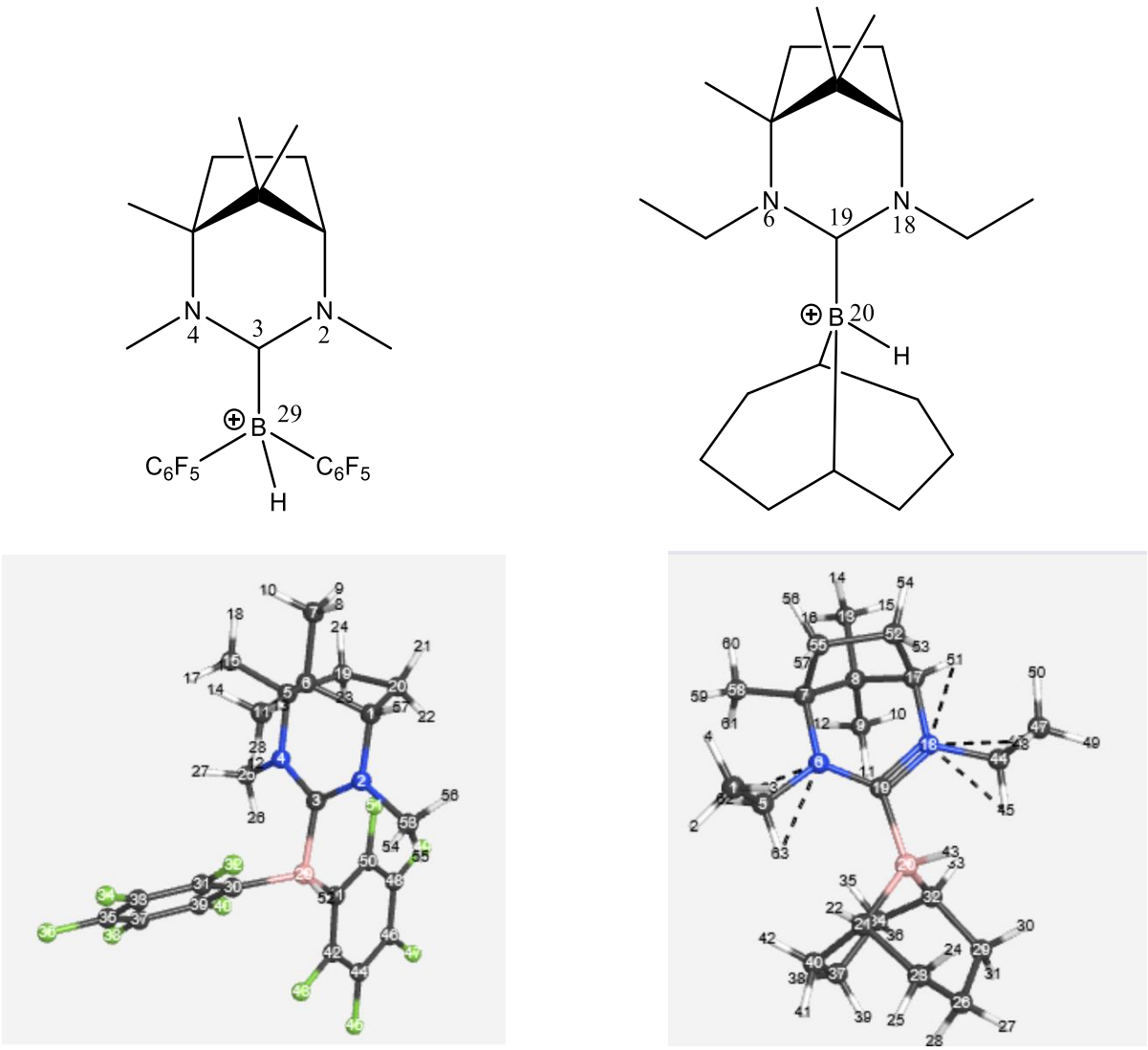

1 **2**

Figure 3.2 Pre-synthesized molecules 1 and 2 used for choosing DFT functional.

The aim of these calculations was to screen a best method which gives the results consistent with the experimental findings. Various conformations were also checked to ensure that we were dealing with a global energy minimum and not an intermediate. The values of the bond lengths obtained from various calculations were compared with the actual experimental values the summary of which is given in Table 3.1.

Method	**Bond Length /Å**	**Bond Length /Å**	**Bond Length /Å**	**r.m.s Error /Å**
Molecule 1	C3-B29	C3-N4	C3-N2	
Experimental	1.637	1.347	1.323	
HF/STO-3G	1.678	1.369	1.358	0.034
HF/3-21G	1.664	1.336	1.326	0.017
HF/6-31G(d)	1.684	1.336	1.323	0.028
B3LYP/STO-3G	1.655	1.351	1.341	0.015
B3LYP/3-21G	1.636	1.353	1.345	0.013
B3LYP/6-31G(d)	1.655	1.351	1.341	0.015
PBE/6-31G(d)	1.645	1.358	1.348	0.016
PBE0/6-31G(d)	1.643	1.344	1.334	0.007
B97D/6-31G(d)	1.656	1.355	1.344	0.017
wB97xD/6-31G(d)	1.646	1.344	1.333	0.008
M062X/6-31G(d)	1.647	1.343	1.332	0.008
Molecule 2	C19-B20	C19-N6	C19-N18	
Experimental	1.693	1.371	1.351	
HF/STO-3G	1.714	1.375	1.372	0.017
HF/3-21G	1.718	1.348	1.345	0.020
HF/6-31G(d)	1.736	1.345	1.339	0.030
B3LYP/STO-3G	1.66	1.404	1.4	0.039
B3LYP/3-21G	1.664	1.367	1.365	0.019
B3LYP/6-31G(d)	1.673	1.363	1.358	0.013
PBE/6-31G(d)	1.663	1.35	1.366	0.023
PBE0/6-31G(d)	1.664	1.354	1.341	0.020
B97D/6-31G(d)	1.671	1.358	1.364	0.017
wB97xD/6-31G(d)	1.666	1.352	1.32	0.026
M062X/6-31G(d)	1.672	1.362	1.349	0.013

Table 3.1 Comparison of bond lengths obtained by various calculations with the experimental values.

r.m.s. error values calculated for various functionals in Table 3 reveal that results for M06-2X/6-31G(d) level of theory (low values) are quite comparable with the values obtained by some well know functionals like B3LYP, PBE, PBE0, B97D and WB97xD. After reviewing the results in Table 3.1 and by observing its widespread use in investigation of reactions of similar FLPs (literature review done in Chapter 1), it was thought worthwhile to proceed for all the further calculations with M06-2X/6-31G(d) basis set as M06-2X functional is a high-nonlocality functional with double the amount of nonlocal exchange (2X), and it is parametrized particularly for main group thermochemistry, thermochemical kinetics, noncovalent interactions and excited states.

Two basic structures **3** and **4** were chosen for the present study (Figure 3.3). All the calculations were performed using M06-2X/6-31G(d) basis set.

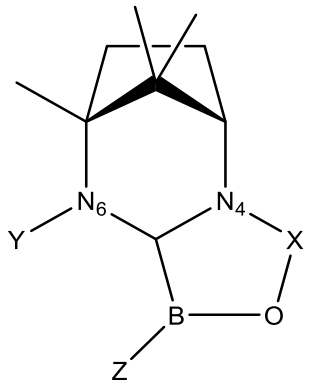

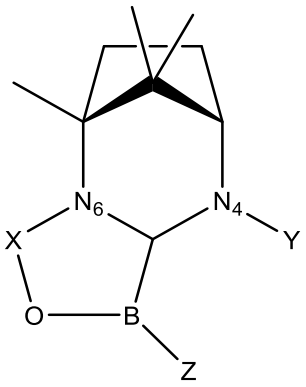

X= -CH_2, -CH_2CH_2, -$CH_2CH_2CH_2$, -C_6H_4, -$CH_2C_6H_4$

Y= -CH_2NH_2, -CH_2NMe_2, -CH_2PH_2, -CH_2PMe_2, -CH_2OH, -CH_2-2-Pyridine, -CH_2-2-Thiophene, -CH_2-2-Furan

Z= -CH_3, -C_6F_5

3 **4**

Figure 3.3 Basic structures chosen for the present study.

3.2 Designing FLP

The aim of the study was to design some chiral intramolecular FLPs which may be used in future as catalysts for enantioselective hydrogenation. The FLP has two major variable components, the Lewis acid component and the Lewis base component. Hence, the next part of the study was to screen linkers for Lewis acid component of FLP.

3.2.1 Linkers of Lewis Acid Component

In order to screen linkers for FLP, X in structure of **3** and **4** was varied using various groups while Y and Z were kept constant. Optimization was done for all the resultant structures and the comparative results are summarized in Table 3.2

Compound	Energy /Hartrees	Compound	Energy /Hartrees	Relative Stability (E_3-E_4) /kJmol^{-1}
3a (X=CH_2, Z= CH_3, Y=CH_3)	-679.6699118	**4a** (X=CH_2, Z= CH_3, Y=CH_3)	-679.6725362	7
3b (X=CH_2, Z= C_6H_5, Y=CH_3)	-871.3325302	**4b** (X=CH_2, Z= C_6H_5, Y=CH_3)	-871.3342679	5
3c (X=CH_2, Z= C_6F_5, Y=CH_3)	-1367.324749	**4c** (X=CH_2, Z= C_6F_5, Y=CH_3)	-1367.32641	4
3d (X=CH_2CH_2, Z= CH_3, Y=CH_3)	-718.9609325	**4d** (X=CH_2CH_2, Z= CH_3, Y=CH_3)	-718.9613754	1
3e (X=CH_2CH_2, Z= C_6H_5, Y=CH_3)	-910.6273236	**4e** (X=CH_2CH_2, Z= C_6H_5, Y=CH_3)	-910.6279593	2
3f (X=CH_2CH_2, Z= C_6F_5, Y=CH_3)	-1406.620229	**4f** (X=CH_2CH_2, Z= C_6F_5, Y=CH_3)	-1406.620561	1
3g (X=$CH_2CH_2CH_2$, Z= CH_3, Y=CH_3)	-758.2587585	**4g** (X=$CH_2CH_2CH_2$, Z=CH_3, Y=CH_3)	-758.2574874	-3
3h (X=$CH_2CH_2CH_2$, Z= C_6H_5, Y=CH_3)	-949.9282256	**4h** (X=$CH_2CH_2CH_2$, Z= C_6H_5, Y=CH_3)	-949.9269147	-3
3i (X=$CH_2CH_2CH_2$, Z= C_6F_5, Y=CH_3)	-1445.916663	**4i** (X=$CH_2CH_2CH_2$, Z= C_6F_5, Y=CH_3)	-1445.919103	6
3j (X=C_6H_4, Z= CH_3, Y=CH_3)	-871.3369152	**4j** (X=$C_6H_4CH_2$, Z=CH_3, Y=CH_3)	-871.3245743	-32
3k (X=C_6H_4, Z= C_6H_5, Y=CH_3)	-1063.000943	**4k** (X=C_6H_4, Z= C_6H_5, Y=CH_3)	-1062.988475	-33
3l (X=C_6H_4, Z= C_6F_5, Y=CH_3)	-1558.995229	**4l** (X=C_6H_4, Z= C_6F_5, Y=CH_3)	-1558.983101	-32
3m (X= $CH_2C_6H_4O$, Z= CH_3, Y=CH_3)	-910.6333576	**4m** (X=$CH_2C_6H_4O$, Z=CH_3, Y=CH_3)	-910.6334377	0.2
3n (X= $CH_2C_6H_4O$, Z= C_6H_5, Y=CH_3)	-1102.302849	**4n** (X= $CH_2C_6H_4O$, Z= C_6H_5, Y=CH_3)	-1102.303217	1
3o (X= $CH_2C_6H_4O$, Z= C_6F_5, Y=CH_3)	-1598.294979	**4o** (X= $CH_2C_6H_4O$, Z= C_6F_5, Y=CH_3)	-1598.294906	-0.2
3p (X= $C_6H_4CH_2O$, Z= CH_3, Y=CH_3)	-910.6309356	**4p** (X=$C_6H_4CH_2O$, Z=CH_3, Y=CH_3)	-910.6256838	-14

Table 3.2 Comparative electronic energies of **3(a-p)** and **4(a-p)** after optimization using M06-2X/6-31G(d) level of theory.

The data in Table 2 was analysed to find stable ligands of **3** and **4**. It was found that **4a**-**4f**, **3g**, **3h**, **4i**, **3j**-**3l** and **4m**-**4p** are more stable than **3a**-**3f**, **4g**, **4h**, **3i**, **4j**-**4l** and **3m**-**3p**. Out of **4m** and **4p**, **4m** linker was 20 kJ mol^{-1} more stable than **4p**. Hence all the further studies were carried out using these stable linkers only.

After screening the stable linkers, their HIA (Hydrogen Ion Affinity) and FIA (Fluoride Ion Affinity) was studied to know the relative strength of these Lewis acids. HIA and FIA have been used as powerful tool to estimate Lewis acidity.

$$LA + H^- \rightarrow LAH^-(HIA: -\Delta H) \qquad 3.1$$

$$LA + F^- \rightarrow LAF^-(FIA: -\Delta H) \qquad 3.2$$

All these calculations were done on BP86/SVP level as the values calculated for some small molecules as a test on BP86/SVP level were much closer to the reported values as compared to B3LYP/6-31G(d) and M062x/6-31G(d) values (Table 3.3), due to cancellation of errors, as originally noted in reference 6.

Compound	**HIA /kJ mol^{-1} B3LYP/6-31G(d)**	**HIA /kJ mol^{-1} M062X/6-31G(d)**	**HIA /kJ mol^{-1} BP86/SVP**	**HIA /kJ mol^{-1} Reported**
BF3	348	373	303	297
BCl3	468	504	392	395
BBr3	472	513	436	440

Table 3.3 A comparison of HIA values of some known compounds (Reference 6) carried out on B3LYP/6-31G(d), M062X/6-31G(d) and BP86/SVP levels.

The calculations were carried out with the stable linkers of Table 3.2 and the results are depicted in Table 3.4. BSSE (Basis set superposition error) was also calculated in each case.

$$\Delta E_{int}^{CP}(r_{AB}) = E_{AB}^{AB}(r_{AB}) - E_{A}^{AB}(r_{AB}) - E_{B}^{AB}(r_{AB}) \qquad 3.3$$

Compound	**HIA /kJmol^{-1}**	**FIA /kJmol^{-1}**
4a (X=CH_2, Y= CH_3, Z=CH_3)	652	647
4b (X=CH_2, Y= C_6H_5, Z=CH_3)	662	653
4c (X=CH_2, Y= C_6F_5, Z=CH_3)	704	687
4d (X=CH_2CH_2, Y= CH_3, Z=CH_3)	641	635
4e (X=CH_2CH_2, Y= C_6H_5, Z=CH_3)	638	630
4f (X=CH_2CH_2, Y= C_6F_5, Z=CH_3)	685	662
3g (X=$CH_2CH_2CH_2$, Y= CH_3, Z=CH_3)	619	608
3h (X=$CH_2CH_2CH_2$, Y= C_6H_5, Z=CH_3)	612	592
4i (X=$CH_2CH_2CH_2$, Y= C_6F_5, Z=CH_3)	629	603
3j (X=C_6H_4, Y= CH_3, Z=CH_3)	666	656
3k (X=C_6H_4, Y= C_6H_5, Z=CH_3)	674	664
3l (X=C_6H_4, Y= C_6F_5, Z=CH_3)	719	698
4m (X=$CH_2C_6H_4O$, Y=CH_3, Z=CH_3)	633	625
4n (X= $CH_2C_6H_4O$, Y= C_6H_5, Z=CH_3)	625	611
4o (X= $CH_2C_6H_4O$, Y= C_6F_5, Z=CH_3)	678	656

Table 3.4 HIA and FIA values for the stable linkers carried out at BP86/SVP level.

A comparison of the values of Table 3.3 and Table 3.4 clearly indicate that the molecules of our study had much higher values and hence were more strong Lewis acids as compared to the reference ones. The reason for this may be attributed to the fact that our molecules of interest are borenium cations rather than neutral boron

molecules and hence have formal positive charge. Apart from this an oxygen atom is directly attached with these cations which further intensifies the positive charge and in turn the Lewis acidity.

3.2.2 Linkers of Lewis Base Component

Once we knew the stable linkers and their corresponding Lewis acidity, the next phase was to attach various bases on N6 (in case of **3**)/N4 (in case of **4**) and check whether these adducts were frustrated pairs or not. For this study, the simple stable linkers 4a and 4c was chosen and Y was varied using various bases. In many cases it was possible to optimize more than one conformer. NBO read command was used to calculate Wiberg bond indexes (WBI) that were used to calculate the bond orders. Values of their energies and bond orders between Boron and Nitrogen of Lewis pairs are depicted in Table 3.5. A comparison of the values of the bond orders indicates that compounds **4(vii)**-**4a(x)** seem to be normal (bond order 0.5 or more) pairs while the rest may prove to be frustrated (bond order close to zero).

Compound	**Energy /Hartrees**	**Bond order (B-N)**
4a X=CH_2, Y=CH_3, Z=CH_3	-679.6725362	0.0
4a(i) X=CH_2, Y=CH_2NH_2, Z=CH_3 (conformer 1)	-734.998968356	.0012
(conformer 2)	-734.999450165	.0012
(conformer 3)	-734.999450199	.0012

4a(ii) X=CH_2, Y=CH_2NMe_2, Z=CH_3 (conformer 1)	-813.578315032	.0015
(conformer 2)	-813.577712221	.0014
4a(iii) X=CH_2, Y=CH_2PH_2, Z=CH_3 (conformer 1)	-1021.57052919	.0016
(conformer 2)	-1021.5714796	.0005
(conformer 3)	-1021.57153839	.0009
4a(iv) X=CH_2, Y=CH_2PMe_2, Z=CH_3 (conformer 1)	-1100.17632362	.0023
(conformer2)	-1100.17721826	.0006
4a(v) X=CH_2, Y=CH_2OH, Z=CH_3 (conformer 1)	-754.860144946	.0027
(conformer 2)	-754.860551713	.0027
(conformer 3)	-754.860547062	.0020
4a(vi) X=CH_2, Y=$CH_2CH_2NH_2$, Z=CH_3 (conformer 1)	-774.315220115	.5795
(conformer 2)	-774.315220323	.5795
(conformer 3)	-774.289734643	.5794
4a(vii) X=CH_2, Y=$CH_2CH_2NMe_2$, Z=CH_3	-852.901692603	.5299
4a(viii) X=CH_2, Y=$CH_2CH_2PMe_2$, Z=CH_3	-1139.484193	.8882
4a(ix) X=CH_2, Y=CH_2CH_2OH, Z=CH_3	-794.14525431	.4386
4a(x) X=CH_2, Y=$CH_2CH_2CH_2NH_2$, Z=CH_3 (conformer 1)	-813.579195017	.0001
(conformer 2)	-813.62428454	.5904
(conformer 3)	-813.57977313	.0001
(conformer 4)	-813.581300422	.0003

4a(xi) X=CH_2, Y=C_6H_4-o-NH_2, Z=CH_3 (conformer 1)	-926.6777252	.0002
(conformer 2)	-926.6776774	.0225
(conformer 3)	-926.6777256	.0002
4a(xii) X=CH_2, Y=C_6H_4-m-NH_2, Z=CH_3 (conformer 1)	-926.675723856	.0002
(conformer 2)	-926.676642044	.0001
(conformer 3)	-926.675723801	.0002
(conformer 4)	-926.676429213	.0002
4a(xiii) X=CH_2, Y=C_6H_4-p-NH_2, Z=CH_3 (conformer 1)	-926.677707402	.0004
(conformer 2)	-926.677897926	.0003
(conformer 3)	-926.677707483	.0004
(conformer 4)	-926.677707348	.0004
4a(xiv) X=CH_2Y=CH_2-2pyridine, Z=CH_3	-926.679811408	0.0185
4a(xv) X=CH_2, Y=CH_2-2furan, Z=CH_3	-908.425200033	0.0027
4a(xvi) X=CH_2, Y=CH_2-2thiophene, Z=CH_3	-1231.39215405	0.0019
4a(xvii) X=CH_2, Y=CH_2NH_2, Z=C_6F_5	-1422.65885557	.0010
4a(xviii) X=CH_2, Y=CH_2NMe_2, Z=C_6F_5	-1501.23356396	.0107
4a(xix) X=CH_2, Y=CH_2PH_2, Z=C_6F_5	-1709.22467546	0.002
4a(xx) X=CH_2, Y=CH_2PMe_2, Z=C_6F_5	-1787.83189368	.0002
4a(xxi) X=CH_2Y=CH_2-2pyridine, Z=C_6F_5	-1614.36499593	0.5647

Table 3.5 Electronic energy and the bond order values for some selected LA/LB pairs using M06-2X/6-31G(d) level of theory.

3.3 Hydrogen Activation by Novel FLPs

Once FLPs were designed next part of the study was to evaluate whether the above screened FLPs were able to split hydrogen molecule or not; and if they were able to split, then what are the energetics of this reaction? To begin with two extreme cases were selected: (1) the molecule in which the hydrogen molecule was far away from FLP (Reactant) and (2) other in which the hydrogen molecule was actually split by FLP and as a result one of the hydrogens goes to base part and the other to the acid part (Product).

Initially the reactant was optimized using M06-2X/6-31G(d) level of theory. Figure 3.4 shows the optimized structure of reactant (using most stable conformer of **4a(i)** FLP).

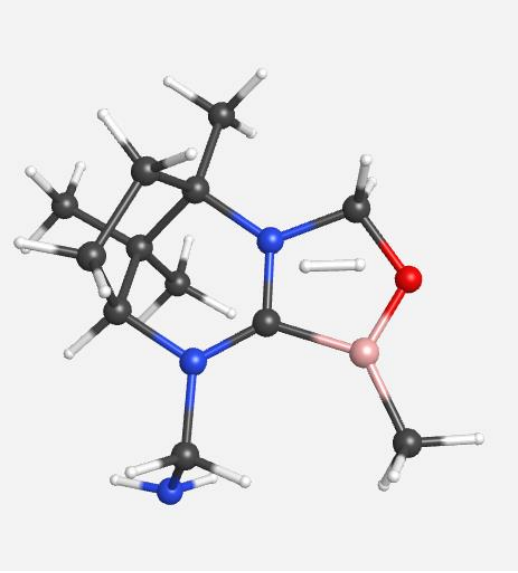

Figure 3.4 Optimized structure of the reactant (using **4a(i)** FLP) at M06-2X/6-31G(d) level of theory.

Afterwards, relaxed potential energy scan was done by running a scan of FLP-B-H(28)….H(35)-N-FLP distance (starting from distance 3.57 Å and then reducing it gradually) to understand the movement of hydrogen from reactant to the product. Figure 3.5 depicts the scan plot of the same.

Next, a transition state search (TS) was tried from various potential point on the scan plot. Transition state so obtained (Figure 3.6) had only one imaginary frequency (1057.71i cm^{-1}) that corresponded to a normal mode for simultaneous movement of hydrogens.

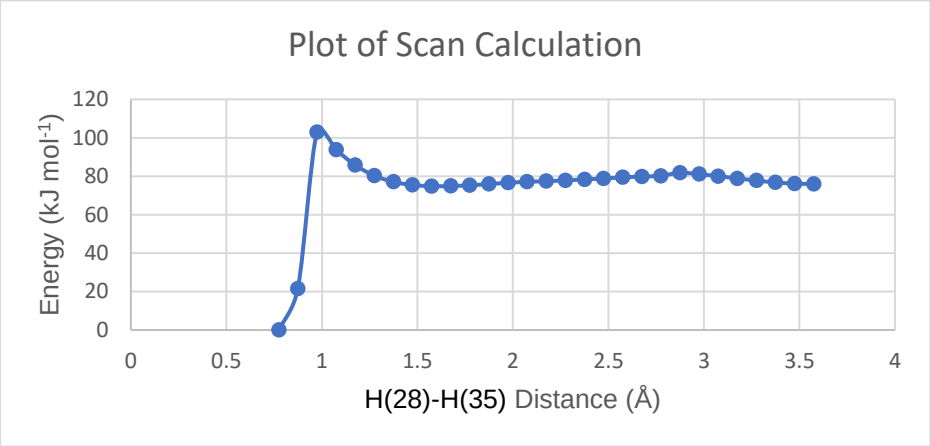

Figure 3.5 Scan plot for activation of hydrogen by FLP **4a(i)**.

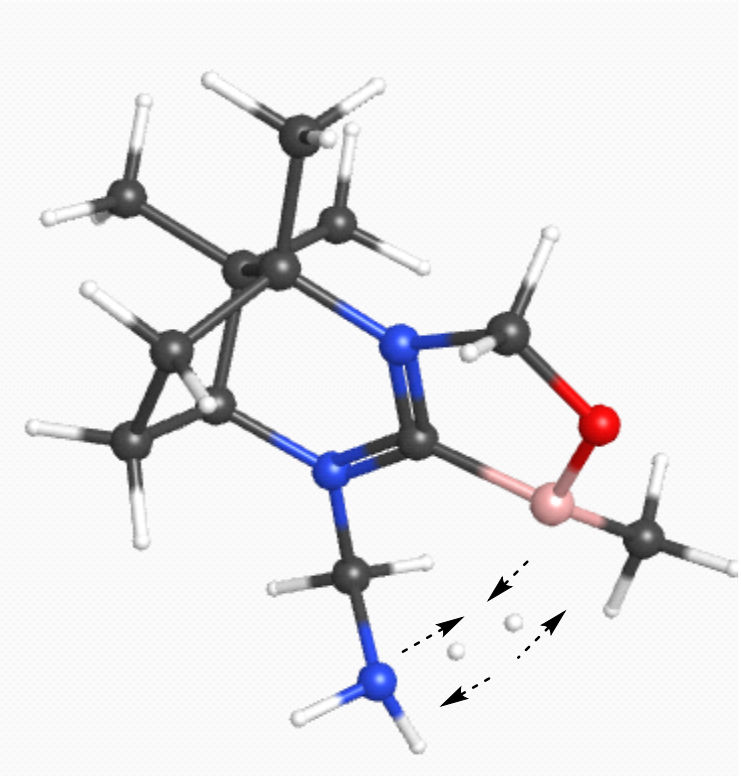

Figure 3.6 Transition state for activation of hydrogen by FLP **4a(i)**.

Intrinsic reaction co-ordinate (IRC) calculation was done to ensure that the transition state connected with the same reactant and product on either side. Figure 3.7 represents the IRC plot for activation of hydrogen by FLP **4a(i)**. Reaction co-ordinate diagram for the complete reaction in gaseous phase is given in Figure 3.8 (study of this reaction has been done in solvent phase as well).

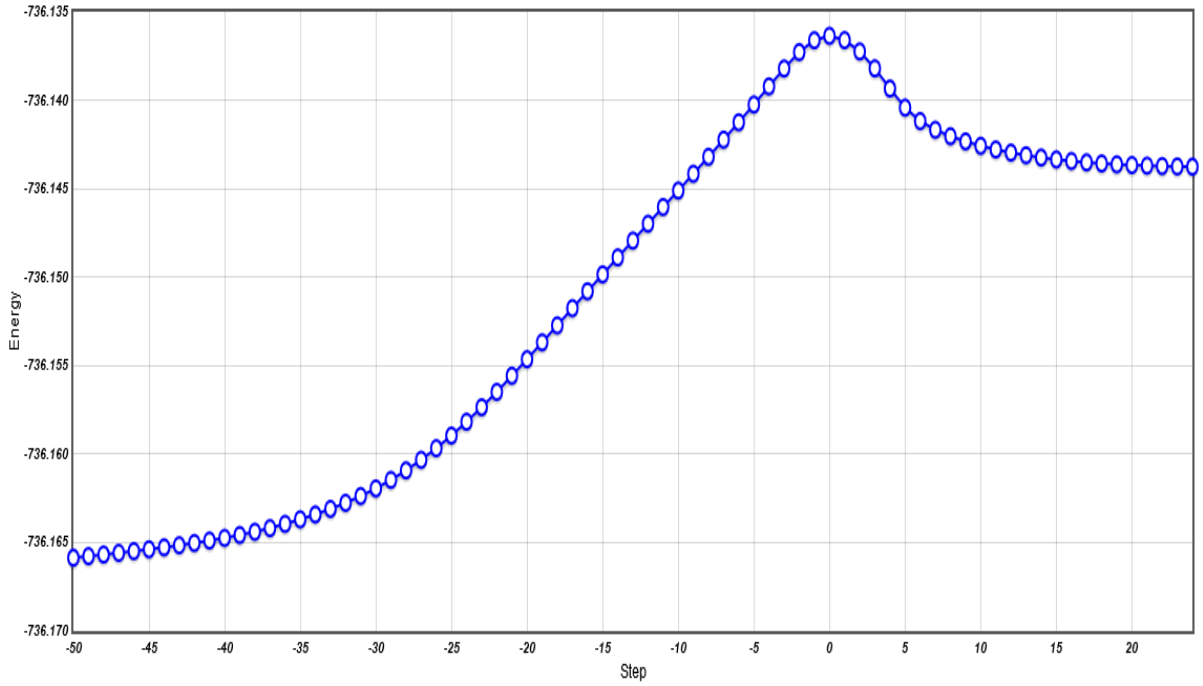

Figure 3.7 IRC plot for activation of hydrogen by FLP by **4a(i)**.

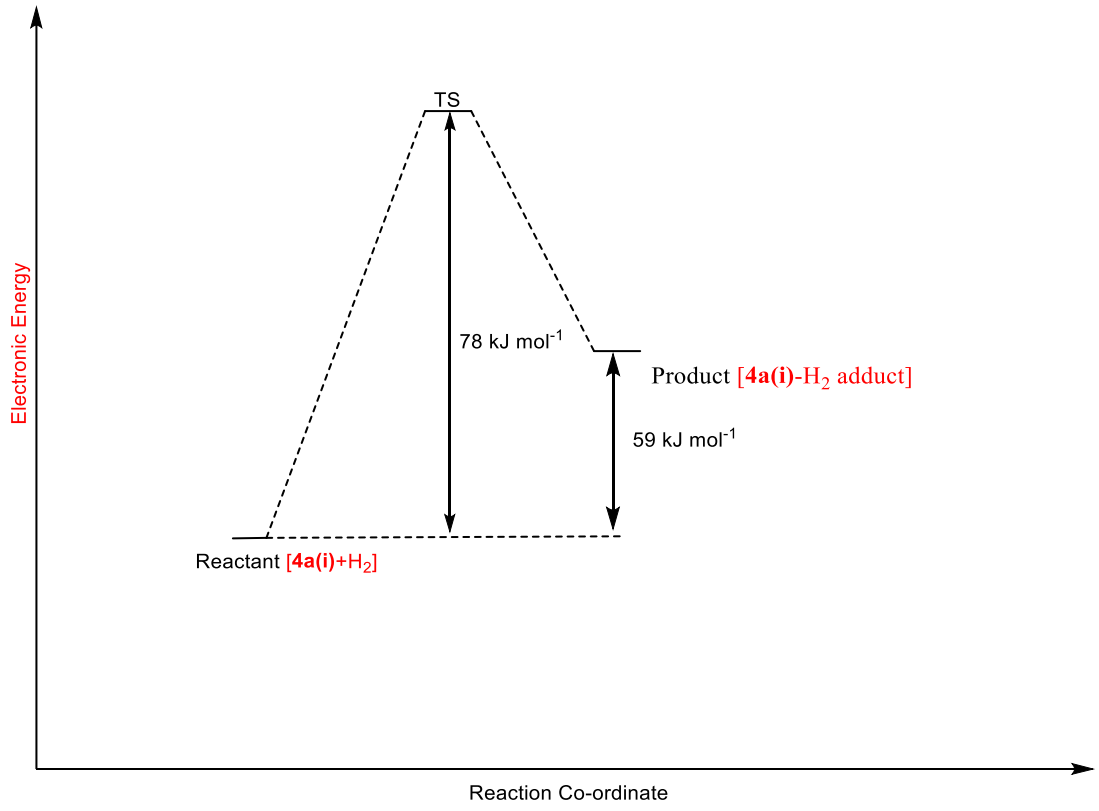

Figure 3.8 Reaction co-ordinate diagram for activation of hydrogen by FLP **4a(i)**.

Study of selected bond lengths (bond orders) that actively take part in transition state (Figure 3.9) indicate that the activation of hydrogen by FLP **4a(i)** is concerted and synchronous. Energetics of the whole conversion in gas phase and solvent (toluene) is shown in Table 3.6.

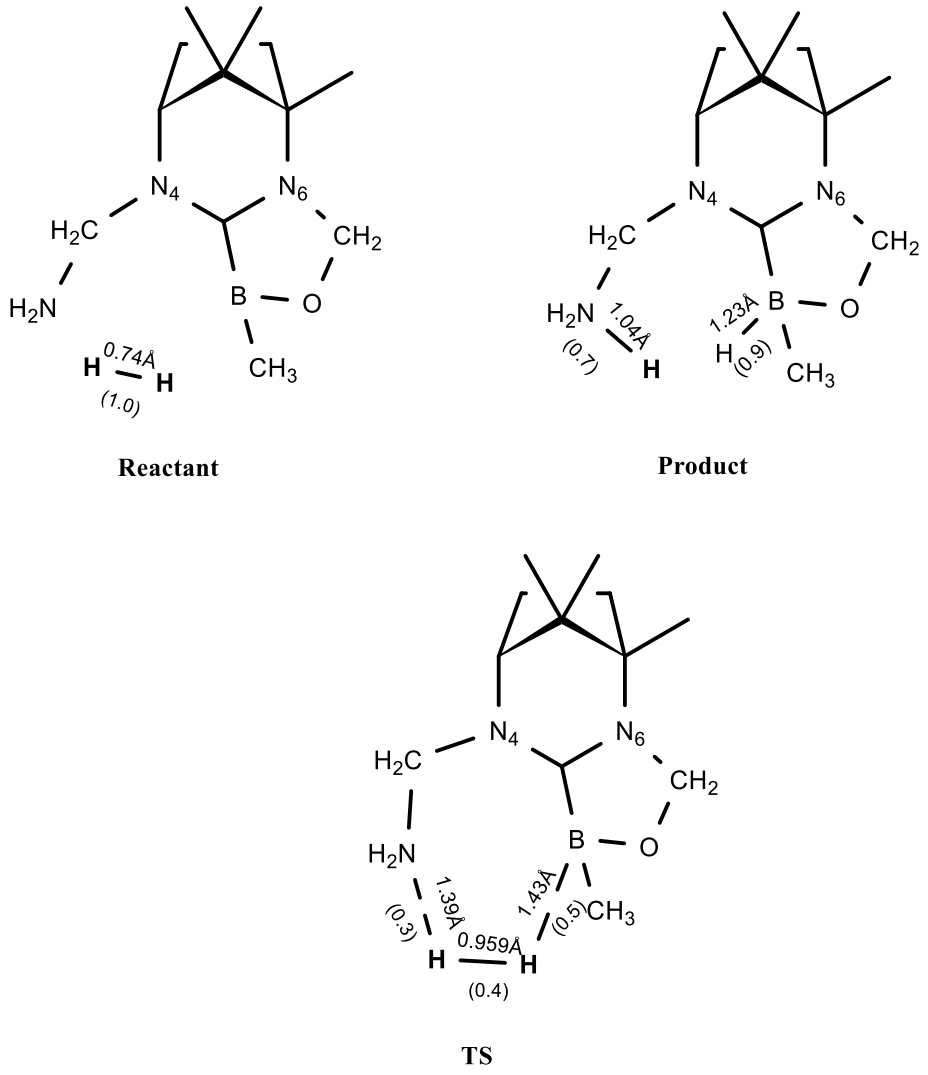

Figure 3.9 Comparison of bond lengths (bond orders) that actively take part in the activation of hydrogen by FLP **4a(i)**.

Substrate	**Electronic *E* /Hartrees**	***Δ‡E* /kJ mol^{-1}**	***Δ‡G* /kJ mol^{-1}**	***ΔE* /kJ mol^{-1}**	***ΔG* /kJ mol^{-1}**
Gas Phase					
Reactant [**4a(i)**+H_2]	-736.1661037				
Product [**4a(i)**-H_2] adduct	-736.1437789			59	84
TS	-736.1363229	78	91		
Toluene					
Reactant [**4a(i)**+H_2]	-736.2202167				
Product [**4a(i)**-H_2] adduct	-736.210547			25	51
TS	-736.1944921	68	81		

Table 3.6 Energetics for activation of H2 by **4a(i)** in gaseous and solvent (toluene) phase.

After the completion of the complete mechanism for activation of hydrogen by FLP **4a(i)**, the same procedure was repeated for some selected FLPs from Table 3.5. Table 3.7 shows the energetics for activation of hydrogen by FLPs in gas phase while table 3.8 shows it in solvent (toluene).

FLP	$\Delta^{\ddagger}E$ /kJ mol^{-1}	$\Delta^{\ddagger}G$ /kJ mol^{-1}	ΔE /kJ mol^{-1}	ΔG /kJ mol^{-1}
4a(i) X=CH_2, Y=CH_2NH_2, Z=CH_3	78	91	59	84
4a(ii) X=CH_2, Y=CH_2NMe_2, Z=CH_3	69	80	56	51
4a(iii) X=CH_2, Y=CH_2PH_2, Z=CH_3	175	184	151	169
4a(iv) X=CH_2, Y=CH_2PMe_2, Z=CH_3	106	116	82	102
4a(xi) X=CH_2, Y=C_6H_4-o-NH_2, Z=CH_3	48	59	9	29
4a(xiii) X=CH_2, Y=C_6H_4-p-NH_2, Z=CH_3	234	243	72	86
4a(xiv) X=CH_2Y=CH_2-2pyridine, Z=CH_3	124	128	68	84
4a(xv) X=CH_2, Y=CH_2-2furan, Z=CH_3	-	-	-	-
4a(xvi) X=CH_2, Y=CH_2-2thiophene, Z=CH_3	-	-	-	-
4a(xvii) X=CH_2, Y=CH_2NH_2, Z=C_6F_5	56	68	4	33
4a(xviii) X=CH_2, Y=CH_2NMe_2, Z=C_6F_5	71	86	8	37
4a(xix) X=CH_2, Y=CH_2PH_2, Z=C_6F_5	110	113	84	100
4a(xx) X=CH_2, Y=CH_2PMe_2, Z=C_6F_5	47	38	-18	-15
4a(xxi) X=CH_2Y=CH_2-2pyridine, Z=C_6F_5	141	143	80	102

Table 3.7 Energetics for activation of hydrogen by FLPs in gas phase.

FLP	$\Delta^{\ddagger}E$ /kJ mol^{-1}	$\Delta^{\ddagger}G$ /kJ mol^{-1}	ΔE /kJ mol^{-1}	ΔG /kJ mol^{-1}
4a(i) X=CH_2, Y=CH_2NH_2, Z=CH_3	68	81	25	51
4a(ii) X=CH_2, Y=CH_2NMe_2, Z=CH_3	63	75	0.01	27
4a(iii) X=CH_2, Y=CH_2PH_2, Z=CH_3	155	164	113	131
4a(iv) X=CH_2, Y=CH_2PMe_2, Z=CH_3	99	108	51	72
4a(xi) X=CH_2, Y=C_6H_4-*o*-PMe_2, Z=CH_3	46	57	-10	10
4a(xiii) X=CH_2, Y=C_6H_4-*p*-PMe_2, Z=CH_3	235	244	39	54
4a(xiv) X=CH_2, Y=CH_2-2pyridine, Z=CH_3	121	125	40	56
4a(xv) X=CH_2, Y=CH_2-2furan, Z=CH_3	-	-	-	-
4a(xvi)X=CH_2, Y=CH_2-2thiophene, Z=CH_3	-	-	-	-

Table 3.8 Energetics for activation of hydrogen by FLPs in solvent (toluene).

Some interesting facts are observed from the study of the table. In general, it is observed that the activation barriers are low when the base is tertiary amine or phosphine rather than primary amine or phosphine. For example, **4a(ii)** has a lower activation barrier than **4a(i)**, **4a(iv)** has less than **4a(iii)**, **4a(xx)** is less than **4a(xix)**. A plausible reason for this observation may be the fact that alkyl amines and alkyl phosphines are more basic than primary amines and phosphines because the alkyl group donates electrons to the electronegative atom by induction and increases electron density around it which makes it even more basic. As the resultant FLP is

stronger, it can split or activate hydrogen more effectively, thus reducing the activation barrier. But contrary to this trend activation barrier for **4a(xviii)** is not less than **4a(xvii)**.

It is noticed that the activation barrier is also reduced when Z is C_6F_5 instead of CH_3 which becomes obvious by the fact that barrier for **4a(xvii)** is less than **4a(i)**, **4a(xix)** is less than **4a(iii)** and **4a(xx)** is less than **4a(iv)**. The reason for this trend also seems obvious as C_6F_5 is more electronegative, it makes the boron even more acidic and the resultant FLP stronger as a result of which activation barrier is reduced. In this case also the barrier for **4a(xviii)** is not less than **4a(ii)**. Three heterocycles, pyridine, furan and thiophene, were chosen for this study as they are quite different in structure and basicity from the primary and tertiary amines. The purpose was to check if they can split hydrogen at all and if so, what are the energetics. It was seen that furan, and thiophene are not able to split hydrogen. It is expected as they are very weak bases which owe their basicity to the lone pair present in sp^2 hybridized orbital which is nearer to the nucleus than the lone pair in sp^3 hybridized orbitals and hence is very difficult to protonate. In the case of pyridine, it was able to split hydrogen, but the energy barrier was quite high and in addition it does not follow the trend as the barrier for **4a(xxi)** is more than **4a(xiv)**. The reason for this trend may be attributed to the fact that although pyridine is more basic than furan and thiophene but is less basic than primary or tertiary amines as neither its lone pair is in sp^3 hybridized orbital nor it has alkyl groups to increase its basicity. Hence, although pyridine splits hydrogen, the barrier is quite high.

Values from the Table 3.6 also reveal that compound **4a(xx)** needs minimum activation energy while compounds **4a(xv)** and **4a(xvi)** are unable to split hydrogen molecule. It may also be noted that the cases in which energy barrier is low (less activation energy is needed), their *ΔE/ΔG* values are also less. As activation energy and *ΔE* and *ΔG* are less in case of **4a(xx)**, it will activate the hydrogen very effectively but at the same time resultant activated FLP might not lose the hydrogens so easily in the next step of hydrogenation and hence may not ultimately prove to be a good hydrogenation catalyst. Electron donating groups (alkyl groups) in FLP reduce the activation barrier and make the reaction more favourable while weak bases (pyridine) increase the barriers (some like furan and thiophene are not able to split hydrogen at all) and are thus not favourable. It has also been observed that the solvent also plays a significant role as it reduces activation barrier and *ΔE/ΔG* values (except in case of **4a(xiii)**). It is observed that the difference in the activation energies of non-solvated and solvated molecules ranges between 1 kJ mol^{-1} - 20 kJ mol^{-1}. The reason for this difference may be attributed to the ability of solvent molecule to stabilize the transition state thus decreasing the activation barrier.

3.4 Screening of New scaffolds for FLP chemistry

Two new scaffolds (Figure 3.10) of potential Lewis acids (**5** and **6**) were studied computationally as the synthesis of these linkers was also in process. It was thought worthwhile to study the energetics of these systems in detail as it may help in predicting if it is possible to employ these Lewis acids in FLP-based catalysis or not.

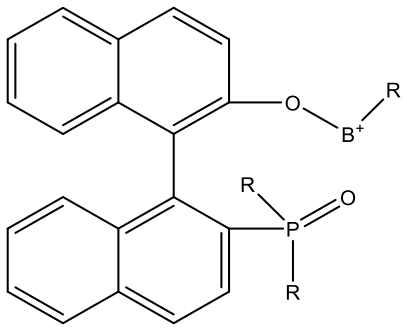

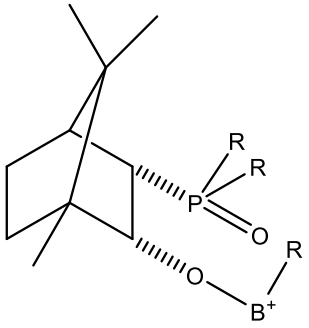

5 **6**

5a (R=H) **6a** (R=H)

5b (R=CH_3) **6b** (R=CH_3)

5c (R=Ph) **6c** (R=Ph)

Figure 3.10 New scaffolds **5** and **6**.

All calculations were done using M062X/6-31G(d) level of theory. Various groups ranging from small R=H to bulky R=Ph were tried during the calculations of these scaffolds to understand the impact of steric bulk on acidity. Bond orders of some selected bonds in **5** and **6** are depicted in Figure 3.11.

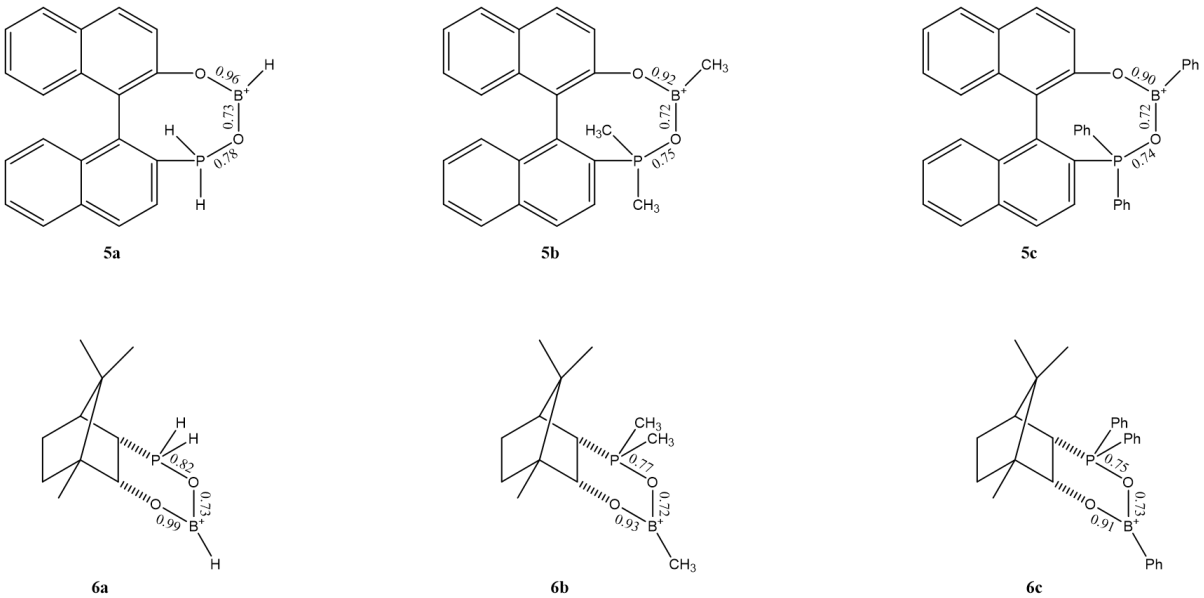

Figure 3.11 Bond orders of some selected bonds in **5** and **6**.

A glance at the values of the bond orders reveal that the P-O bond is a little less than single bond rather than expected double bond while PO-B is co-ordinate probably getting electron donation from lone pair of phosphorus.

HOMO, LUMO and LUMO+1 plot for **5a** and **6a** are shown in Figure 3.12. A close look at these plots reveals that in the case of the HOMO the electron density is centred around one of the aromatic rings in case of **5a** and the carbon framework in case of 6a but not around boron or phosphorus. In the case of LUMO, in addition to the probability around aromatic ring in **5a** it is found to be concentrated on phosphorous and a little on the oxygen connecting boron and phosphorus. LUMO+1 of **5a** is like HOMO while in the case of **6a** LUMO is centred around boron, phosphorus and oxygen connecting both rather than the carbon framework. Rest of the linkers (**5b**,**5c**,**6b** and **6c**) also follow the similar trend.

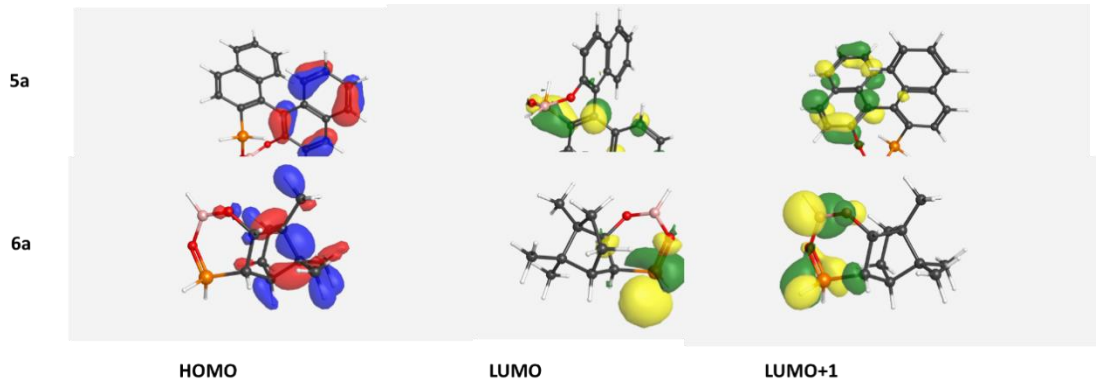

Figure 3.12 HOMO, LUMO and LUMO+1 plots for **5a** and **6a**.

HIA and FIA values were calculated at BP86/SVP level in the next step to confirm the Lewis acidity of these compounds, including counterpoise correction to remove BSSE. The results of the calculations done are compiled in Table 3.9. These results

have also been compared with the results of N-Heterocyclic Carbenes (NHC) linkers calculated previously.

Compound	**HIA /kJ mol^{-1}**	**FIA /kJ mol^{-1}**
5a (R=H)	692	694
5b (R=CH_3)	623	636
5c (R=Ph)	612	621
6a (R=H	695	707
6b (R=CH_3)	615	629
6c (R=Ph)	579	587
4a (X=CH_2, Y=CH_3, Z=CH_3)	652	647
4b (X=CH_2CH_2, Y=CH_3, Z=CH_3)	641	635
[a]BF_3	303.4	
[a]BCl_3	391.6	
[a]BBr_3	435.9	

Table 3.9 HIA and FIA values of various linkers for the comparison of their Lewis acidity done at BP86/SVP level of theory.

[a] Reference compounds from literature[6]

A glance at the table reveal that HIA and FIA values of the new LA are in the same range as some of our previously studied LA (NHCs). Data in the table indicates that both HIA and FIA values decrease when we make the R group bulky i.e. the value is

maximum when R=H and minimum when R=Ph which shows that the acidity decrease with increase in bulk. Trends are not too regular when we compare the values for compound **5** and **6** with each other. Acidity of molecule **5** is less than **6** if R=H but it is more than 6 if R=CH_3 or Ph.

3.5 Conclusions

In this chapter, initially screening of functionals was done. It was found that M06-2X is a functional of choice for this study. Following literature precedent, BP86/SVP functional was used to calculate HIA and FIA values. These methods were used to screen possible linkers for Lewis acid as well as Lewis base part for FLP. This allowed us to separate FLPs from normal Lewis pairs. This process was applied to camphor-based carbene-borenium systems with a range of linker groups, and also to binaphthol and camphor-based phosphine-oxide/borenium molecules. The former show encouraging FLP-like behaviour, as judged by bond order, with suitably chosen linkers, but the latter form normal Lewis pairs.

Activation of hydrogen by FLPs was studied in the next phase. It was found that bases like tertiary amines/phosphines may prove to be better catalysts than primary amines/phosphines due to low activation barriers while weak bases like pyrimidine might not be substrates of choice because of their high activation barriers (thiophene and furan bases are unable to split hydrogen). It was observed that solvents play active part in activation by significantly reducing the activation barriers. Results show that the activation of hydrogen by FLPs is concerted and synchronous process.

3.6 References

1. J. Hagen, *Industrial Catalysis: A Practical Approach*, John Wiley & Sons, 2015.

2. L. Wilkins and R. Melen, *Coordination Chemistry Reviews*, 2016, 324, 123-139.

3. S. Harder, *Early Main Group Metal Catalysis*, John Wiley & Sons, Incorporated, Newark, 2020.

4. P. D. Newman, Personal Communication.

5. Gaussian 09, Revision C.01, M. J. Frisch, G. W. Trucks, H. B. Schlegel, G. E. Scuseria, M. A. Robb, J. R. Cheeseman, G. Scalmani, V. Barone, B. Mennucci, G. A. Petersson, H. Nakatsuji, M. Caricato, X. Li, H. P. Hratchian, A. F. Izmaylov, J. Bloino, G. Zheng, J. L. Sonnenberg, M. Hada, M. Ehara, K. Toyota, R. Fukuda, J. Hasegawa, M. Ishida, T. Nakajima, Y. Honda, O. Kitao, H. Nakai, T. Vreven, J. A. Montgomery, Jr., J. E. Peralta, F. Ogliaro, M. Bearpark, J. J. Heyd, E. Brothers, K. N. Kudin, V. N. Staroverov, T. Keith, R. Kobayashi, J. Normand, K. Raghavachari, A. Rendell, J. C. Burant, S. S. Iyengar, J. Tomasi, M. Cossi, N. Rega, J. M. Millam, M. Klene, J. E. Knox, J. B. Cross, V. Bakken, C. Adamo, J. Jaramillo, R. Gomperts, R. E. Stratmann, O. Yazyev, A. J. Austin, R. Cammi, C. Pomelli, J. W. Ochterski, R. L. Martin, K. Morokuma, V. G. Zakrzewski, G. A. Voth, P. Salvador, J. J. Dannenberg, S. Dapprich, A. D. Daniels, O. Farkas, J. B. Foresman, J. V. Ortiz, J. Cioslowski, and D. J. Fox, Gaussian, Inc., Wallingford CT, 2010.

6. H. Böhrer, N. Trapp, D. Himmel, M. Schleep and I. Krossing, *Dalton Trans.*, 2015, 44, 7489-7499.

4 Hydrogenation of Achiral Substrates

In Chapter-3, activation of hydrogen by FLPs was discussed. This chapter reports attempts to study the hydrogenation of some small achiral molecules by hydrogen molecules activated by these FLPs.

4.1 Hydrogenation of olefins (Ethene) by FLP/H_2 system

To understand the mechanism of hydrogenation by FLP/H_2 system, **4a(i)** FLP (the base is $–NH_2$ in this FLP) was selected as catalyst for this study (as it was simplest in structure, had FLP character and was also able to activate hydrogen effectively) and ethene (the simplest olefin) as substrate. To begin with FLP **4a(i)**/H_2-ethene system was optimized with the help of M062X/6-31G(d) level of theory in gas phase. The optimized structure thus obtained for the combined system is shown in Figure 4.1.

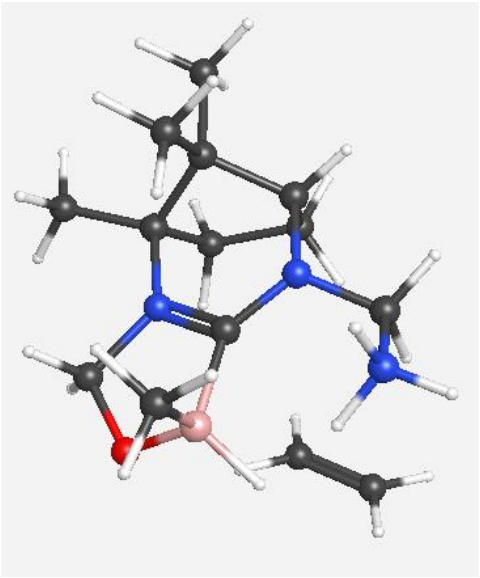

Figure 4.1 Optimized structure of **4a(i)/H_2-ethene** system.

Afterwards, various relaxed potential energy scans were done. In the first set of scans, hydrogen attached with boron was gradually brought closer to ethene (B-H……C43/ B-H……C44) while in the second set hydrogen attached with nitrogen was slowly brought closer to ethene (N-H……C43/ N-H……C44), and in both cases the energy and structural changes along the path were monitored. In the next scan hydrogen attached to boron and the hydrogen attached to nitrogen were simultaneously brought closer to the ethene (B-H…...C43 and N-H…...C44). Last category of the scans was the reverse one in which hydrogens attached with the alkane were slowly brought closer to boron and nitrogen respectively.

The xyz coordinates were chosen from various plausible points (most of the time they were the points at which hydrogen detached from the FLP and started moving towards the olefin) on the scan and calculations were done with each of them to locate the transition state. In this particular case QST3 calculation was also done to confirm the mechanism. A frequency calculation was also done along with optimization. Only one imaginary frequency was obtained (1303i cm^{-1}) that corresponds to a normal mode for simultaneous movement of hydrogens. Figure 4.2 shows the optimized structure of the transition state involved. To ascertain if this transition state connected the reactants with the products the IRC calculation was carried out which has shown that hydrogenation actually occurs via this transition state only. Figure 4.3 shows the energetics of the IRC calculation. Start and end points of the IRC were optimized to get the actual structure of reactant and product. Figure 4.4 depicts the optimized structure of actual reactant from IRC.

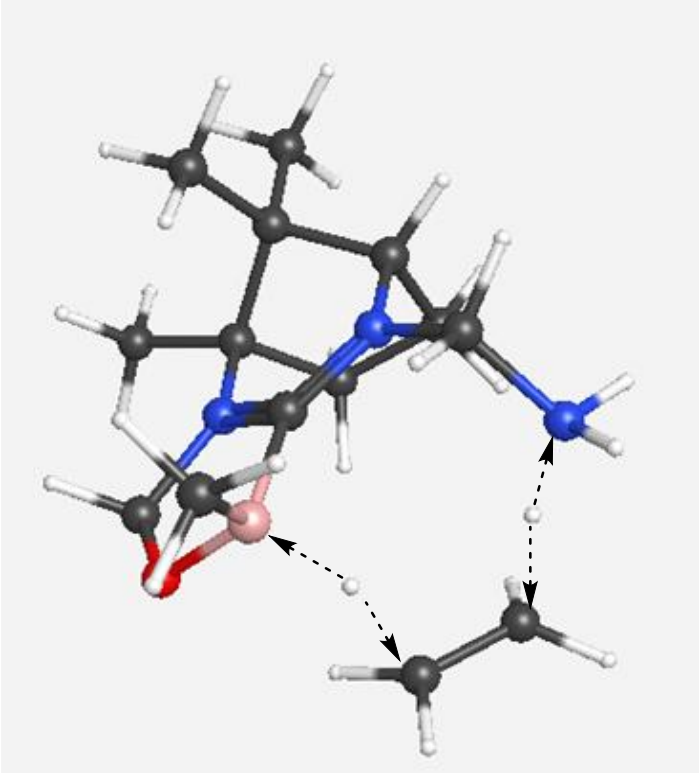

Figure 4.2 Optimized structure of the transition sate for hydrogenation of ethene.

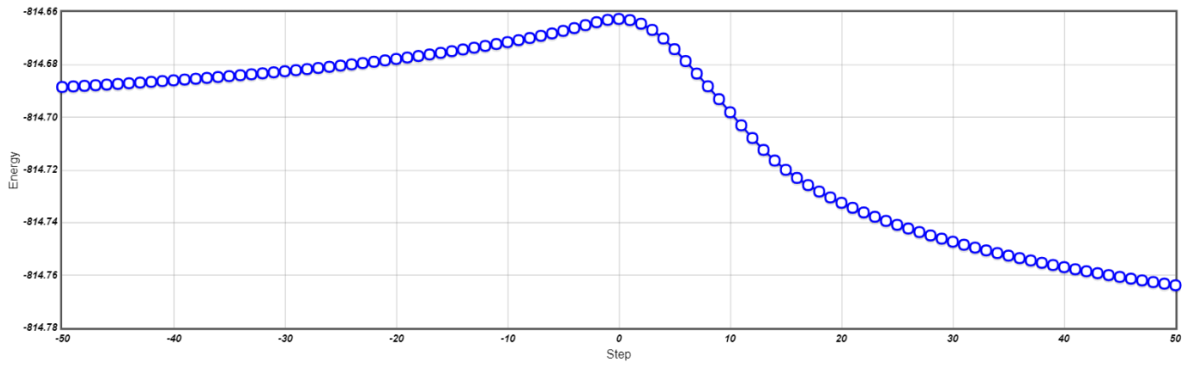

Figure 4.3 Energetics of the IRC calculation.

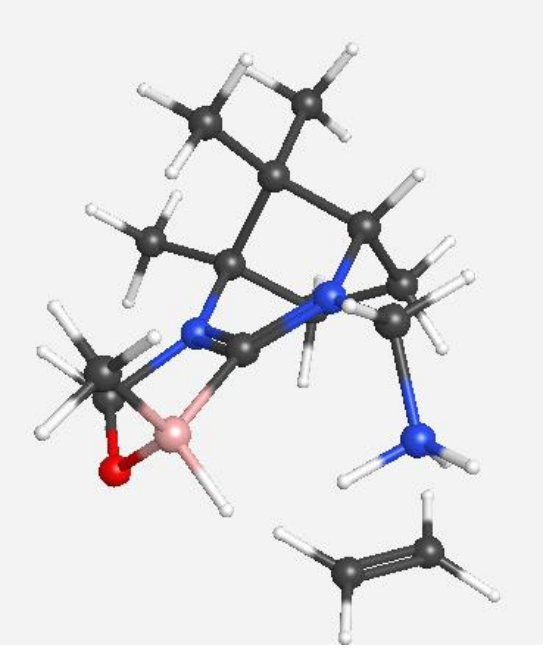

Figure 4.4 Optimized structure of the actual reactant from IRC.

When the energy of this reactant was compared with the starting structure, it was found that there was difference of 13 kJ mol^{-1} between them. A comparison of some specific bond lengths between reactant optimized at start and the reactant optimized from the IRC is shown 4.5.

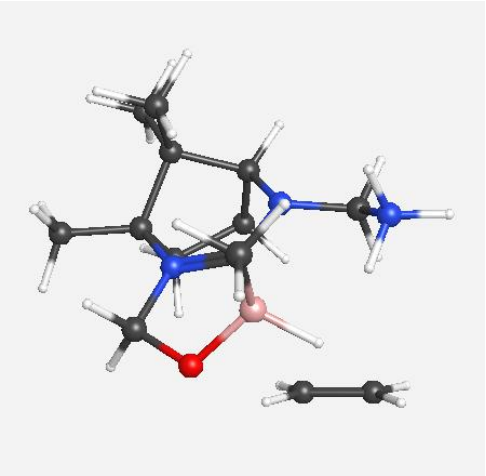

Original reactant geometry

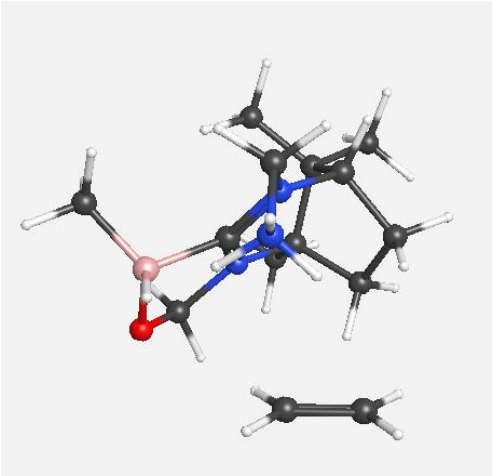

Reactant geometry from IRC

Figure 4.5 Comparison of bond lengths of the original reactant and the reactant obtained from IRC.

A glance at Figure 4.5 reveals that the difference of 13 kJ mol^{-1} between the two structures may be due more distance between oxygen of FLP and carbon of olefin (3.52 Å) in the reactant geometry obtained from IRC which in turn may relieve the steric strain in the molecule. In addition the distance between N-H…..C=C is only 2.82 Å that may increase the chances of hydrogenation. Optimized structure of the final product from the IRC is shown in Figure 4.6. Energy profile diagram of the above transformation is depicted in Figure 4.7.

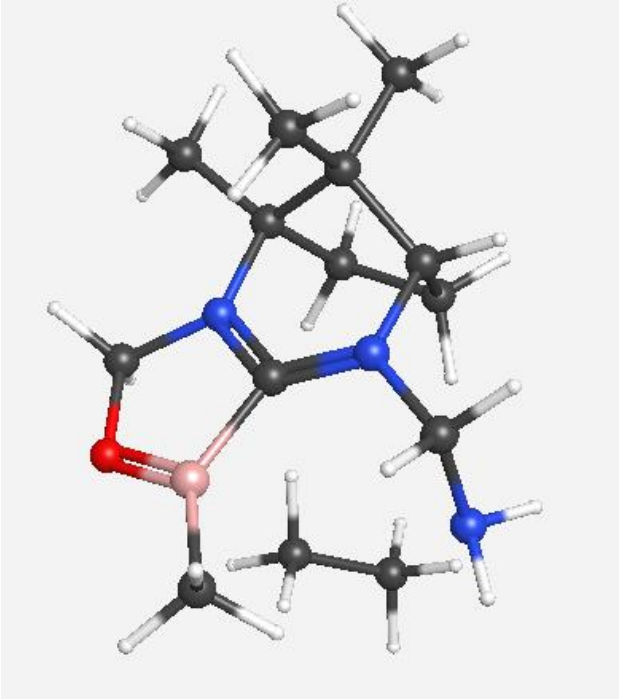

Figure 4.6 Optimized structure of the product from IRC.

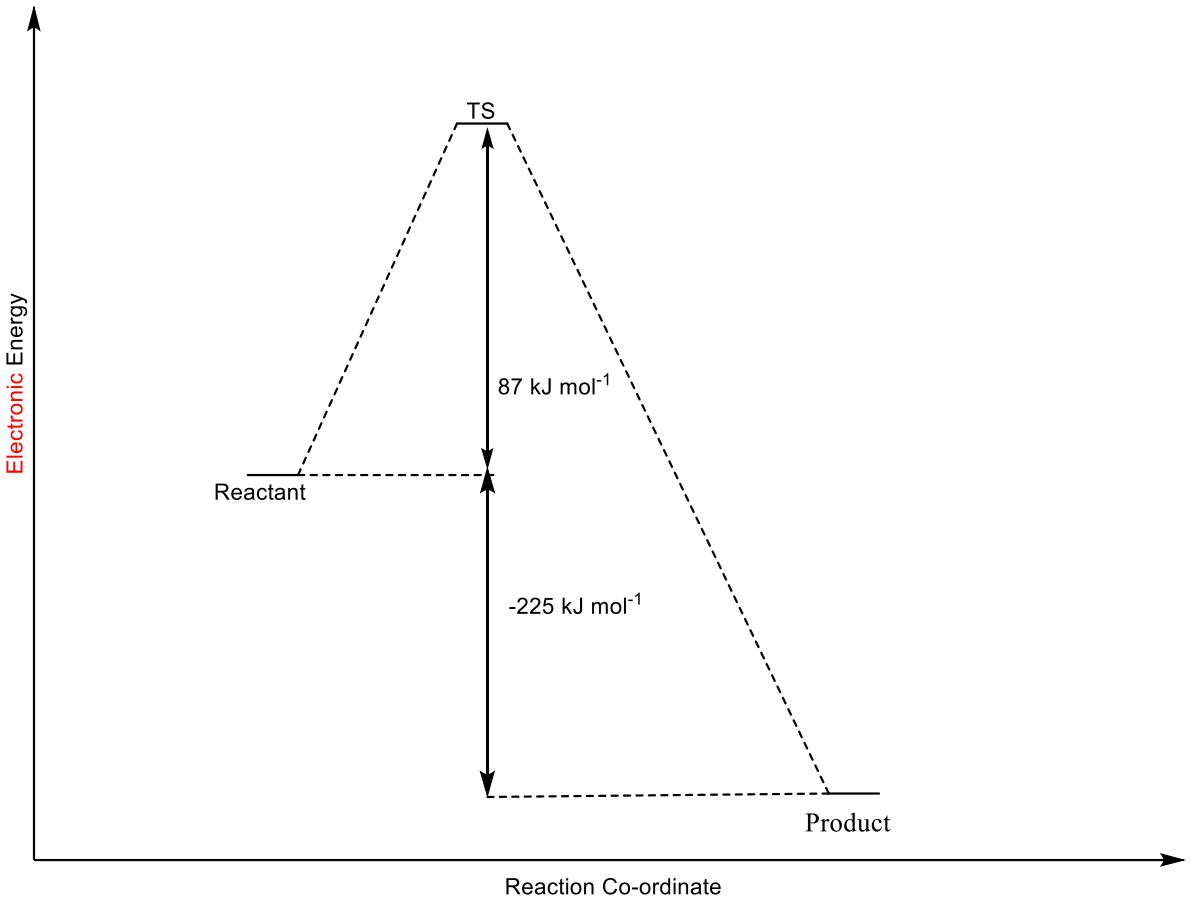

Figure 4.7 Energy (electronic energy) profile diagram for hydrogenation of olefins.

The energy profile diagram reveals that the overall reaction is strongly exothermic and requires 87 kJ mol^{-1} of activation energy. A study of the selected bond lengths (bond orders) which participate in the transition state (Figure 4.8) indicate that the reaction is concerted and synchronous. Energetics of the whole transformation is given in Table 4.1.

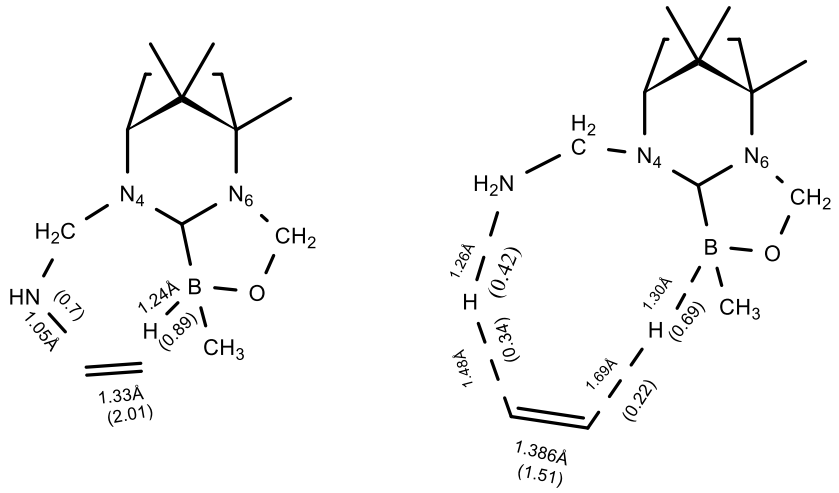

Figure 4.8 Comparison of the bond lengths and (bond orders) of some selected bonds that participate actively in hydrogenation.

Substrate	**Electronic E /Hartrees**	***Δ‡E* /kJ mol^{-1}**	***Δ‡H* /kJ mol^{-1}**	***Δ‡G⁰* /kJ mol^{-1}**	***ΔE* /kJ mol^{-1}**	***ΔH* /kJ mol^{-1}**	***ΔG⁰* /kJ mol^{-1}**
Gas Phase							
Reactant	-814.6956252						
Product	-814.7812321				-225	-217	-221
TS	-814.6626729	87	73	82			
Toluene							
Reactant	-814.7583377						
Product	-814.8349848				-201	-193	-197
TS	-814.7218412	96	82	91			

Table 4.1 Energetics for hydrogenation of ethene using **4a(i)** FLP.

To check whether the mechanism is consistent the same set of calculations were done using **4a(iii)** FLP (the base is $–PH_2$ in this FLP) also. Figure 4.9 represent the optimized geometry of the reactant using **4a(iii)** FLP.

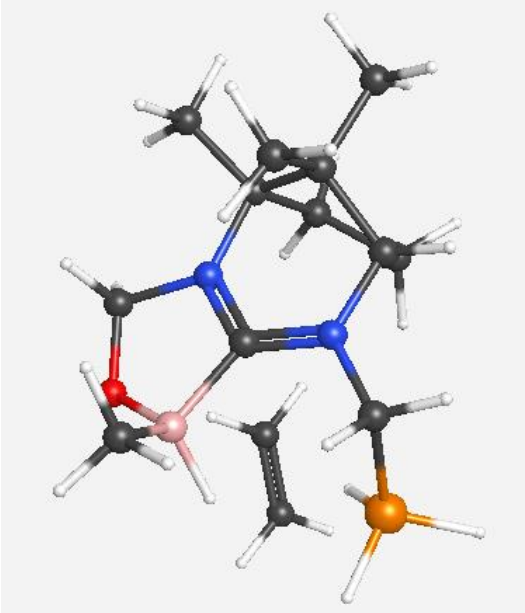

Figure 4.9 Optimized geometry of the reactant using **4a(iii)** FLP.

As in the previous case the transition state was obtained from taking probable points in the scan calculation. It contained only one imaginary frequency (1049i cm^{-1}) as before. Figure 4.10 depicts the optimized geometry of the transition state using **4a(iii)** FLP. IRC (Figure 4.11) was also done to ensure that this transition state connects to the expected reactant and product.

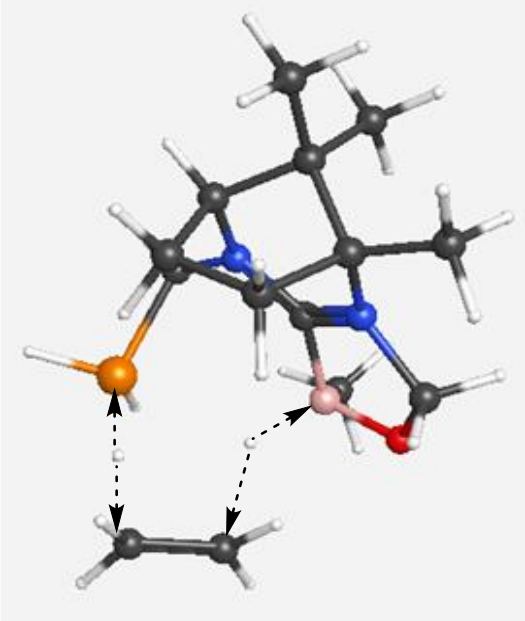

Figure 4.10 Optimized structure of the transition state using **4a(iii)** FLP.

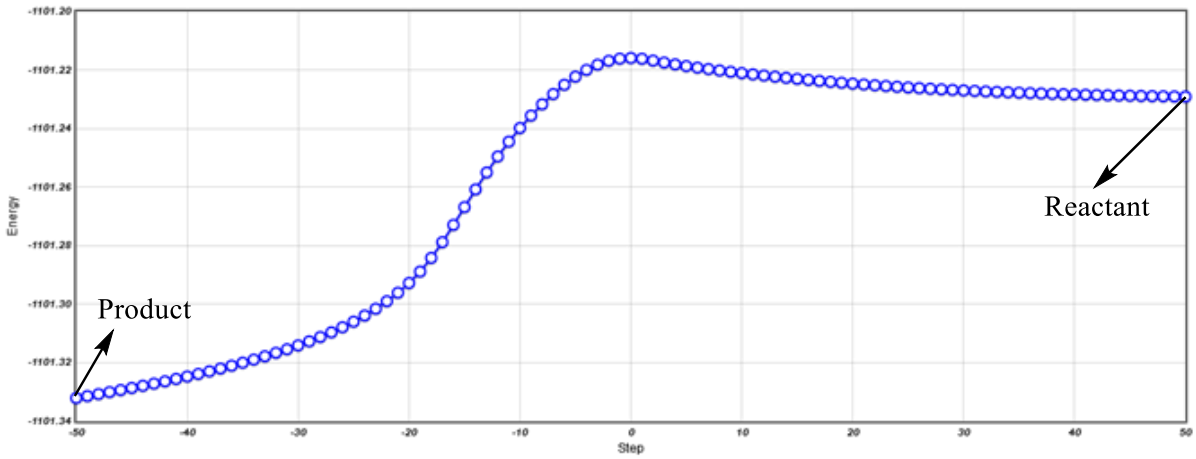

Figure 4.11 IRC of the reaction with **4a(iii)** FLP.

Again, optimization of the start and end points of IRC was done to get the actual structure of the reactant and the product. Figure 4.12 shows the structure of the reactant obtained from IRC, and structure of the product obtained from IRC is represented in Figure 4.13.

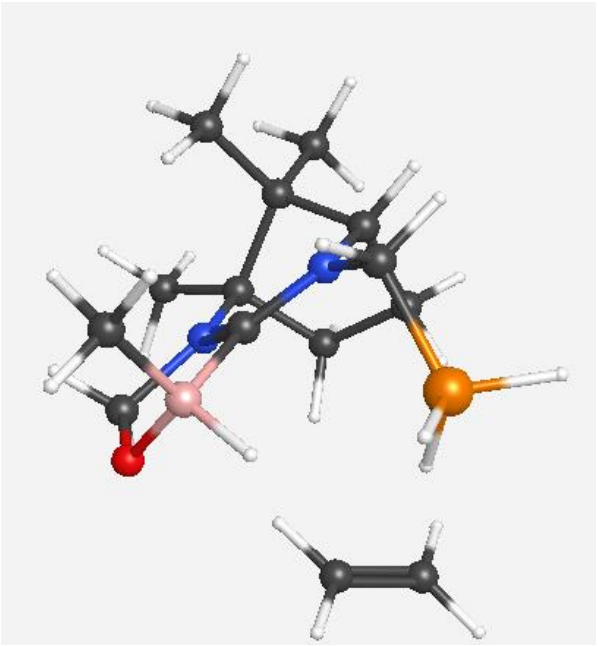

Figure 4.12 Optimized structure of the reactant [using **4a(iii)** FLP] from IRC.

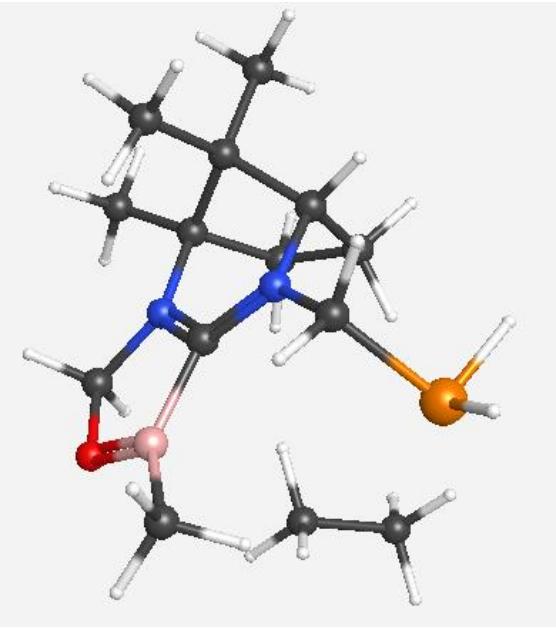

Figure 4.13 Optimized structure of the product [using **4a(iii)** FLP] obtained from IRC.

Energetics of the transformation using **4a(iii)** FLP is summarized in Table 4.2. A comparison of Table 4.1 and 4.2 reveals that activation energy is less for **4a(iii)** as compared to **4a(i)** which may be attributed to the fact that N has more proton affinity

as compared to P, hence, it is easier for phosphorus to lose a hydrogen rather than nitrogen.

Substrate	**Electronic E /Hartrees**	$\Delta^{\ddagger}E$ **/kJ mol^{-1}**	$\Delta^{\ddagger}H$ **/kJ mol^{-1}**	$\Delta^{\ddagger}G^{0}$ **/kJ mol^{-1}**	ΔE **/kJ mol^{-1}**	ΔH **/kJ mol^{-1}**	ΔG^{0} **/kJ mol^{-1}**
Gas Phase							
Reactant	-1101.232621						
Product	-1101.351228				-311	-297	-292
TS	-1101.215892	44	32	42			
Toluene							
Reactant	-1101.292922						
Product	-1101.403127				-289	-275	-270
TS	-1101.274176	49	38	47			

Table 4.2 Energetics for hydrogenation of olefins using **4a(iii)** FLP.

Above mechanism was also tried with FLPs that had boron attached with C_6F_5 instead of CH_3, to see the effect of electron withdrawing substituent. **4a(xvii)** FLP [the base is $–NH_2$ and B is attached with C_6F_5] was selected for understanding the mechanism as it was the analogous to **4a(i)** except for the C_6F_5 substituent on B. As in the previous study, the calculations were initiated with geometry optimization of reactant. Figure 4.14 depicts the optimized geometry of reactant.

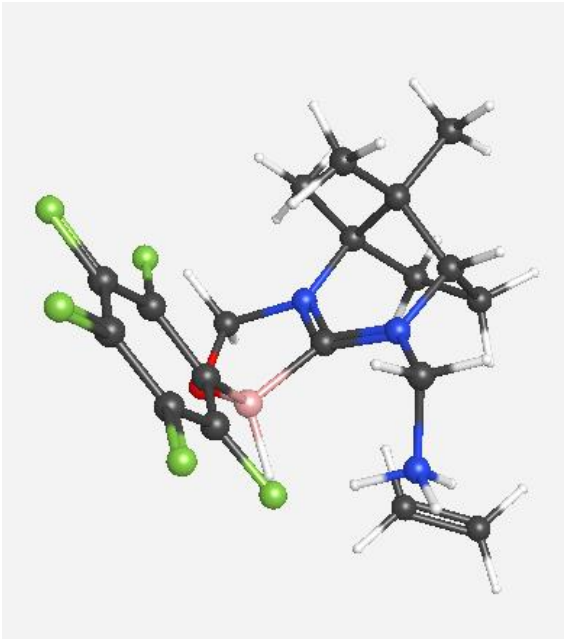

F**igure 4.14** Optimized geometry of reactant using [using **4a(xvii)** FLP].

As in the earlier part of the section, the scans were done in the next phase and the transition state was tried from the probable points on the scan. Figure 4.15 shows the optimized structure of the transition state, that exhibits only one imaginary frequency (1346i cm^{-1}) corresponding to concerted motion of hydrogens.

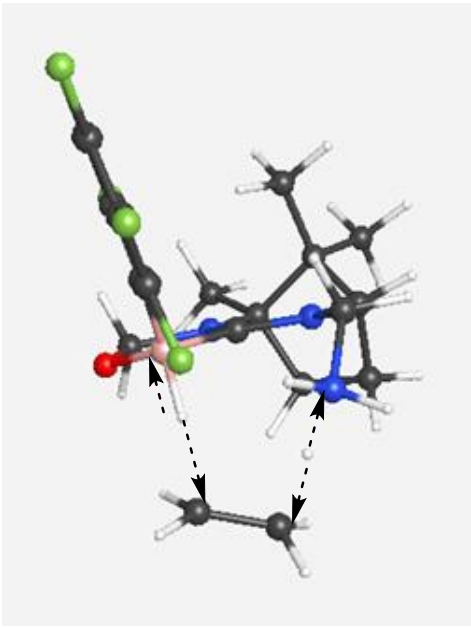

Figure 4.15 Optimized structure of the transition state using [using **4a(xvii)** FLP].

As before IRC was used to see if the transition state connects with the reactant and product on either end. Optimization was done at the start and end point of IRC to get the actual structure of the reactant and product. Figure 4.16 shows the geometry of the reactant obtained from IRC, while Figure 4.17 represents the optimized geometry of the product [using **4a(xvii)** FLP] obtained from IRC. Energetics of the transformation using **4a(xvii)** FLP is summarized in Table 4.3.

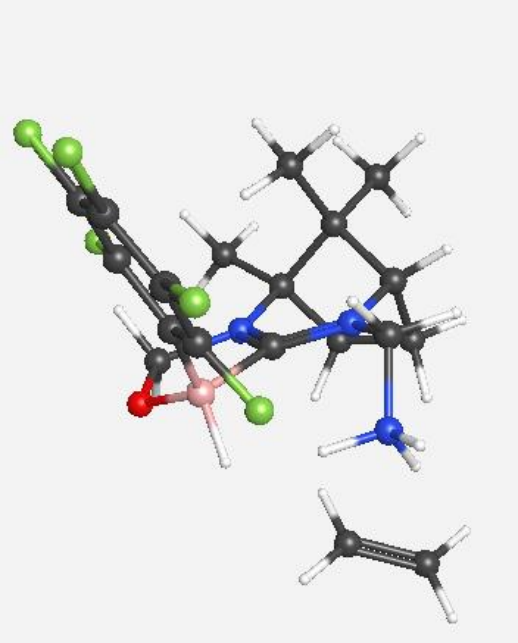

Figure 4.16 Optimized geometry of the reactant [using **4a(xvii)** FLP] obtained from IRC.

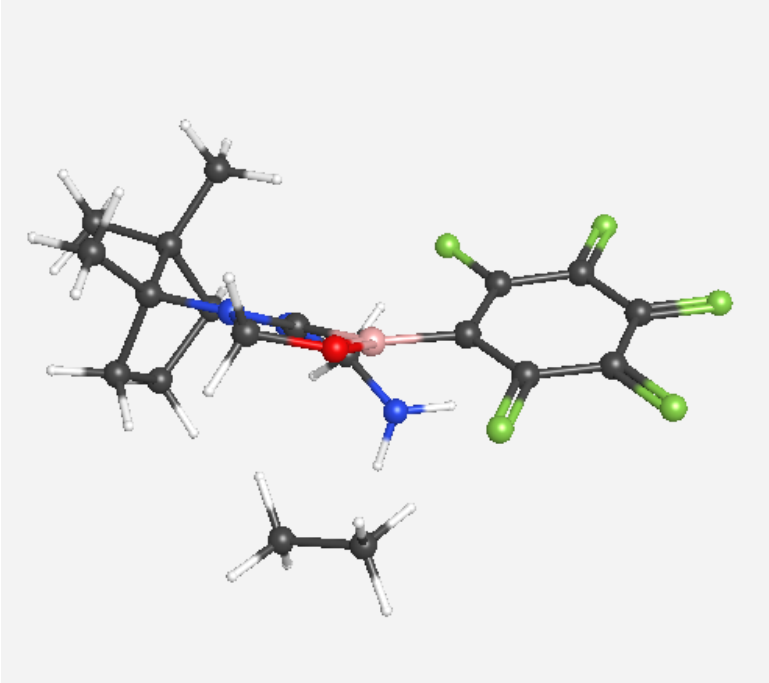

Figure 4.17 Optimized geometry of the product [using **4a(xvii)** FLP] obtained from IRC.

Substrate	**Electronic E /Hartrees**	**$\Delta^{\ddagger}E$ /kJ mol^{-1}**	**$\Delta^{\ddagger}H$ /kJ mol^{-1}**	***$\Delta^{\ddagger}G^{0}$*** **/kJ mol^{-1}**	***ΔE*** **/kJ mol^{-1}**	***ΔH*** **/kJ mol^{-1}**	***ΔG^{0}*** **/kJ mol^{-1}**
Gas Phase							
Reactant	-1502.372684						
Product	-1502.43832				-172	-167	-168
TS	-1502.337017	94	78	87			
Toluene							
Reactant	-1502.435024						
Product	-1502.491384				-148	-142	-143
TS	-1502.393846	108	92	101.37			

Table 4.3 Energetics of the hydrogenation reaction with **4a(xvii)** FLP.

Finally, the same steps were repeated with **4a(xix)** FLP [base is $–PH_2$ and B is attached with C_6F_5] as well because it was analogous to **4a(iii)** except for the C_6F_5 substituent on B. The calculations were initiated with geometry optimization of reactant. Figure 4.18 depicts the optimized geometry of reactant. Figure 4.19 represents the optimized structure of the transition state that has one imaginary frequency (902i cm^{-1}). A glance at Figure 4.19 reveals that the hydrogen attached with the phosphorous on FLP in the reactant has detached but the hydrogen attached with boron has not yet detached from the reactant.

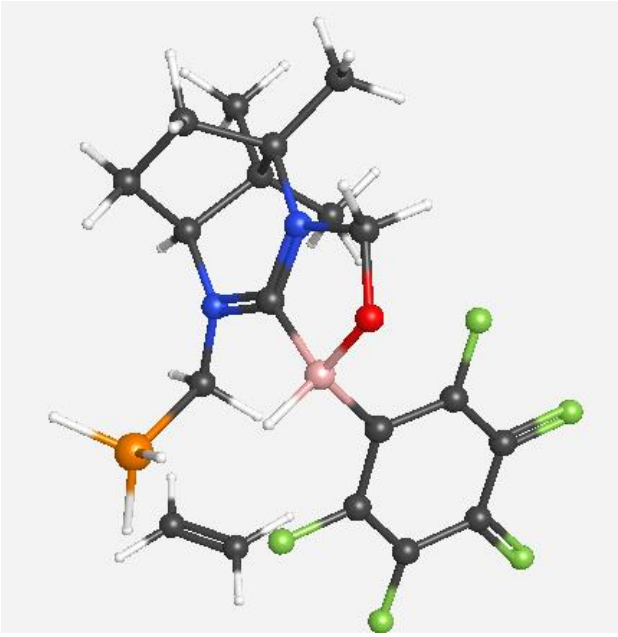

Figure 4.18 Optimized geometry of the reactant using **4a(xix)** as FLP.

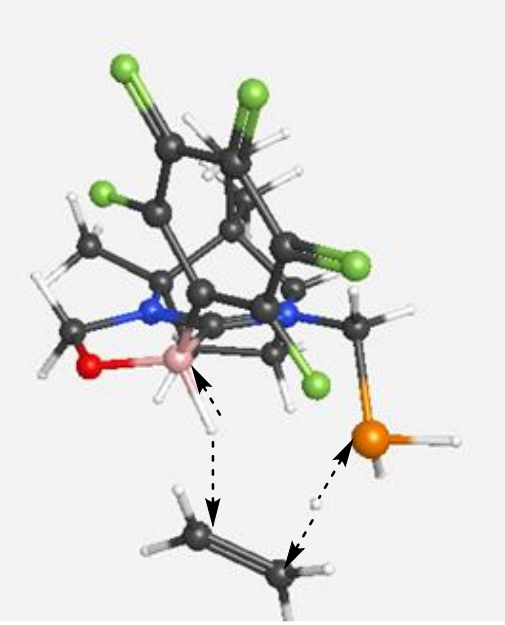

Figure 4.19 Optimized geometry of the transition state using **4a(xix)** as FLP.

IRC calculation confirmed that as in the previous cases here also transition state connects to the reactants on the one end of IRC and product on the other. Optimization was done at the start and end point of IRC to get the actual structure of the reactant and product. Figure 4.20 shows the optimized geometry of the reactant obtained from IRC, and Figure 4.21 represents the geometry of the product obtained from IRC. Energetics of the transformation using **4a(xix)** FLP is summarized in Table 4.4. Complete catalytic cycle for hydrogenation may be depicted as in Figure 4.22.

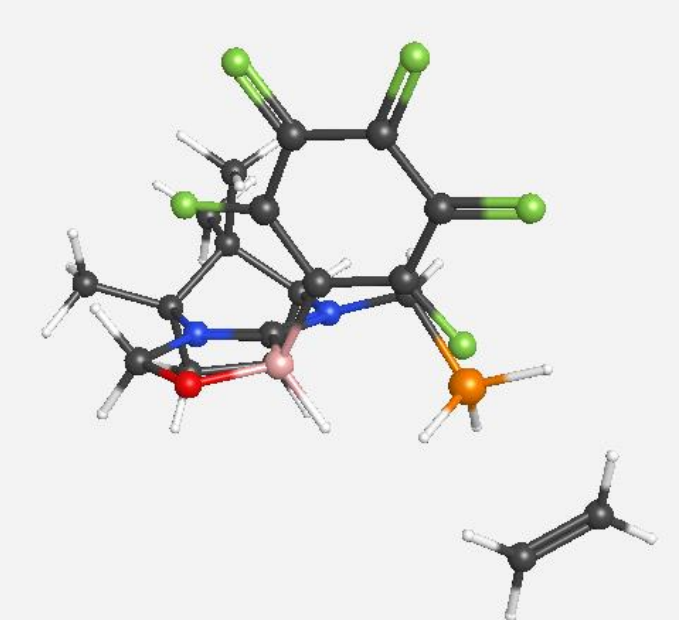

Figure 4.20 Optimized geometry of the reactant [using **4a(xix)** FLP] obtained from IRC.

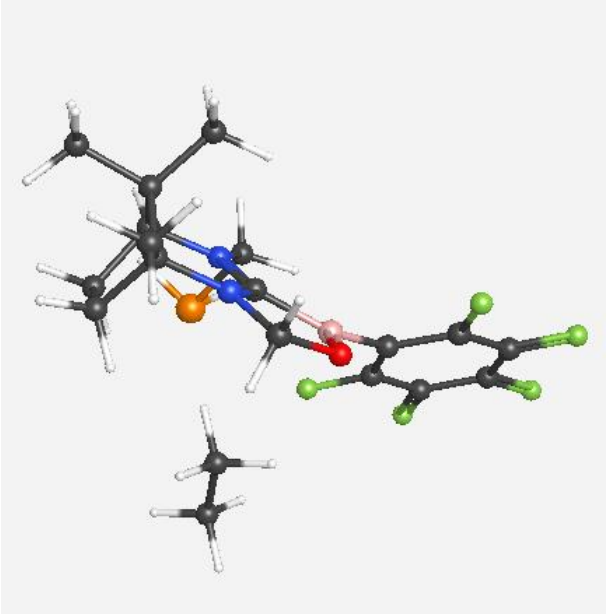

Figure 4.21 Optimized geometry of the product [using **4a(xix)** FLP] obtained from IRC.

Substrate	E /Hartrees	$\Delta^{\ddagger}E$ /kJ mol^{-1}	$\Delta^{\ddagger}H$ /kJ mol^{-1}	$\Delta^{\ddagger}G$ /kJ mol^{-1}	ΔE /kJ mol^{-1}	ΔH /kJ mol^{-1}	ΔG /kJ mol^{-1}
Gas Phase							
Reactant	-1788.908079						
Product	-1789.00556				-256	-245	-243
TS1	-1788.893963	37	31	37			
Toluene							
Reactant	-1788.968931						
Product	-1789.057148				-232	-221	-219
TS1	-1788.948749	53	47	53			

Table 4.4 Energetics of the hydrogenation reaction with **4a(xix)** FLP.

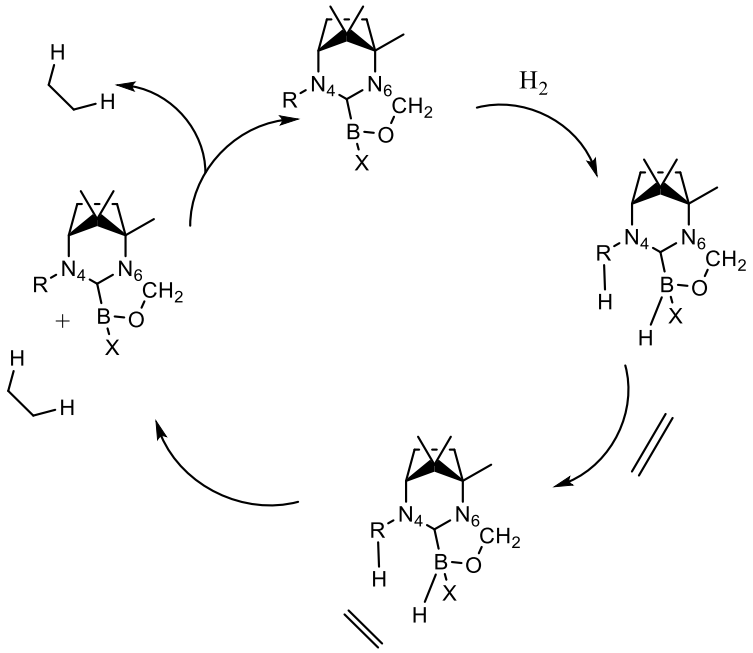

4a(i) R= -CH_2-NH_2; X=CH_3
4a(iii) R= -CH_2-PH_2; X=CH_3
4a(xvii) R= -CH_2-NH_2; X=C_6F_5
4a(xix) R= -CH_2-PH_2; X=C_6F_5

Figure 4.22 Catalytic cycle for hydrogenation of olefins.

Comparison of energetics of hydrogenation of olefins by all the four used FLPs is given in Table 4.5. A glance at the table reveals few interesting facts. The activation barrier is lowered when the base is -PH_2 [**4a(iii)**/**4a(xix)**] instead of -NH_2 [**4a(i)**/**4a(xvii)**]. This may be attributed to the fact that primary phosphines are weaker bases than primary amines and thus can easily lose hydrogen attached to it. The barrier is raised when B is attached with C_6F_5 [**4a(xvii)**/**4a(xix)**] rather when it is attached with CH_3 [**4a(i)**/**4a(iii)**] in the solvent. This may be due to fact that the electron withdrawing C_6F_5 group makes boron an even stronger Lewis acid which in turn becomes reluctant to lose its hydrogen.

It may be noted that the above-mentioned trend is observed only in solvent phase and not in gaseous one but then mechanism of the reaction in presence of solvent presents a more realistic model as compared to the gaseous one. It is observed that all the $\Delta^{\ddagger}G$ values are higher and the ΔG values less negative in solvent (Toluene) than in the gaseous phase. The reason for this observation may be the fact that solvent stabilizes the reactants (where FLP has full positive charge) much more than the TS (where the charge is partial) and hence the barrier increases. On the other hand, products are less stabilized than the reactant (where the positive charge is less intense due to dative bond of carbene) and so the ΔG values become less negative.

Substrate	$\Delta^{\ddagger}G$ /kJmol^{-1}	ΔG /kJmol^{-1}
Gas Phas0e		
4a(i)	82	-221
4a(iii)	42	-292
4a(xvii)	87	-168
4a(xix)	37	-243
Toluene		
4a(i)	91	-197
4a(iii)	47	-270
4a(xvii)	101	-143
4a(xix)	53	-219

Table 4.5 Comparisons of energetics of hydrogenation of olefins by FLPs.

Table 4.6 provides the energetics of overall hydrogenation of olefins by FLPs in solvent. A look at the data reveals that **4a(xvii)** might prove to be the best choice for laboratory synthesis.

FLP	Hydrogen activation by FLP		Hydrogenation of olefin	
	$\Delta^{\ddagger}G$ /kJ mol^{-1}	ΔG /kJ mol^{-1}	$\Delta^{\ddagger}G$ /kJ mol^{-1}	ΔG /kJ mol^{-1}
4a(i)	91	84	82	-221
4a(iii)	184	169	42	-292
4a(xvii)	68	33	87	-168
4a(xix)	113	101	37	-243

Table 4.6 Energetics of complete overall mechanism of hydrogenation of olefins.

4.2 Hydrogenation of Aldehydes (Formaldehyde) by FLP 4a(i)/H_2 system

After understanding the mechanism of hydrogenation of olefins, we applied the same method to understand hydrogenation of aldehydes. The steps involved were the same as in the case of olefins. The study was started with optimizing the geometries of reactant [activated-FLP and formaldehyde] and product (FLP and methanol). Figure 4.23 depicts the optimized geometry of the reactant that was obtained after trying various other possible conformations that had higher energy. The stability of this conformer may be attributed to the fact that in this conformation, carbonyl oxygen comes close (2.11 Å) to the hydrogen of the amine group in the FLP and hence the hydrogen bond formed as a result may increase its stability.

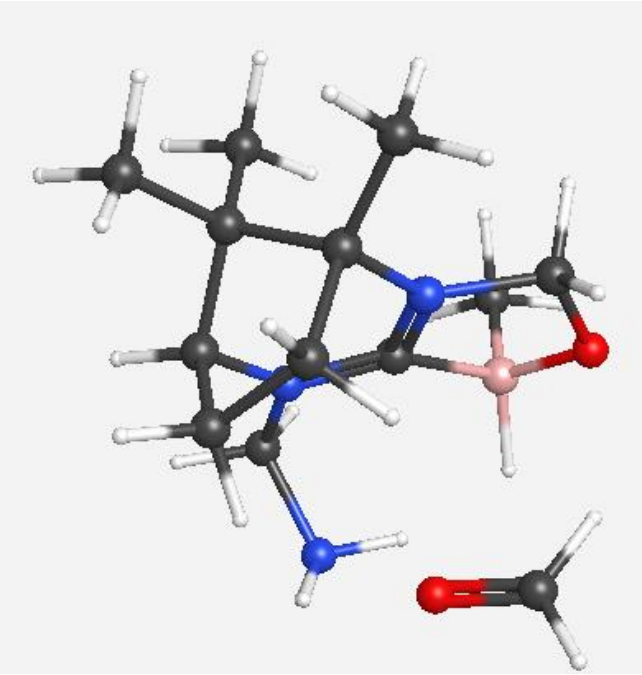

Figure 4.23 Optimized geometry of the reactant at M06-2X/6-31G(d) level of theory.

In the next part of the study scans were done to understand the movement of hydrogen from FLP to aldehyde. Transition state connecting reactant and product was tried from various potential points in the scan plot. Transition state was obtained which had only one imaginary frequency (216i cm^{-1}) that corresponds to a normal mode for simultaneous movement of hydrogens. Figure 4.24 represents the optimized geometry of the same.

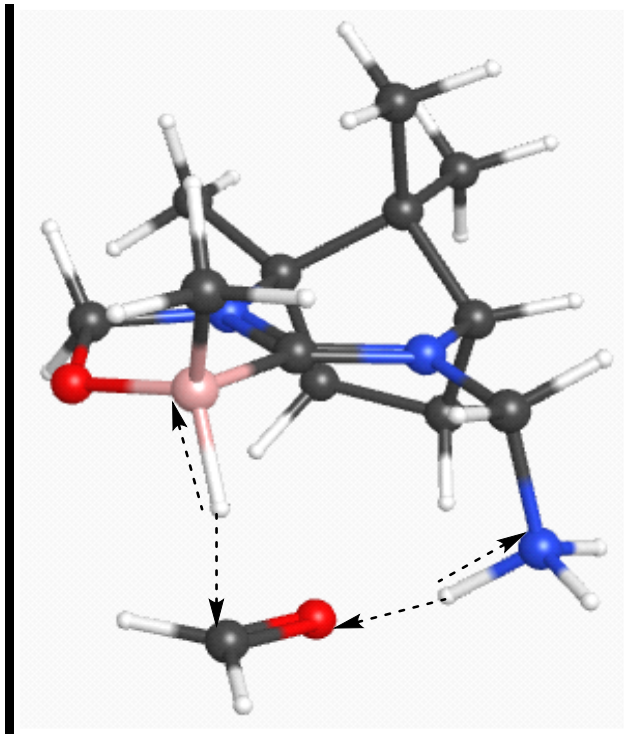

Figure 4.24 Optimized geometry for the transition state for hydrogenation of formaldehyde.

IRC calculation was also run to find if this TS connected the reactants and the products. It was found that the TS connected reactant on one end and an intermediate at the other which is actually the product still bonded with the catalyst. In this intermediate the CH_3OH (product) was not separated from catalyst but bound to boron of FLP via carbonyl oxygen. B…O bond in this intermediate had 1.69 Å bond length

and 0.4 bond order. Figure 4.25 represents the optimized geometry of the reactant from IRC. Optimized structure of the intermediate is depicted in Figure 4.26.

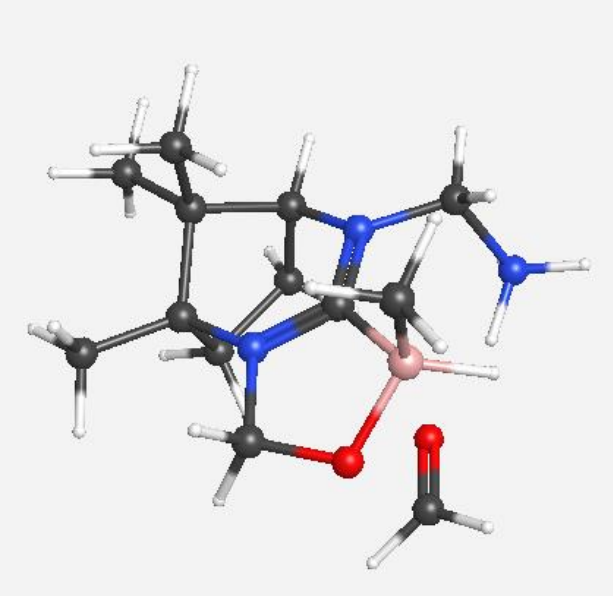

Figure 4.25 Optimized geometry of the reactant from IRC.

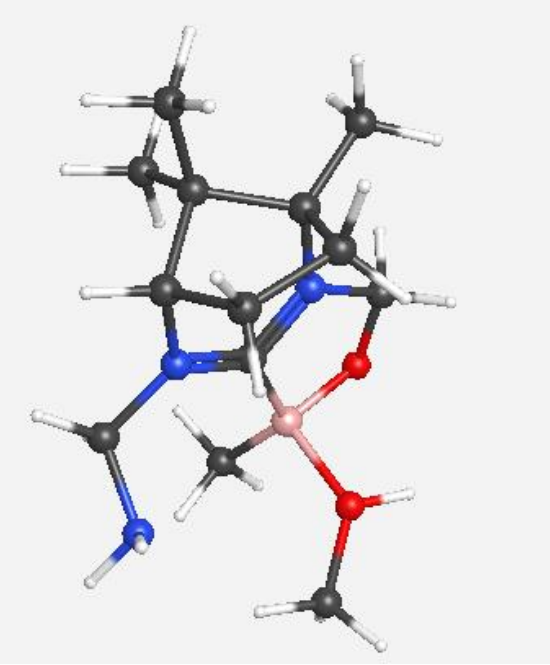

Figure 4.26 Optimized geometry of the intermediate from IRC.

In the next part the transition state was located which connected this intermediate with the product. Figure 4.27 represents the optimized geometry of the transition state that had single imaginary frequency (53i cm^{-1}).

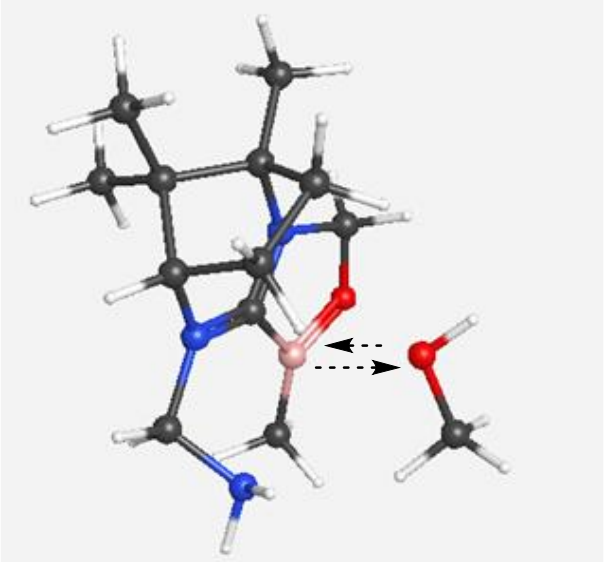

Figure 4.27 Optimized geometry of the transition state that connects to intermediate and product.

IRC revealed that this transition state connects to the intermediate on one end of IRC and to the product on the other. Figure 4.28 shows the optimized geometry of the product from IRC.

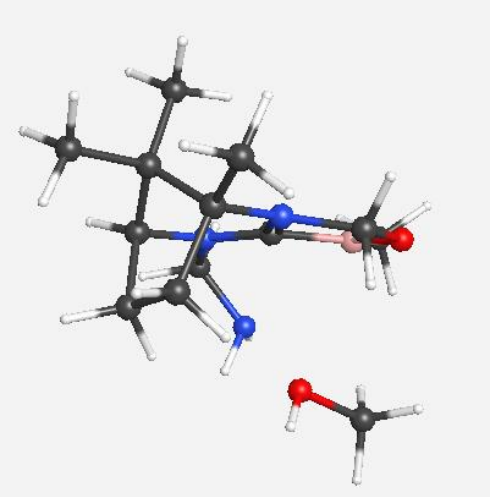

Figure 4.28 Optimized geometry of the product from IRC.

A comparison of change in the bond lengths (bond orders) of the key bonds participating in the hydrogenation process are shown in Figure 4.29. The values indicate the hydrogenation of formaldehyde is concerted and synchronous. Energetics of the whole transformation is depicted in Table 4.6.

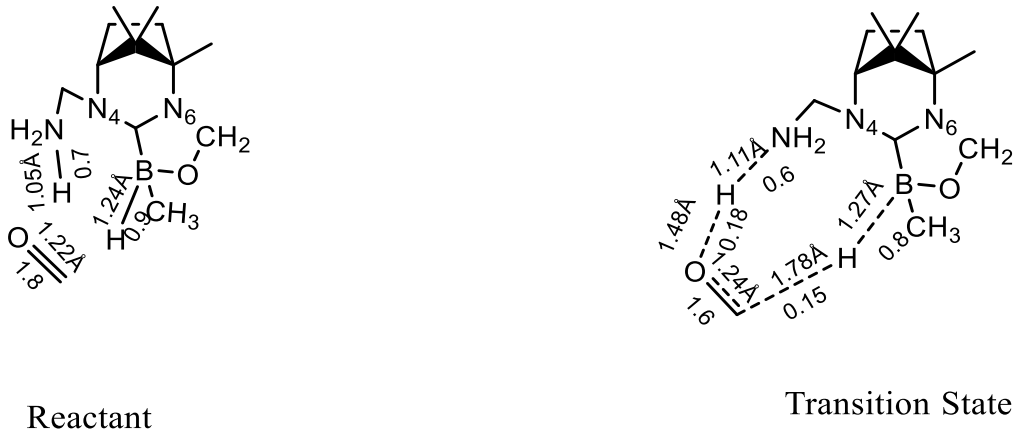

Figure 4.29 Comparison of change in bond lengths (bond orders) of the key bonds participating in hydrogenation of formaldehyde.

Substrate	**Electronic E /Hartrees**	$\Delta^{\ddagger}E$ **kJ mol^{-1}**	$\Delta^{\ddagger}H$ **kJ mol^{-1}**	$\Delta^{\ddagger}G$ **kJ mol^{-1}**	ΔE **kJ mol^{-1}**	ΔH **kJ mol^{-1}**	ΔG **kJ mol^{-1}**
Gas Phase							
Reactant	-850.6235907						
Product	-850.6770706				-140	-133	-143
Intermediate	-850.6882601				-170	-161	-163
TS1	-850.6118031	31	23	23			
TS2	-850.6767301	30	25	17			
Toluene							
Reactant	-850.684596						
Product	-850.7273656				-112	-105	-114
Intermediate	-850.7401215				-146	-137	-139
TS1	-850.6726999	31	23	23			
TS2	-850.7275629	33	28	20			

Table 4.6 Energetics of hydrogenation of formaldehyde.

Energy profile diagram (Figure 4.30) depicts energetics of all the steps taking place in above transformation. Complete catalytic cycle for this transformation has been depicted in Figure 4.31.

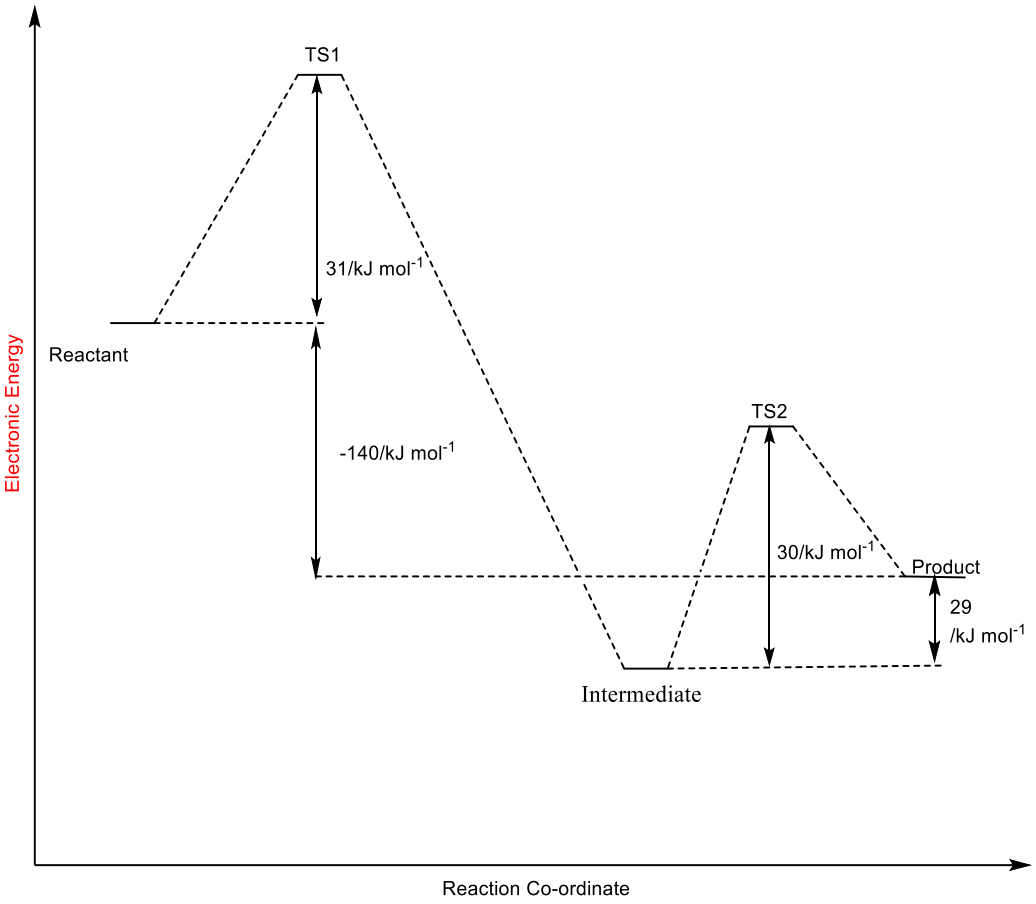

Figure 4.30 Energy profile diagram for hydrogenation of formaldehyde.

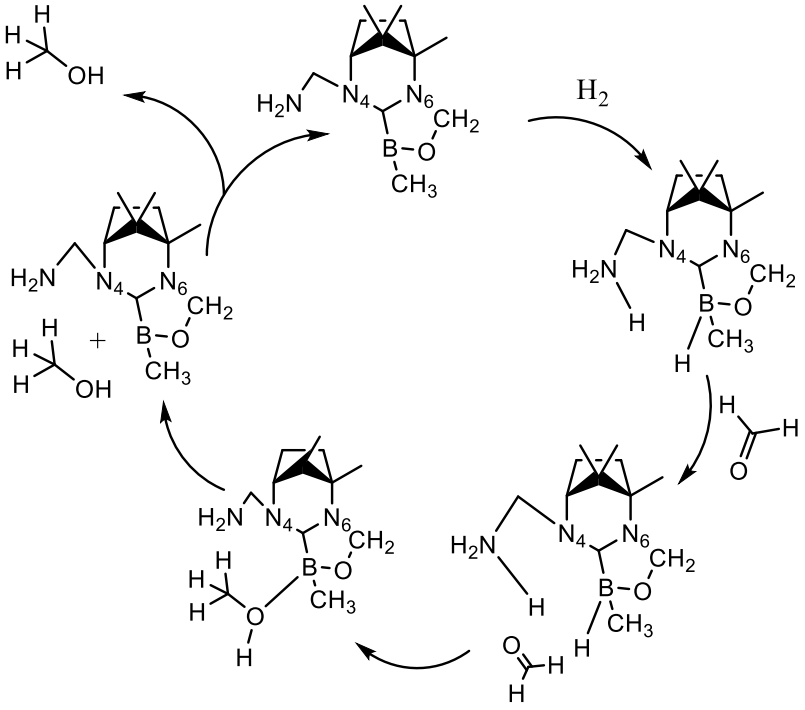

Figure 4.31 Complete catalytic cycle for hydrogenation of Formaldehyde.

Since the above hydrogenation was facile but it took lot of energy to separate the catalyst from the product, it was thought worthwhile to try the same process with bulkier substrates. Hence in this case benzaldehyde was chosen as the substrate and all the calculations done for each step in the previous case were repeated. Figure 4.32 represents the optimized geometry of the transition state [with imaginary frequency of (409i cm^{-1})] between reactant and the intermediate (the product still attached with the catalyst).

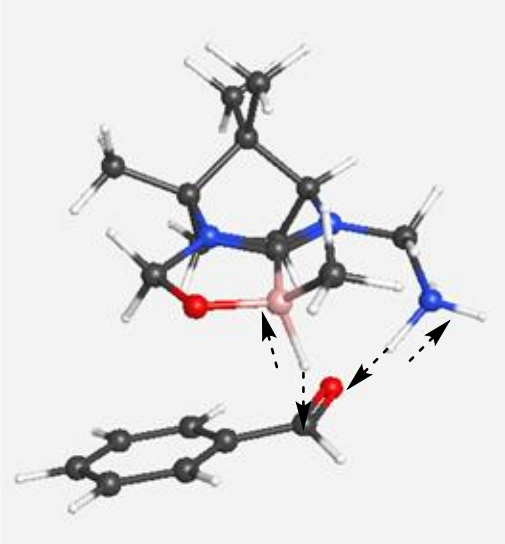

Figure 4.32 Optimized geometry of the transition state.

IRC ensured that the transition state actually connects reactant with the intermediate (product still attached with the catalyst). Figure 4.33 shows the optimized geometry of the reactant and the intermediate from IRC. Table 4.7 summarizes all the energy changes. In this case also it was very difficult to separate the product from the catalyst. Therefore, it was very difficult to separate the final product from the catalyst whether we take small or bulky reactant.

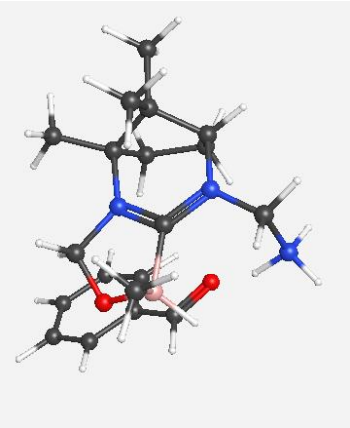

Reactant

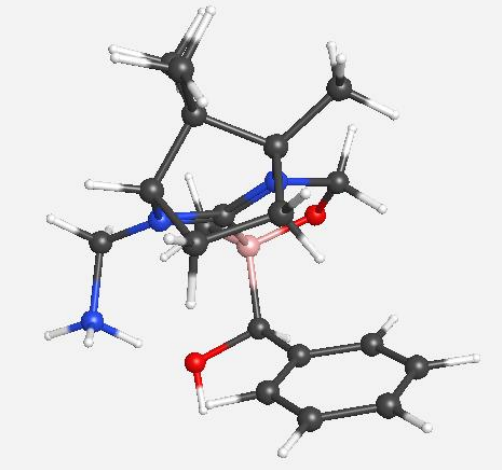

Intermediate

Figure 4.33 Optimized geometry of the reactant and intermediate from IRC.

Substrate	**Electronic E /Hartrees**	***Δ‡E* /kJ mol^{-1}**	***Δ‡H* /kJ mol^{-1}**	***Δ‡G* /kJ mol^{-1}**	***ΔE* /kJ mol^{-1}**	***ΔH* /kJ mol^{-1}**	***ΔG* /kJ mol^{-1}**
Gas Phase							
Reactant	-1081.606737						
Product	-1081.637834				-82	-77	-81
Intermediate	-1081.620419				-36	-33	-23
TS	-1081.591179	41	28	37			
Toluene							
Reactant	-1081.669967						
Product	-1081.694138						
Intermediate	-1081.684847				-39	-36	-26
TS	-1081.652517	46	33	42			

Table 4.7 Energetics for hydrogenation of benzaldehyde.

4.3 Hydrogenation of Ketones (Acetone) by FLP/H_2 system

In the last section hydrogenation of aldehydes was studied in detail. As the activation barrier for this reaction was quite low it was thought worthwhile to explore the hydrogenation of ketones also. All the steps were same as followed in case of hydrogenation of aldehydes. The study was commenced with the geometry optimization of reactant. As it was seen in the last section, in this case also the extra stability of this conformer may be due to the hydrogen bond between carbonyl oxygen (1.78 Å) and hydrogen of amine group in the FLP. Figure 4.34 represents the optimized geometry of the reactant.

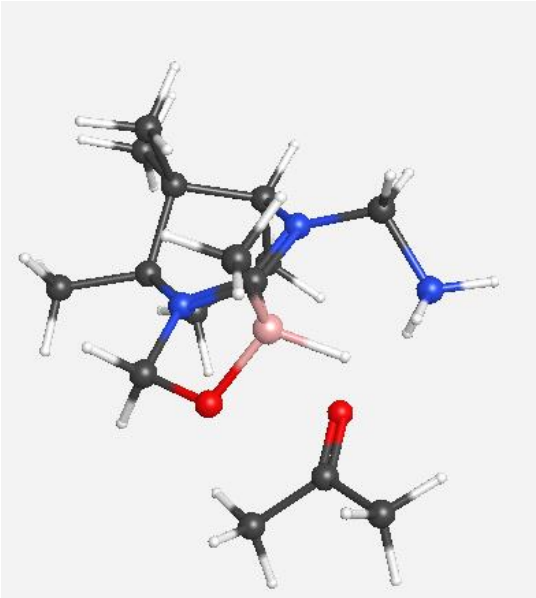

Figure 4.34 Optimized geometry of the reactant.

Next step included the study of scans to understand the movement of hydrogen from FLP to acetone. Transition state connecting reactant and product was tried from various potential points in the scan plot. Transition state was obtained which had only one imaginary frequency (261i cm^{-1}). Figure 4.35 represents the optimized geometry

of the same. IRC calculation was also run to find if this TS connected the reactants and the products. It was found that the TS connected reactant on one end and an intermediate at the other which is the product still bonded with the catalyst. In this intermediate propan-2-ol (product) was not separated from catalyst but bound to the Boron of FLP via carbonyl oxygen. B…O bond in this intermediate had 1.61 Å bond length and 0.5 bond order. Optimized geometry of the reactant from IRC is depicted in Figure 4.36, and intermediate from IRC in Figure 4.37.

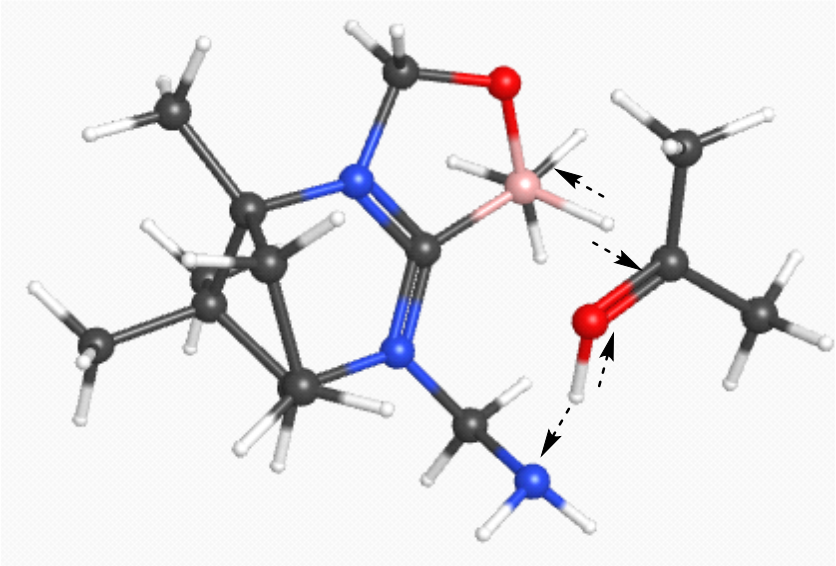

Figure 4.35 Optimized geometry for the transition state for hydrogenation of acetone.

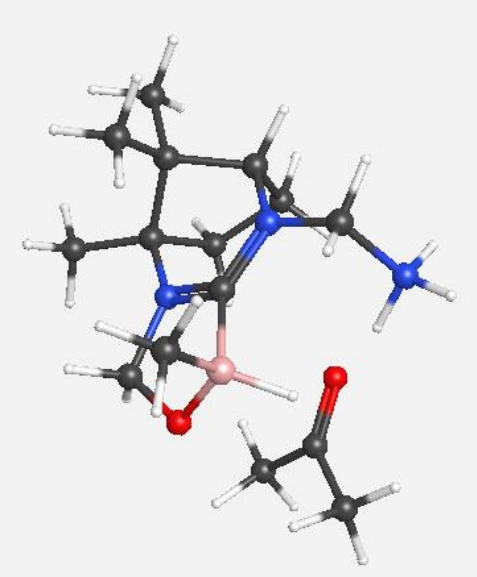

Figure 4.36 Optimized geometry of the reactant from IRC.

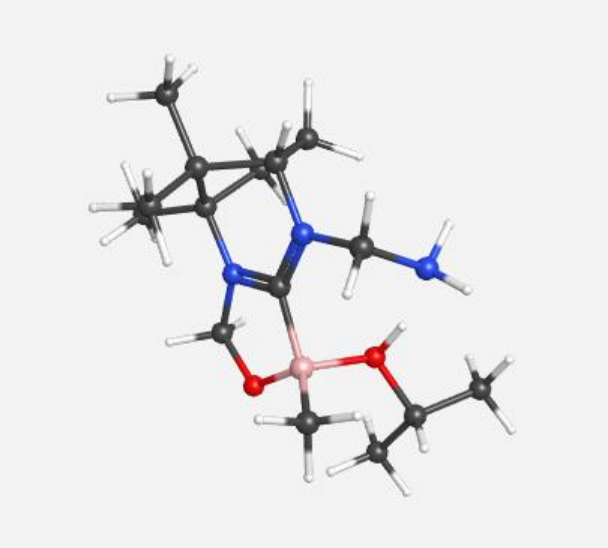

Figure 4.37 Optimized geometry of the intermediate from IRC.

A transition state was located which connected intermediate with product. It also had single imaginary frequency (25i cm^{-1}). The optimized geometry of the second transition state is depicted in Figure 4.38. A comparison of bond lengths (bond orders) of the key bonds participating in the hydrogenation process is shown in Figure 4.39.

Energetics of the whole transformation is depicted in Table 4.8 and depicted in Figure 4.40. Complete catalytic cycle for the transformation is depicted in Figure 4.41.

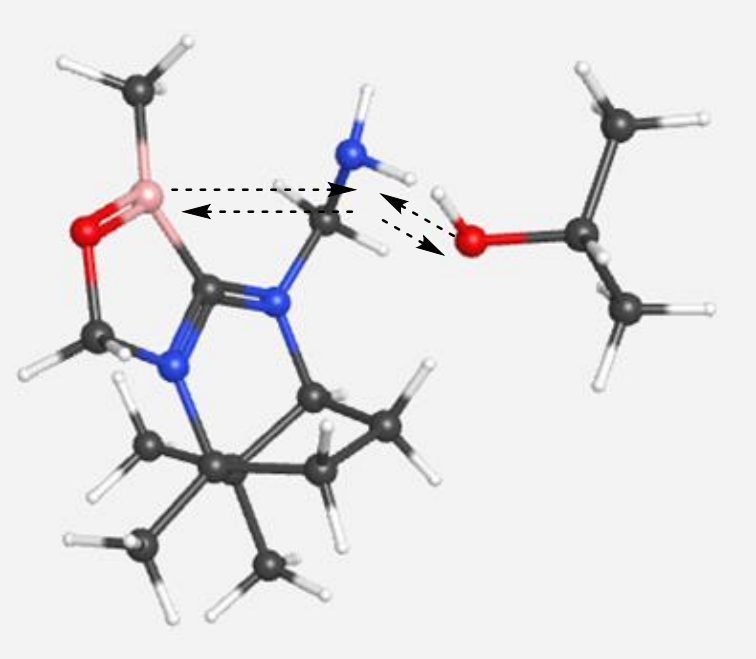

Figure 4.38 Transition state geometry for the for detachment of product from catalyst.

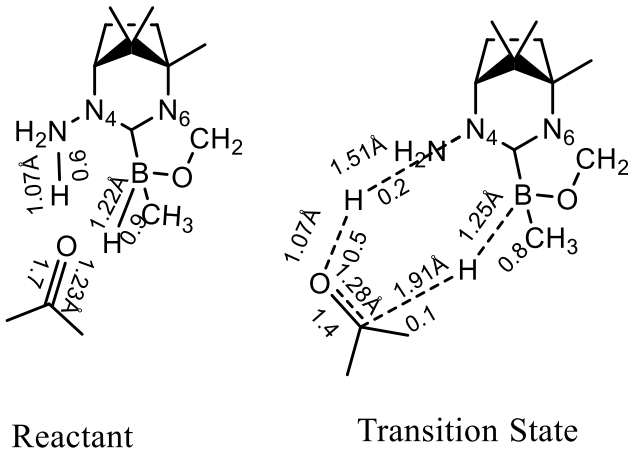

Figure 4.39 Comparison of change in bond lengths (bond orders) of the key bonds participating in hydrogenation of acetone.

Substrate	Electronic E /Hartrees	$\Delta^{\ddagger}E$ /kJ mol^{-1}	$\Delta^{\ddagger}H$ /kJ mol^{-1}	$\Delta^{\ddagger}G$ /kJ mol^{-1}	ΔE /kJ mol^{-1}	ΔH /kJ mol^{-1}	ΔG /kJ mol^{-1}
Gas Phase							
Reactant	-929.2406885						
Product	-929.2756492				-82	-73	-83
Intermediate	-929.3045454				-163	-152	-147
TS1	-929.239377	37	29	34			
TS2	-929.3037729	89	84	75			
Toluene							
Reactant	-929.3038155						
Product	-929.325505				-57	-48	-58
Intermediate	-929.3591917				-145	-135	-130
TS1	-929.2855225	48	40	45			
TS2	-929.3228107	96	91	81			

Table 4.8 Energetics for hydrogenation of acetone.

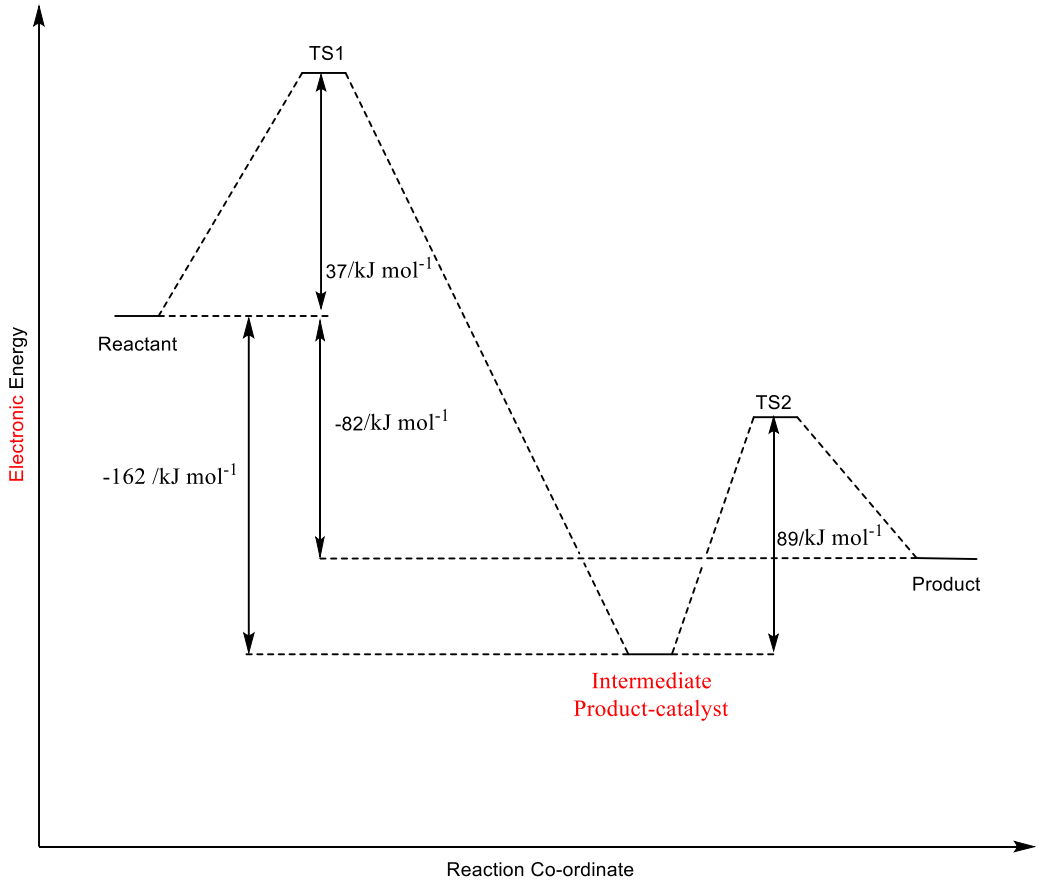

Figure 4.40 Energy profile diagram for hydrogenation of acetone.

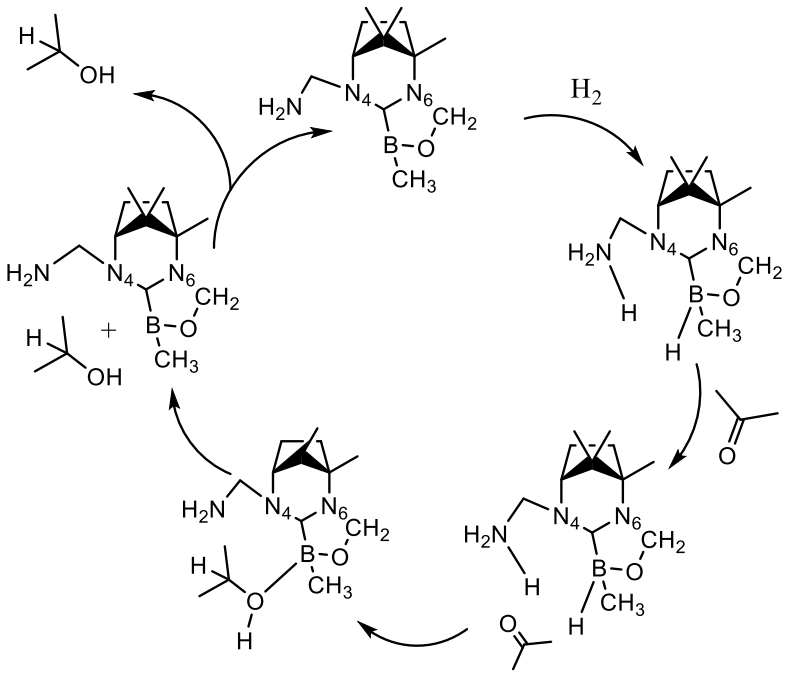

Figure 4.41 Complete catalytic cycle for hydrogenation of ketones (acetone).

4.4 Hydrogenation of Formaldimine by FLP 4a(i)/H_2 system

To gain deeper understanding of the possible scope for hydrogenation of different substrates using FLP catalysis, hydrogenation of formaldimine was also undertaken. The study was commenced with the geometry optimization of reactant. Figure 4.42 represents the optimized geometry of the reactant.

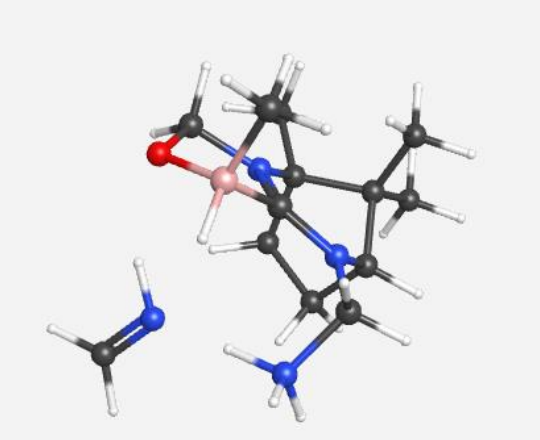

Figure 4.42 Optimized geometry of the reactant.

As in the previous case next step was the study of scans to understand the movement of hydrogen from FLP **4a(i)** to formaldimine. Scan of B-H…C=N distance (starting from H….C distance 3.84 Å and then reducing it gradually) was performed. Searches for transition state connecting reactant and product was tried from various potential points in the scan plot. Transition state was obtained which had only one imaginary frequency (142i cm^{-1}) but the activation energy ($\Delta E^{\ddagger}$) of the TS was slightly less than the reactant (-0.11 kJ mol^{-1}) although $\Delta G^{\ddagger}$ was little positive (0.15 kJ mol^{-1}). These values indicated that it was a case of barrierless reaction. Figure 4.43 represents the optimized geometry of the transition state (TS1) obtained.

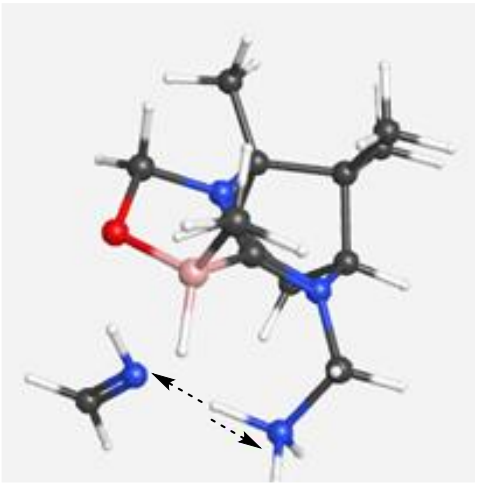

Figure 4.43 Transition state geometry (TS1) for hydrogenation of formaldimine.

IRC calculation was run to find if this TS connected the reactants and the products. It was found that the TS connected reactant on one end and an intermediate (Int1) at the other in which the hydrogen of the basic part of FLP has detached from nitrogen and attached with nitrogen of imine while the hydrogen of the acidic part is still attached with the boron. Figure 4.44 depicts the optimized geometry of the reactant obtained from IRC. The intermediate was also optimized and it had zero imaginary frequencies. Figure 4.45 represents the optimized geometry of the intermediate (int1) from IRC.

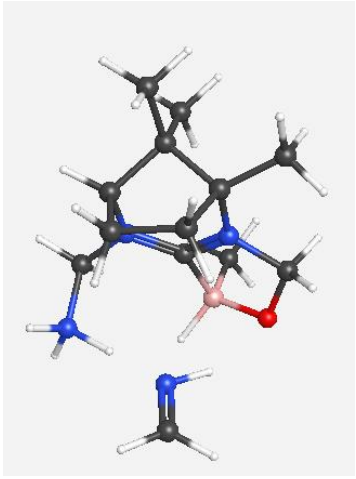

Figure 4.44 Optimized geometry of the reactant obtained from IRC.

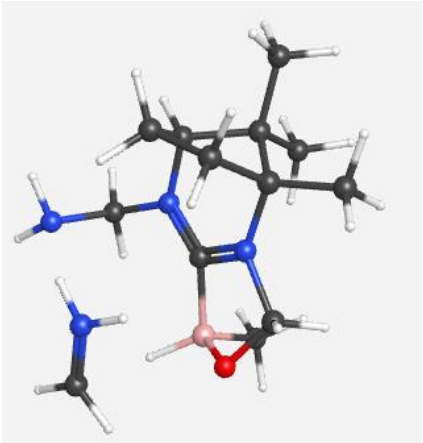

Figure 4.45 Optimized geometry of the intermediate (int1) from IRC.

In the next part the transition state was located which connected this intermediate with the product. The transition state obtained as a result had a single imaginary frequency. Optimized geometry of the TS is shown in Figure 4.46.

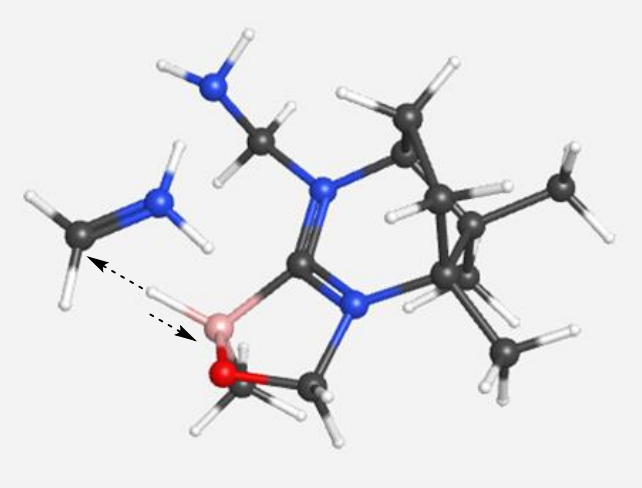

Figure 4.46 Optimized geometry of the transition state (TS2).

Again, IRC was done to ascertain that this transition state (TS2) connects to intermediate (Int1) on one side and products on the other. But it was seen that although this transition state (TS2) connected to Int1 on one side, but on the other side it connected to another intermediate (Int2). Int2 is the product attached with the catalyst. Optimized geometry of the Int2 is shown in Figure 4.47.

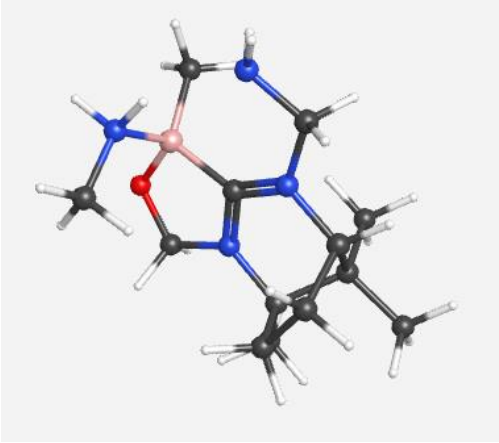

Figure 4.47 Optimized geometry of the intermediate (Int2).

Once again calculations were started to find the barrier between Int2 and product. The transition state (TS3) thus obtained also had only one imaginary frequency. The optimized geometry of the same is depicted in Figure 4.48.

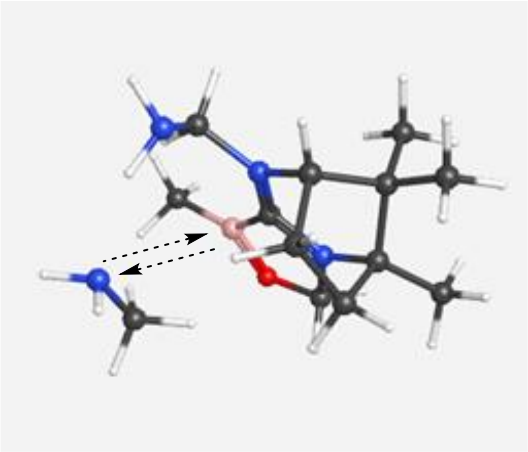

Figure 4.48 Optimized geometry of the transition state (TS3).

Final IRC calculation revealed that this transition state (TS3) connected to Int2 on one side and the product on the other. Thus, completing the catalytic cycle. Energetics of the whole transformation is depicted in Table 4.9 and depicted in Figure 4.49. Complete catalytic cycle for this transformation if given in Figure 4.50.

Substrate	Electronic E /Hartrees	$\Delta^{\ddagger}E$ /kJ mol^{-1}	$\Delta^{\ddagger}G$ /kJ mol^{-1}	ΔE /kJ mol^{-1}	ΔG /kJ mol^{-1}
Gas Phase					
Reactant	-830.7592682				
Product	-830.8144084			-145	-143
Intermediate (Int1)	-830.7683382			-24	-18
Intermediate (Int2)	-830.8620544			-270	-250
TS1	-830.75931	-0.11	0.15		
TS2	-830.7561878	32	35		
TS3	-830.8154005	122	110		
Toluene					
Reactant	-830.8192454				
Product	-830.8649035			-120	-118
Intermediate (Int1)	-830.8240557			-13	-7
Intermediate (Int2)	-830.9158234			-254	-234
TS1	-830.8193899	-0.38	-0.12		
TS2	-830.8128298	29	33		

Table 4.9 Energies of all the steps involved in hydrogenation of imines in gas phase.

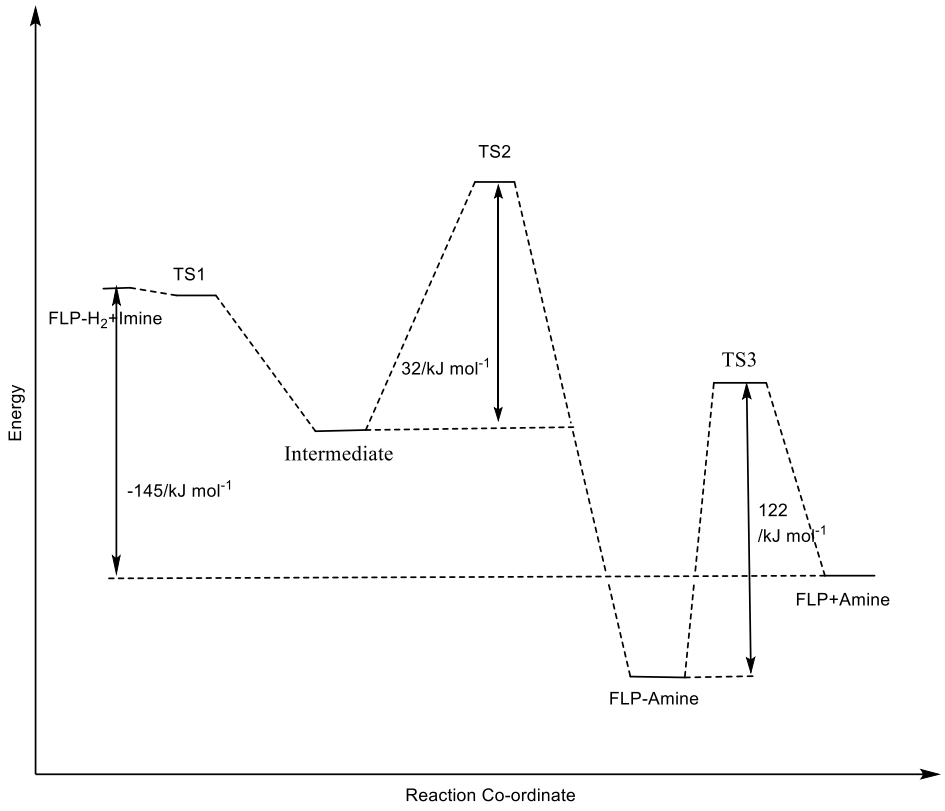

Figure 4.49 Energy profile diagram for hydrogenation of imines (Formaldimine).

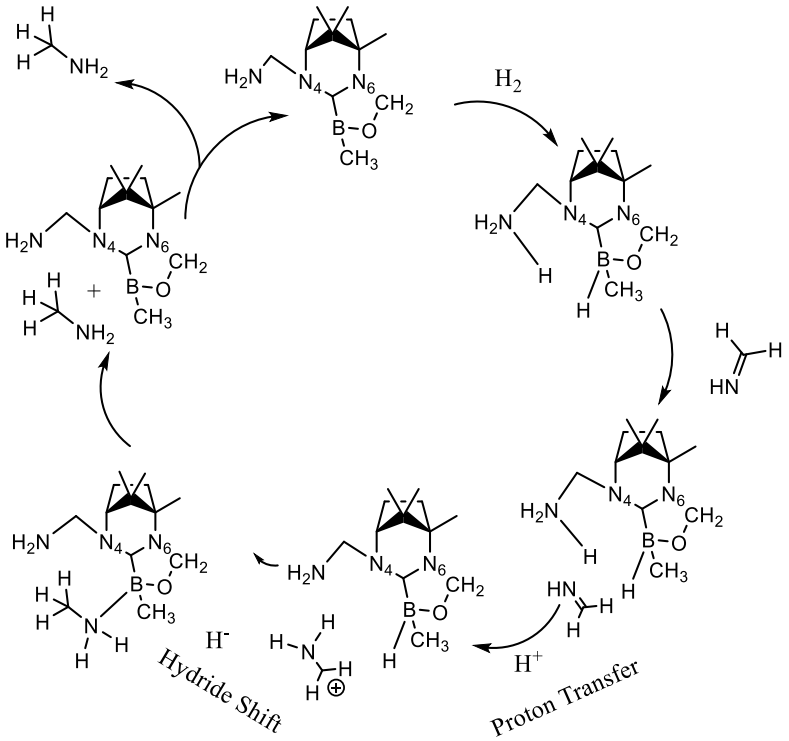

Figure 4.50 Complete catalytic cycle for hydrogenation of imines (Formaldimine).

4.5 Conclusions

In this chapter, hydrogenation of some simple achiral substrates as olefins, aldehydes, ketones and imines with the FLPs has been studied at length. The study revealed that the hydrogenation of ethene is concerted and synchronous. Hydrogenation of aldehydes and ketones is also concerted and synchronous, but we find that it is difficult to detach the product from the catalyst: the energy of the isolated product is more than the product attached with the catalyst. In contrast, hydrogenation of imines is step wise.

Barriers to hydrogenation are generally quite small, in the range of 30 to 80 kJ mol^{-1}, such that this process is expected to take place at room or slightly elevated

temperatures. Barriers are quite strongly dependent on the nature of the base and substituent on B within the FLP and also to the environment.

The activation barrier is lowered when the base is -PH_2 [**4a(iii)**/**4a(xix)**] instead of -NH_2 [**4a(i)**/**4a(xvii)**]. The barrier is raised when B is attached with C_6F_5 [**4a(xvii)**/**4a(xix)**] rather when it is attached with CH_3 [**4a(i)**/**4a(iii)**] in the solvent. It is observed that all the $\Delta G^{\ddagger}$ values are higher and the ΔG values less negative in solvent (Toluene) than in the gaseous phase.

All hydrogenation reactions are predicted to be highly exothermic/exoergic with overall energy changes of several hundred kJ mol^{-1}, again with significant dependence on substituents and solvent.

Chapter-5 Hydrogenation of Prochiral Substrates

In the last chapter hydrogenation of olefins and carbonyl compounds and some imines were discussed at length. In this chapter hydrogenation of some prochiral substrates will be analysed. An effort will be made to understand the stereochemical preferences in these transformations *i.e* the ability of one reactant to form mixture of stereoisomers with one in preference over other and also the regiochemical preferences *i.e* preference of the reactant for particular region of the substrate.

5.1 Hydrogenation of Acetophenone

As the pathway for hydrogenation of acetone had already been studied in Chapter 4, it was thought that the pathway for hydrogenation of acetophenone will also be somewhat similar. Figure 5.1 depicts the pathway envisaged.

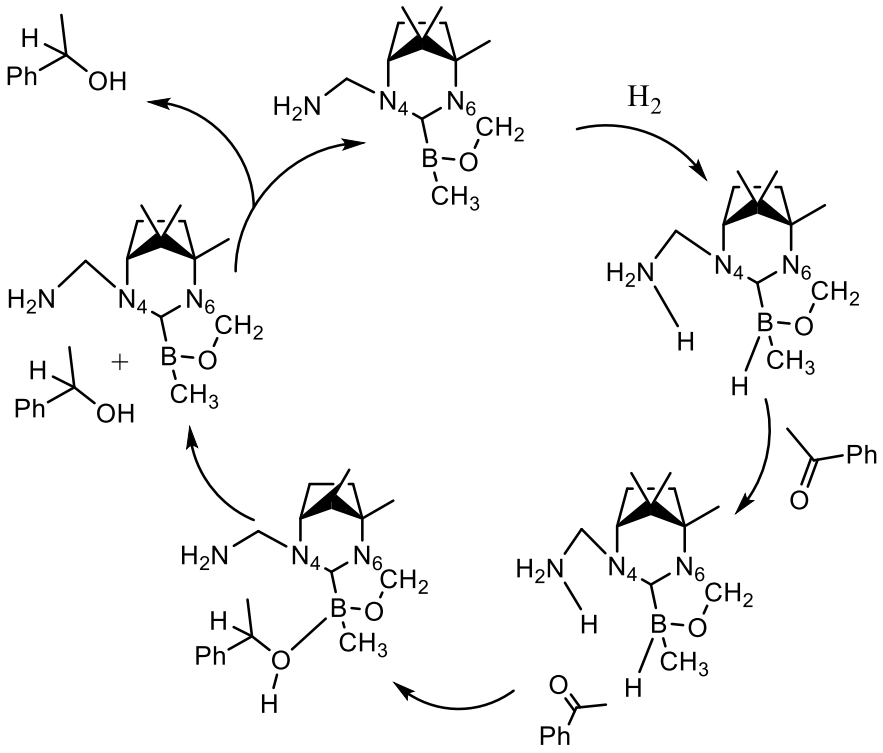

Figure 5.1 Plausible pathway for hydrogenation of acetophenone.

Although it is reasonable to presume that the pathway for hydrogenation of acetophenone should be similar to acetone, acetophenone is prochiral molecule and therefore it has two different faces (Re-face and Si-face) available for attack. Hence, it needs to be ascertained, how attack occurs at both faces? To understand the detailed mechanism at the outset some probable conformation for Re and Si face of acetophenone were optimized. Figure 5.2 represents the optimized geometries of Re and Si face conformations calculated on M062X/6-31G(d) level of theory.

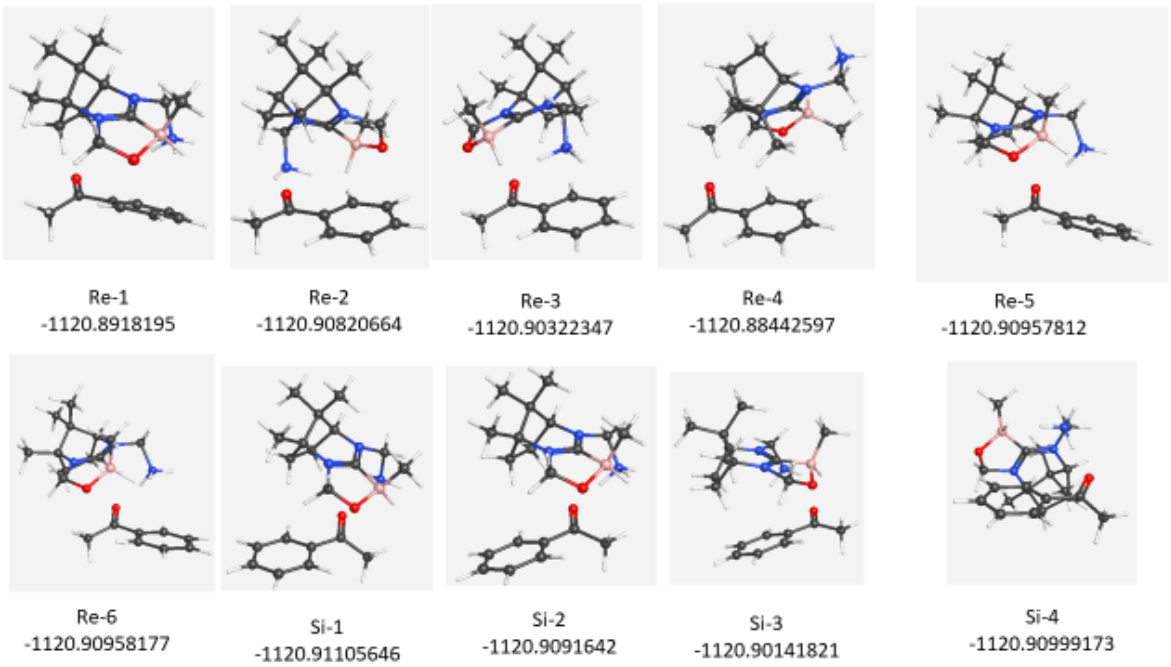

Figure 5.2 Optimized geometries of possible conformations of Re and Si face of acetophenone.

Once we had the optimized geometries and their corresponding energies, the next step was to study the complete path of hydrogenation via Re as well as Si face of

acetophenone. In the forthcoming sections the reaction pathway for hydrogenation through both Re and Si faces of acetophenone will be discussed at length.

5.1.1 Hydrogenation of acetophenone *via* Si-face

Reactant Si-1 was chosen to explore the pathway as it was the most stable conformer. As done in the last chapter, the study was initiated by running a scan of B-H….C44 distance (starting from H….C(44) distance 2.9 Å and then reducing it gradually). Figure 5.3 depicts the scan plot of the same.

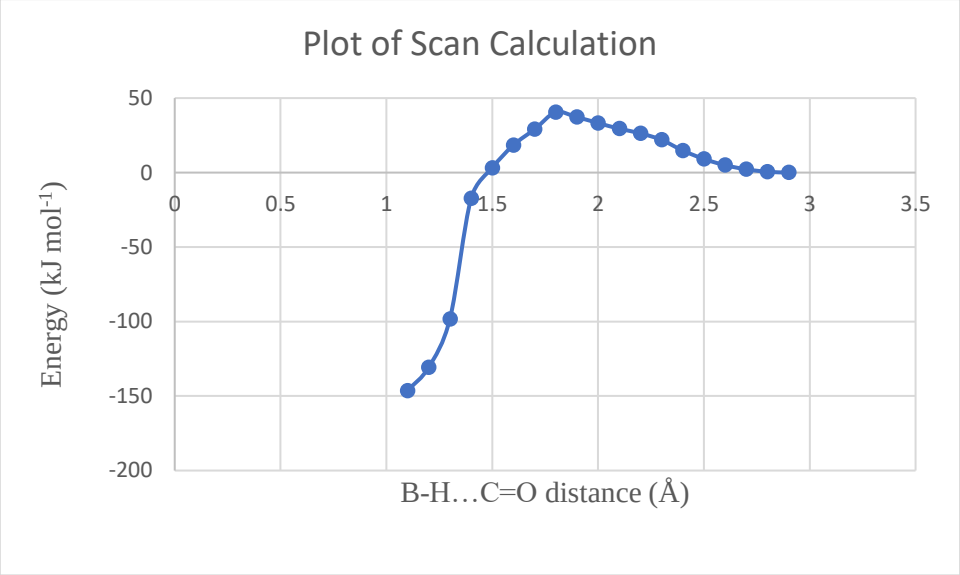

Figure 5.3 Scan plot of hydrogenation of acetophenone by Si-face.

Search for transition state connecting reactant and product was tried from various potential points from the scan plot. Transition state obtained as a result had only one negative frequency corresponding to hydrogen transfer. Figure 5.4 represents the optimized geometry of the transition state for Re face of acetophenone.

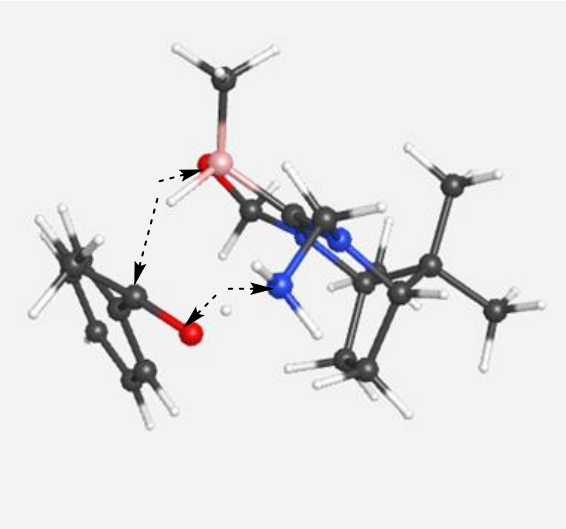

Figure 5.4 Optimized geometry for the initial Si- transition state.

IRC calculation was run to find if this TS connected the reactant and the product. It was found that the TS connected reactant on one end and an intermediate instead of product at the other end. Figure 5.5 depicts the IRC plot for the reaction.

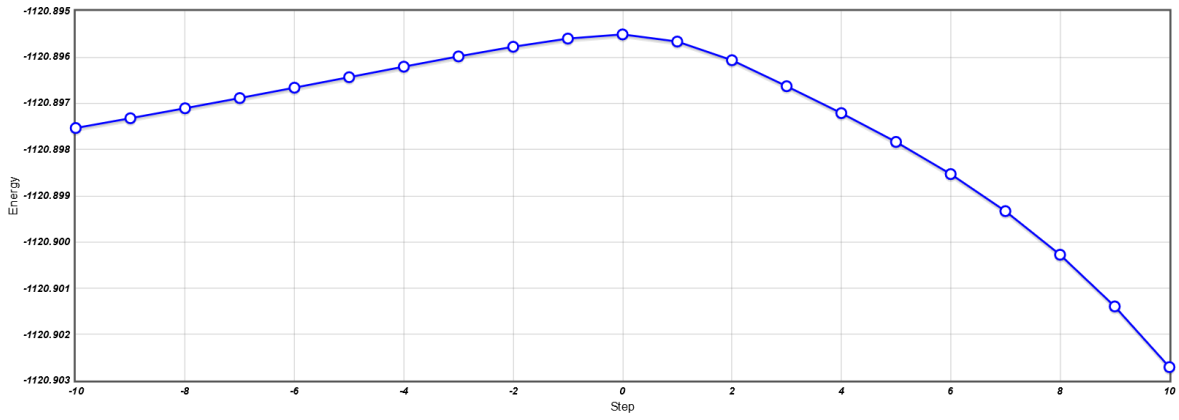

Figure 5.5 IRC plot for hydrogenation of acetophenone through its Si-face.

Start as well as end point of the IRC were optimized to get the true minimum at both the ends. Results revealed that one end of the IRC is the Si-face of acetophenone i.e. the reactant. Figure 5.6 displays the optimized geometry of the reactant. The energy of the geometry of the reactant optimized from the IRC is very similar to the starting Si-1 conformer. The difference between the two is -0.001 kJ mol^{-1}.

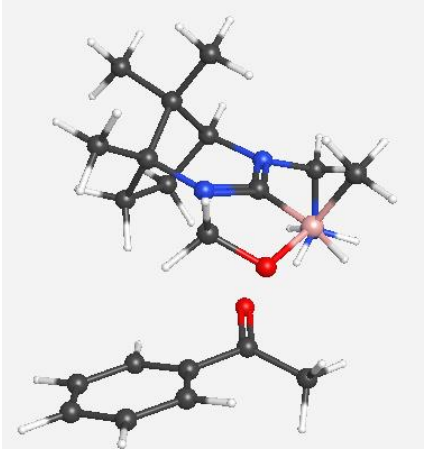

Figure 5.6 Optimized geometry of the Si-face of reactant from IRC.

The other end of the IRC was found to be an intermediate which was in fact product that was not separated from catalyst but bound to the Boron of FLP via oxygen. Exactly same behaviour was observed when hydrogenation was studied using acetone as a substrate (see section 4.3 of Chapter 4). B…O bond in this intermediate had 1.63 Å bond length. Figure 5.7 represents the optimized geometry of the intermediate.

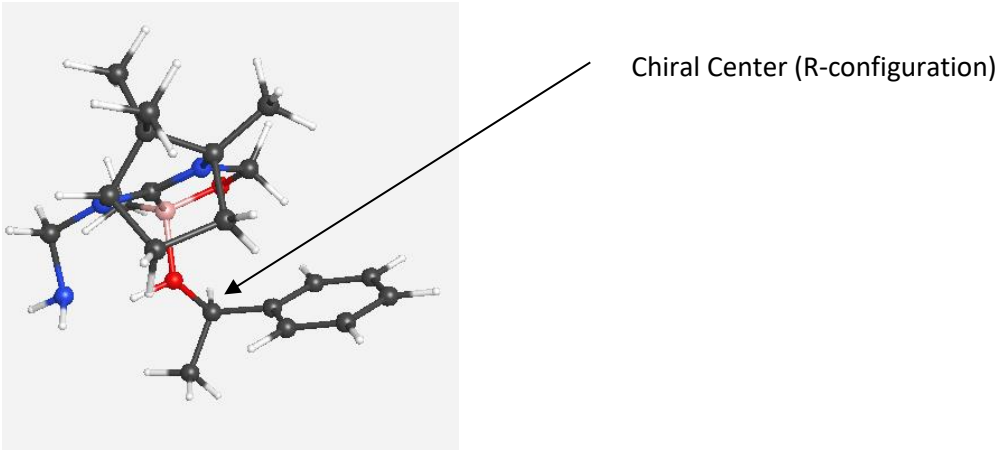

Figure 5.7 Optimized geometry of the intermediate (product attached with the catalyst) from IRC.

A glance at Figure shows that the newly formed chiral centre has R-configuration. Therefore, attack from Si-face of the reactant leads to the formation of R-product. After that, many attempts were done to check the energy required to separate the product from the catalyst but without any success. The reason for this may be attributed to the huge attraction of Lewis acid towards oxygen of the alcohol product. Energetics for the whole pathway is depicted in Table 5.1.

Substrate	**Electronic E /Hartrees**	***Δ‡E* /kJ mol^{-1}**	***Δ‡H* /kJ mol^{-1}**	***Δ‡G* /kJ mol^{-1}**	***ΔE* /kJ mol^{-1}**	***ΔH* /kJ mol^{-1}**	***ΔG* /kJ mol^{-1}**
Reactant	-1120.911057						
Product	-1120.966863				-147	-142	-140
TS	-1120.895628	41	26	33			

Table 5.1 Energetics for hydrogenation of Si-face of acetophenone.

Study of the reaction pathway reveals that analogous to the hydrogenation of acetone, hydrogenation of acetophenone through Si-face is also concerted but non-

synchronous reaction which becomes clear by having a glance at the bond lengths and bond orders of some key bonds participating in hydrogenation (Figure 5.8).

Figure 5.8 Bond lengths (bond orders) of some key bonds participating in hydrogenation of acetophenone through Si-face.

When this reaction was studied by taking Si-1 as a start point, at the same time the reaction pathway was also studied with Si-4. It was observed that Si-4 also proceeded *via* same TS as that for Si-1. When IRC calculation was done for this TS and the start and end points optimized as before, it was seen that gave same geometry for reactant and intermediate as in case of Si-1. We therefore conclude that exhaustive searching of reactant conformations is not required, since the process of coordinate scan, TS search, and IRC will find the correct pathway from any reasonable starting point.

5.1.2 Hydrogenation of acetophenone *via* Re-face

In the previous section all the steps involved in hydrogenation of acetophenone *via* Si-face were studied completely. In order to check if same or different pathway is followed

in attack via Re-face of acetophenone, reactant Re-6 was selected as it was found to be the most stable conformer after optimization. Calculations were carried out in the same order as reported in previous section. The study was initiated by running a scan of B-H….C44 distance (starting from H….C(44) distance 3.21 Å and then reducing it gradually). Figure 5.9 depicts the scan plot of the same.

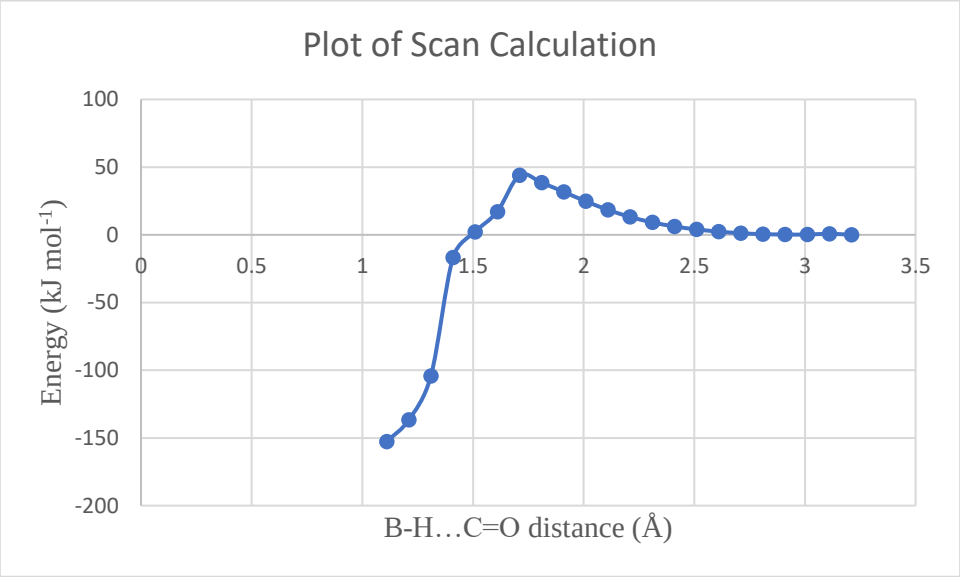

Figure 5.9 Scan plot of hydrogenation of acetophenone by Re-face.

Transition state search connecting reactant and product was tried from various potential points from the scan plot. Transition state obtained as a result had only one negative frequency. Figure 5.10 represents the optimized geometry of the transition state for Re face of acetophenone.

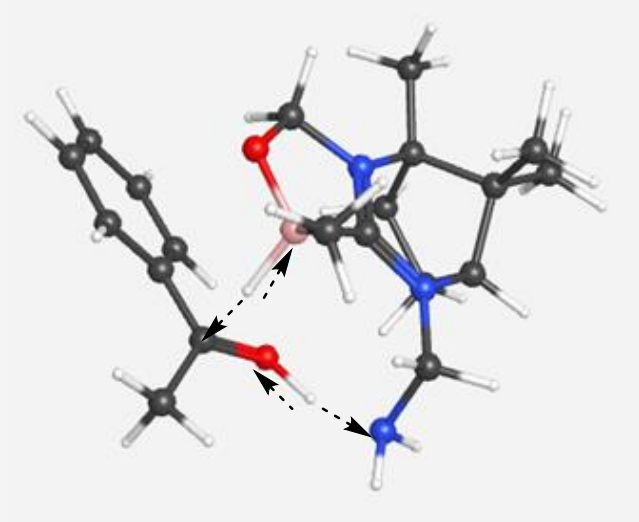

Figure 5.10 Optimized geometry for the transition state.

IRC calculation was run to find if this TS connected the reactant and the product. Figure 5.11 displays the IRC plot for the reaction.

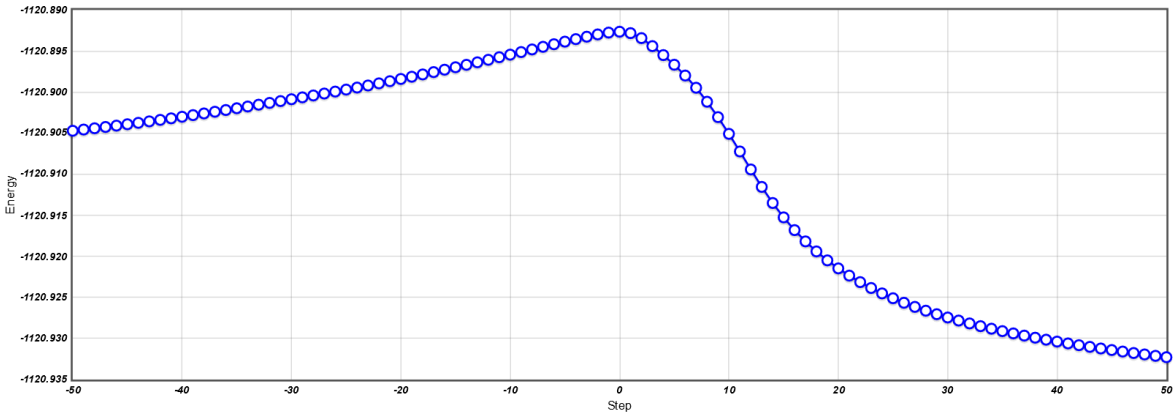

Figure 5.11 IRC plot for hydrogenation of acetophenone through its Re-face.

It was found that as in the case of Si-face, the TS connected reactant on one end and an intermediate (product attached with the reactant) instead of separated products at the other end. Figure 5.12 depicts the optimized geometry of reactant

(Re-face of acetophenone) from the IRC. As in the case of Si-face energy of the geometry of the reactant optimized from the IRC is very similar to the starting Re-6 conformer. The difference between the two is 0.172 kJ mol^{-1}.

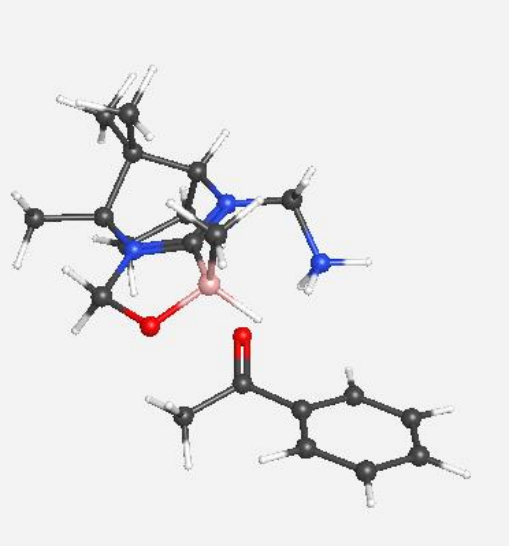

Figure 5.12 Optimized geometry of the Re-face of reactant from IRC.

The other end of the IRC which was the intermediate was in fact product that was not separated from catalyst but bound to the Boron of FLP via oxygen. B…O bond in this intermediate had 1.61 Å bond length. Figure 5.13 represents the optimized geometry of the intermediate.

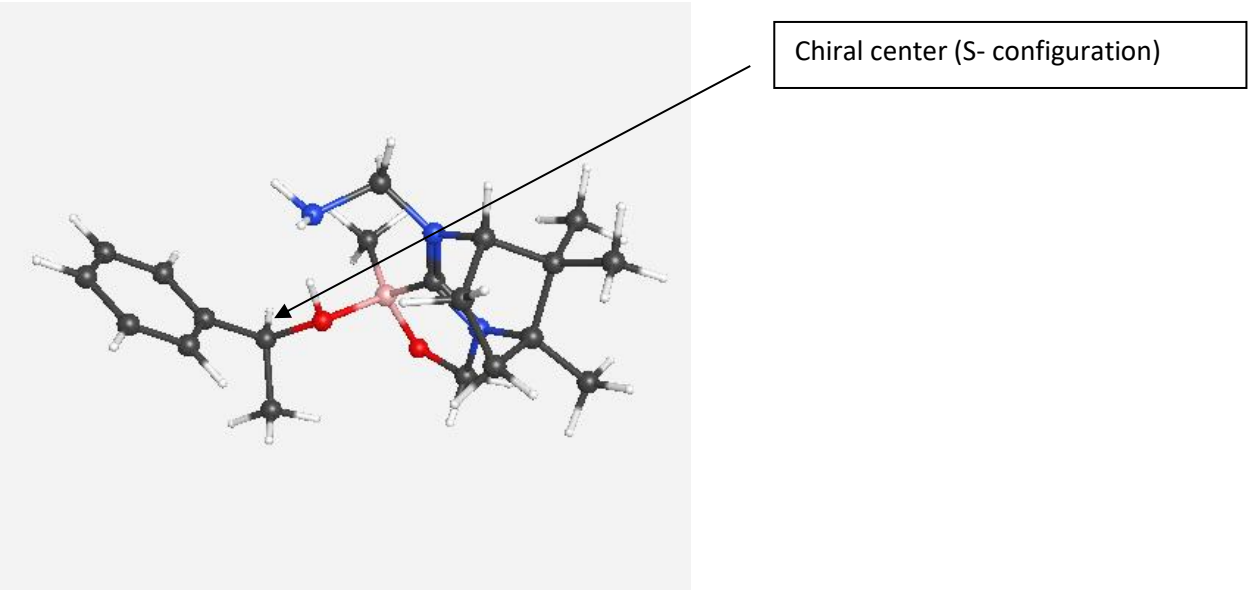

Figure 5.13 Optimized geometry of the intermediate from IRC.

A glance at Figure shows that the newly formed chiral centre has S-configuration. Therefore, attack from Re-face of the reactant leads to the formation of S-product. As in the previous section, many attempts were done to check the energy required to separate the product from the catalyst but without any success. The reason for this may be attributed to the huge attraction of Lewis acid towards oxygen of the product. Energetics for the whole pathway is depicted in Table 5.2.

Substrate	**Electronic E /Hartrees**	$\Delta^{\ddagger}E$ **/kJ mol^{-1}**	$\Delta^{\ddagger}H$ **/kJ mol^{-1}**	$\Delta^{\ddagger}G$ **/kJ mol^{-1}**	ΔE **/kJ mol^{-1}**	ΔH **/kJ mol^{-1}**	ΔG **/kJ mol^{-1}**
Reactant	-1120.909512						
Product	-1120.967825				-153	-147	-142
TS	-1120.892644	44	31	39			

Table 5.2 Energetics for hydrogenation of Re-face of acetophenone.

As in the previous section study of the reaction pathway reveals that analogous to the hydrogenation of acetone, hydrogenation of acetophenone through Re-face is also concerted but non-synchronous reaction which becomes clear by having a glance at the bond lengths (bond orders) of some key bonds participating in hydrogenation (Figure 5.14).

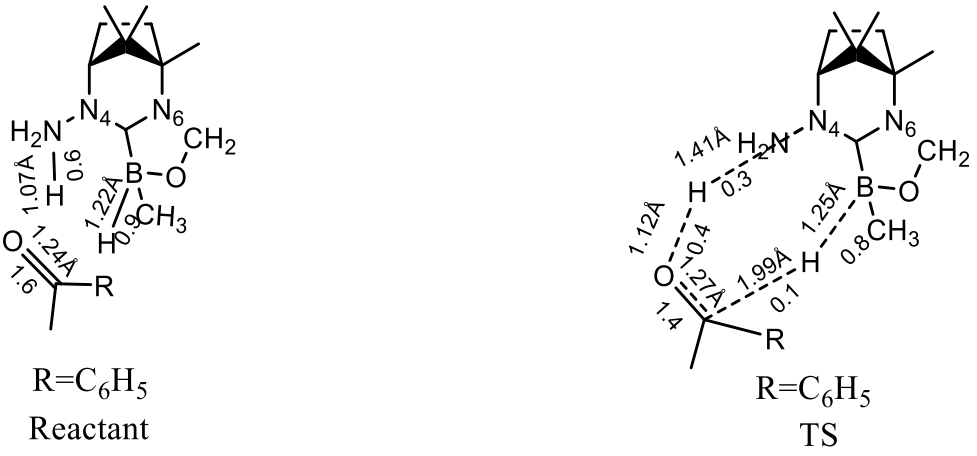

Figure 5.14 Bond lengths (bond orders) of some key bonds participating in hydrogenation of acetophenone through Si-face.

5.1.3 Comparison of Hydrogenation via Re- and Si-face of Acetophenone

Energy profile diagram in Figures 5.15 – 5.17 compares the overall energetics of the attack on both faces of acetophenone.

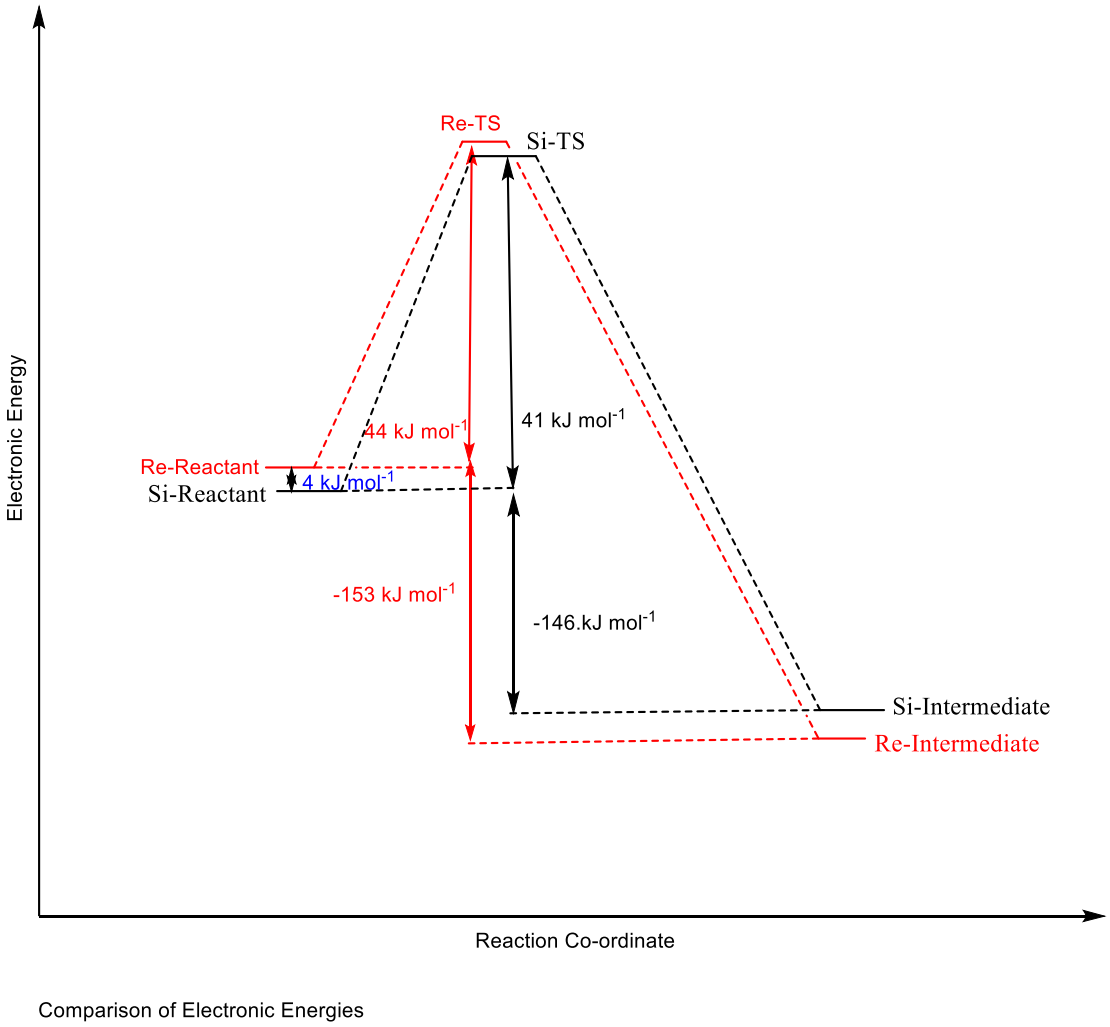

Figure 5.15 Comparison of electronic energy for attack of FLP on Re- and Si-face of acetophenone.

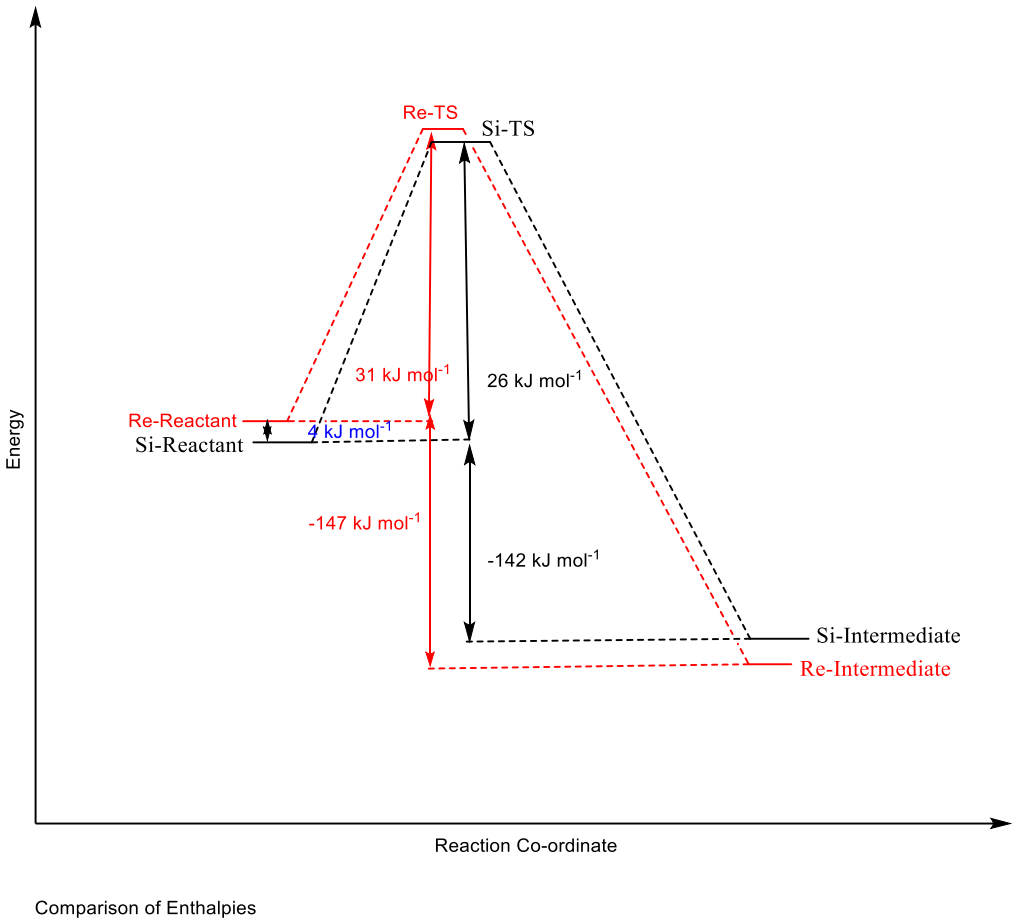

Figure 5.16 Comparison of enthalpy for attack of FLP on Re- and Si-face of acetophenone.

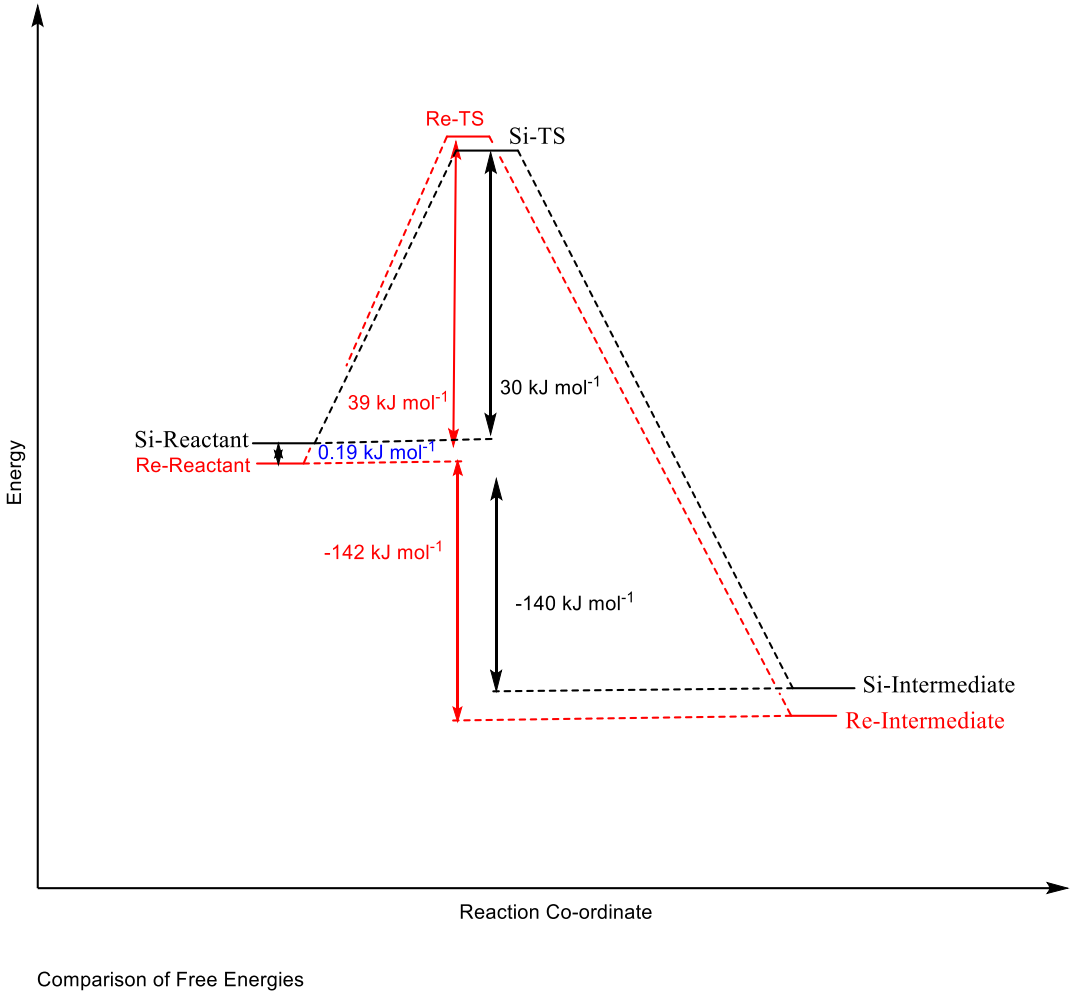

Figure 5.17 Comparison of free energy for attack of FLP on Re- and Si-face of acetophenone.

Comparison of energetics (Figure 5.15-5.17) of Re and Si face by studying electronic energy, enthalpy and free energy shows almost similar trends. One exception to this trend is that in the case of electronic energy and enthalpy, Si-reactant is more stable than the Re-reactant but in the case of free energy, Re-reactant becomes a bit more stable than Si-reactant. It may be noted that the barrier is affected by this change.

Table 5.3 presents the energetics of whole conversion in a concise way.

Substrate	**Electronic E /Hartrees**	***Δ‡E* /kJ mol^{-1}**	***Δ‡G* /kJ mol^{-1}**	***ΔE* /kJ mol^{-1}**	***ΔG* /kJ mol^{-1}**
Reactant-Si	-1120.911057				
Product-Si	-1120.966863			-147	-140
TS-Si	-1120.895608	41	30		
Reactant-Re	-1120.909512				
Product-Re	-1120.967825			-153	-142
TS-Re	-1120.892644	44	39		

Table 5.3 Energies of all the steps involved in hydrogenation of acetophenone.

After studying the complete pathway in gas phase single point calculations for all the steps were done in the presence of solvent (toluene) also to study its effect. Table 5.4 depicts the results of calculations done.

Substrate	**Electronic E /Hartrees**	***Δ‡E* /kJ mol^{-1}**	***Δ‡G* /kJ mol^{-1}**	***ΔE* /kJ mol^{-1}**	***ΔG* /kJ mol^{-1}**
Reactant-Si	-1120.974293				
Product-Si	-1121.023766			-130	
TS-Si	-1120.955846	48	38		
Reactant-Re	-1120.971492				
Product-Re	-1121.026011			-143	
TS-Re	-1120.952867	49	43		

Table 5.4 Energies of all the steps involved in hydrogenation of acetophenone in solvent (toluene).

A close look at Table 5.4 reveals that although the *Δ‡E* values for Re and Si face are almost similar, *Δ‡G* values are quite different. Apart from comparing the energetics, enantiomeric excess was also calculated. To begin with the energy difference between

two transition states (for Re and Si face respectively) was calculated and then enantiomeric excess was calculated at various temperatures. The plot of ee against temperature is depicted in Figure 5.18.

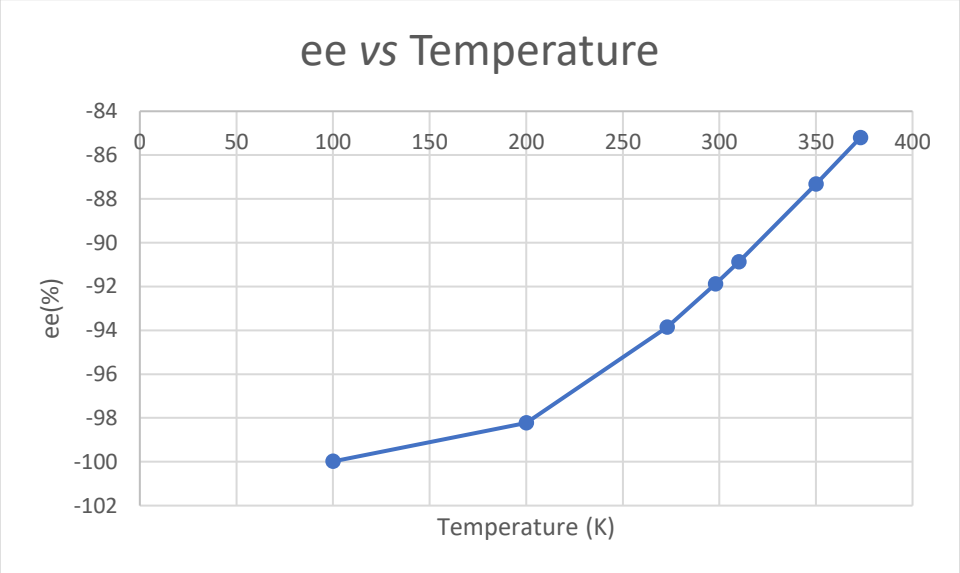

Figure 5.18 Plot of enantiomeric excess (ee) *vs* temperature (K).

It has been observed that in general acetone hydrogenations with FLPs take place with 60.8 bar hydrogen at 70°C[1] while hydrogenation acetophenone with FLPs take place with 100 bar hydrogen at 75°C[2]. The plot in Figure 5.18 predicts the enantiomeric excess at 298K to be 92%.

5.1.4 Further Analysis

It was thought worthwhile to check the non-covalent interactions between catalyst and substrate to understand the preference for Si-face attack. It was done by constructing NCI (Non-Covalent Interaction) plots that give an idea about inter- and intramolecular

non-covalent interactions in the system. Figure 5.19 represents the NCI plots for hydrogenation via Re/Si face of acetophenone in presence of FLP. NCI Plot indicates differences between transition states, most notably in the interactions of the aromatic ring of the substrate.

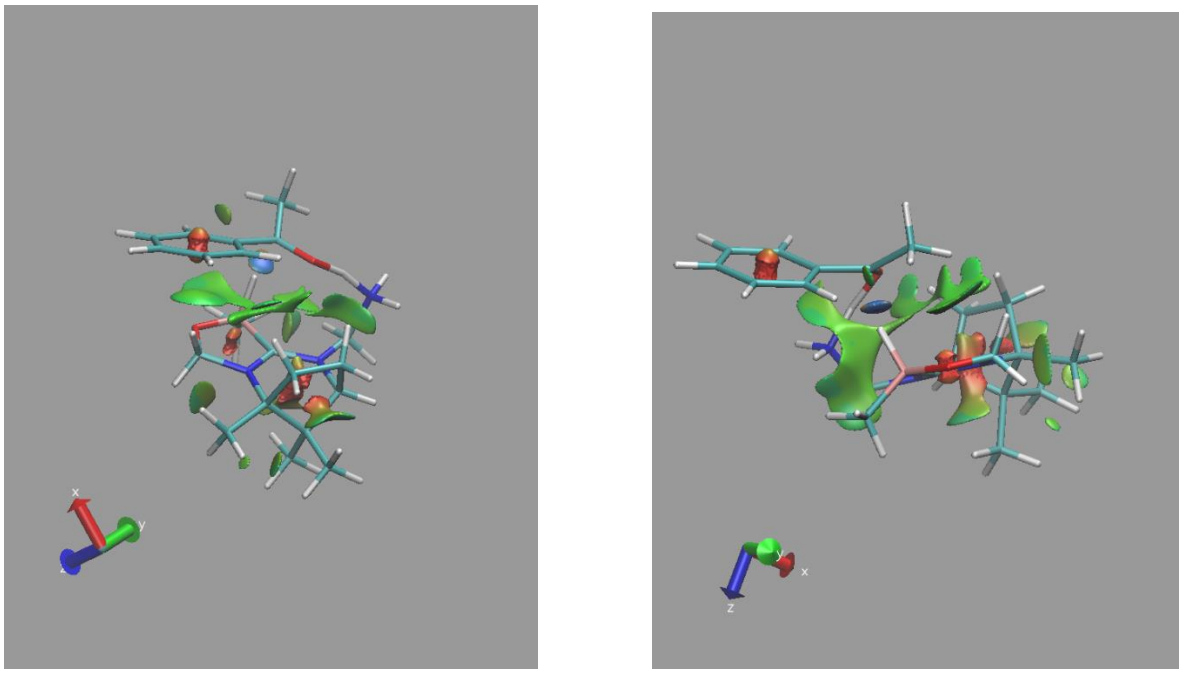

Figure 5.19 NCI plot for TS *via* Re/Si face of acetophenone in presence of FLP.

Although it is very difficult to exactly locate attractive and repulsive interactions in huge substrate-FLP system as shown in Figure 5.19, but an effort was made to catalogue distances between selected groups in Si- and Re-TS (Table 5.6) that come very close in TS. A careful look at Table 5.6 reveals few interesting facts. In Si-TS, C=O (2.45 Å), C(49) of aromatic ring (2.49 Å) and CH_3 (2.32 Å) group of substrate comes quite close to H attached to B in FLP. In the case of Re-TS, CH_3 of substrate comes very close to the H attached to the C between N and O in FLP (2.30 Å). Similarly, H attached to B in FLP comes quite close to CH_3 (2.38 Å) group and C(49) of the aromatic ring of substrate (2.32 Å).

Si-TS	**Distance /Å**
C(49)(aromatic ring of substrate)-O(22)(of FLP)	3.28
H(30)(attached to C between N and O of FLP)-C(50)(aromatic ring of substrate).	2.96
H(28)(H attached to B in FLP)-C(45) (CH_3 of substrate)	2.32
H(28) (H attached with B in FLP)-C(49) (C of aromatic ring in substrate)	2.49
H(48)(CH_3 of substrate)-H(25)(CH_3 of FLP)	3.62
H(28) (H attached to B in FLP)-O(43) (C=0 oxygen of substrate)	2.45
Re-TS	
C(49) (C of aromatic ring in substrate)-H(33) (H of NH_2 group in FLP)	3.16
C(50) (C of aromatic ring in substrate)-H(33) (H of NH_2 group in FLP)	2.98
H(28) (H attached to B in FLP)-C(49) (C of aromatic ring in substrate)	2.32
H(59) (H of aromatic ring in substrate)-H(34) (H of NH_2 group in FLP)	2.98
H(28) (H attached to B in FLP)-C(45) (CH_3 in substrate)	2.38
H(47) (CH_3 in substrate)-O(22)(in FLP)	2.99
H(48) (CH_3 in substrate)-H(30) (attached to C between N and O in FLP)	2.30

Table 5.6 Distance between selected groups in Si- and Re-TS.

5.2 Hydrogenation of (E)-α-Methyl-4-methoxystilbene

In the last section, hydrogenation of prochiral substrates was studied using prochiral carbonyl substrates. After studying the complete mechanism, it was thought worthwhile to study hydrogenation using one prochiral olefin substrate also. The substrate chosen for this study was (E)-α-Methyl-4-methoxystilbene. Steps employed to study this mechanism were exactly similar as in the last chapter. In the present study although different possible isomers have been optimized but one with the lowest energy were selected as the previous study (last section) has indicated that the reaction always proceeds through the same pathway immaterial of the starting point.

As the mechanism for hydrogenation of olefins have been studied in detail in Chapter 4, it was thought that hydrogenation of (E)-α-Methyl-4-methoxystilbene will also follow a similar pathway (Figure 5.20).

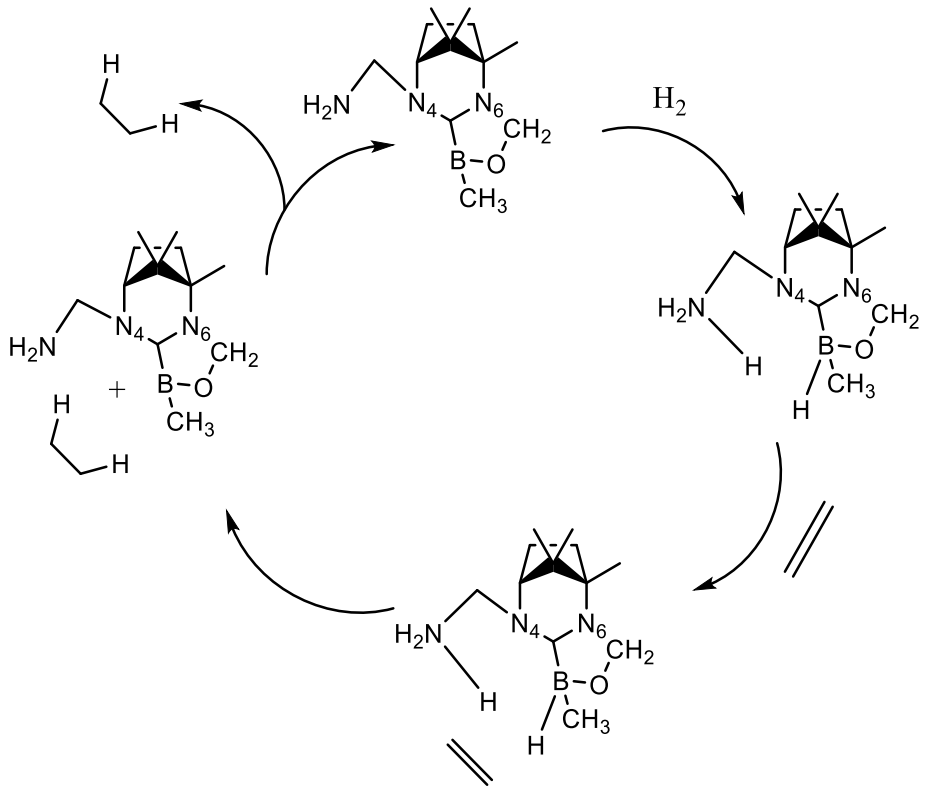

Figure 5.20 Plausible pathway for hydrogenation of (E)-α-Methyl-4-methoxystilbene.

5.2.1 Hydrogenation of (E)-α-Methyl-4-methoxystilbene *via* Re-face

The study was initiated by optimizing various probable isomers for Re-face of (E)-α-Methyl-4-methoxystilbene. Out of them the most stable one (Figure 5.21) was selected as the starting point.

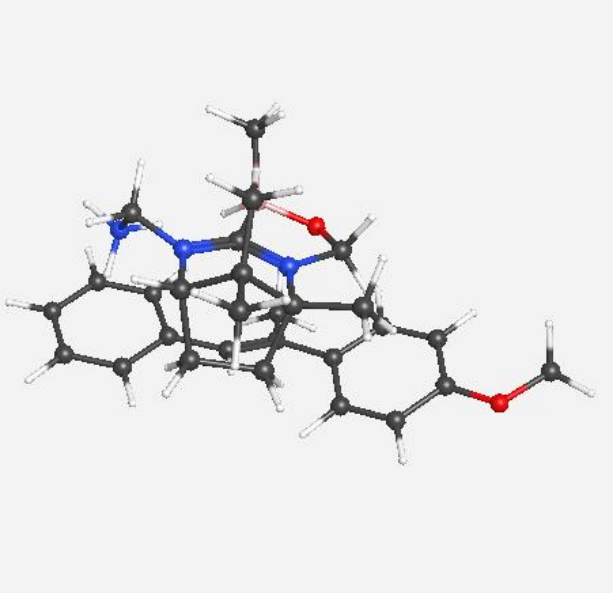

Figure 5.21 Optimized geometry of most stable Re-face conformer of (E)-α-Methyl-4-methoxystilbene).

Subsequently a scan of N-H…C=C distance (starting from H (9)…C (43) distance 3.3 Å and then reducing it gradually). Figure 5.22 depicts the scan plot of the same.

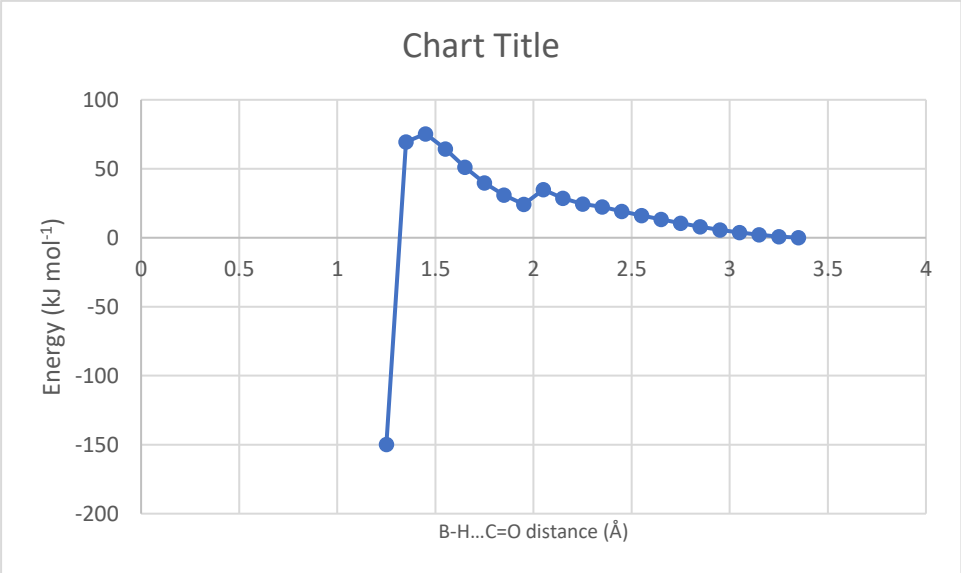

Figure 5.22 Scan plot of hydrogenation of (E)-α-Methyl-4-methoxystilbene) by Re-face.

Transition state connecting reactant and product was tried from various potential points from the scan plot. Transition state obtained as a result had only one negative frequency. Figure 5.23 represents the optimized geometry of the transition state for Re face of (E)-α-Methyl-4-methoxystilbene).

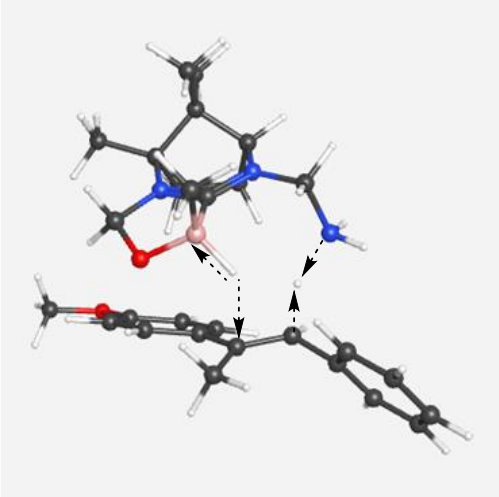

Figure 5.23 Optimized geometry for the transition state.

IRC calculation was done to find if this TS connected the reactant and the product. It was found that the TS connected reactant on one end and product at the other end. Figure 5.24 depicts the IRC plot for the reaction.

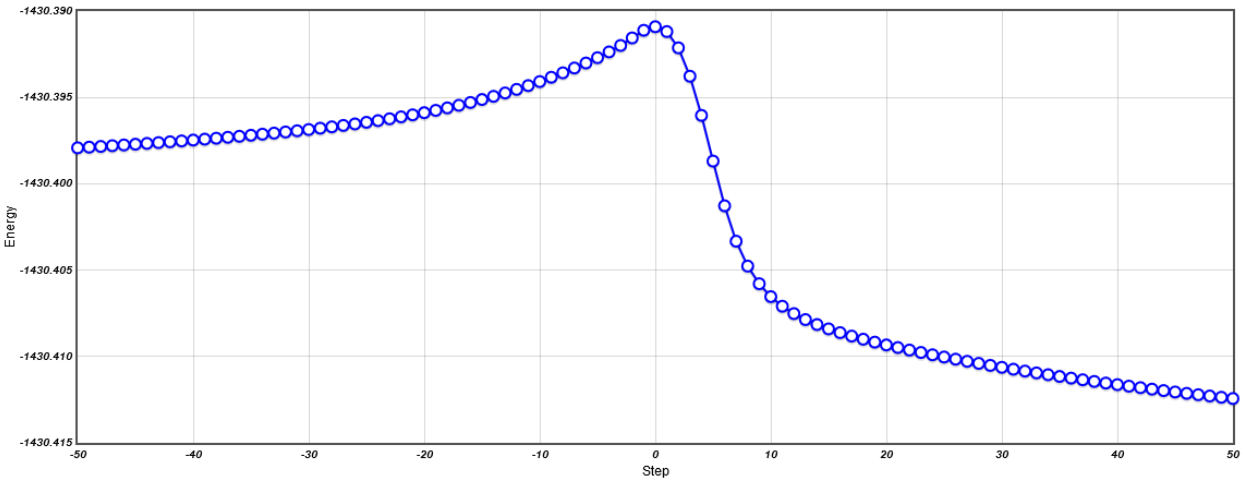

Figure 5.24 IRC plot for hydrogenation of (E)-α-Methyl-4-methoxystilbene) through its Re-face.

Start and end point of the IRC were optimized to get the true minimum at both the ends. Results revealed that one end of the IRC is the Re-face of (E)-α-Methyl-4-methoxystilbene) i.e. the reactant. Figure 5.25 displays the optimized geometry of the reactant. The energy of the geometry of the reactant optimized from the IRC is very similar to the starting probable Re-face conformer. The difference between the two is 4.35 kJ mol^{-1}.

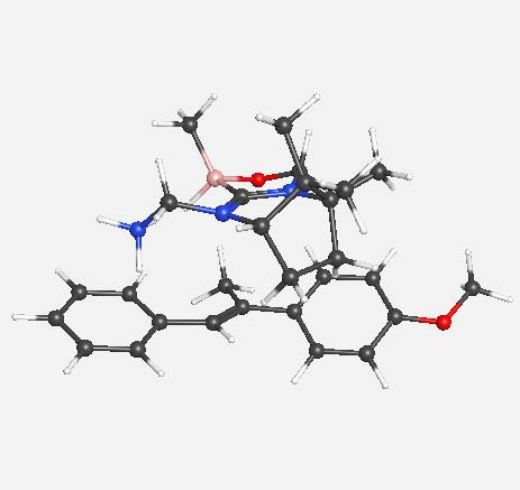

Figure 5.25 Optimized geometry of the Re-face of reactant from IRC.

The other end of the IRC was found to be the product. Figure 5.26 represents the optimized geometry of the product.

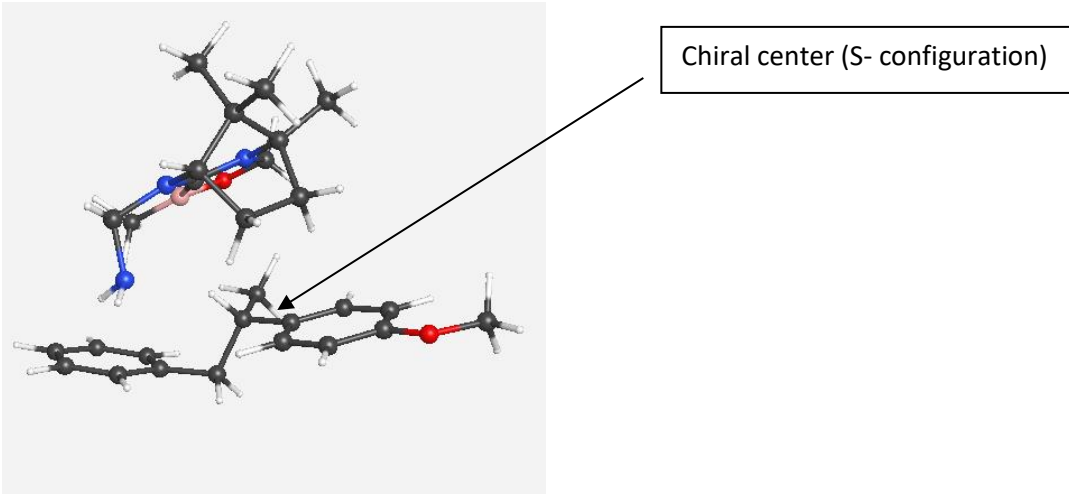

Figure 5.26 Optimized geometry of the intermediate (product attached with the catalyst) from IRC.

A glance at Figure shows that the newly formed chiral center has S-configuration. Therefore, attack from Re-face of the reactant leads to the formation of S-product. Energetics for the whole pathway is depicted in Table 5.5.

Substrate	**Electronic E /Hartrees**	***Δ‡E* /kJ mol^{-1}**	***Δ‡H* /kJ mol^{-1}**	***Δ‡G* /kJ mol^{-1}**	***ΔE* /kJ mol^{-1}**	***ΔH* /kJ mol^{-1}**	***ΔG* /kJ mol^{-1}**
Reactant	-1430.418437				-154	-149	-149
Product	-1430.477072						
TS	-1430.390905	72	55	62			

Table 5.5 Energetics for hydrogenation of Re-face of (E)-α-Methyl-4-methoxy stilbene).

5.2.2 Hydrogenation of (E)-α-Methyl-4-methoxystilbene *via* Si-face

In the previous section all the steps involved in hydrogenation of acetophenone *via* Re-face were studied completely. The same steps were repeated as in the previous section to check if the same pathway is followed in attack via Si-face of (E)-α-Methyl-

4-methoxystilbene). Figure 5.27 depicts the optimized geometry of the most stable Si-isomer.

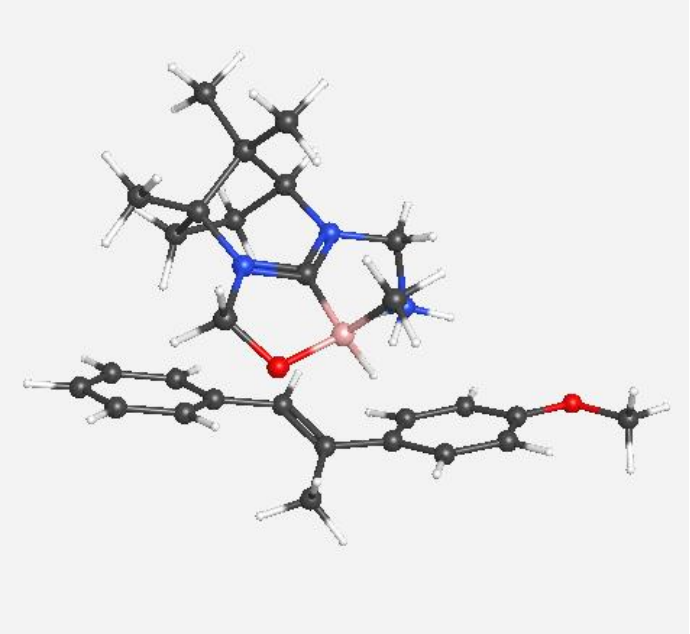

Figure 5.27 Optimized geometry of most stable Si-face conformer of (E)-α-Methyl-4-methoxystilbene).

The study was initiated by running a scan of B-H….C=C distance (starting from H….C (43) distance 2.95 Å and then reducing it gradually).

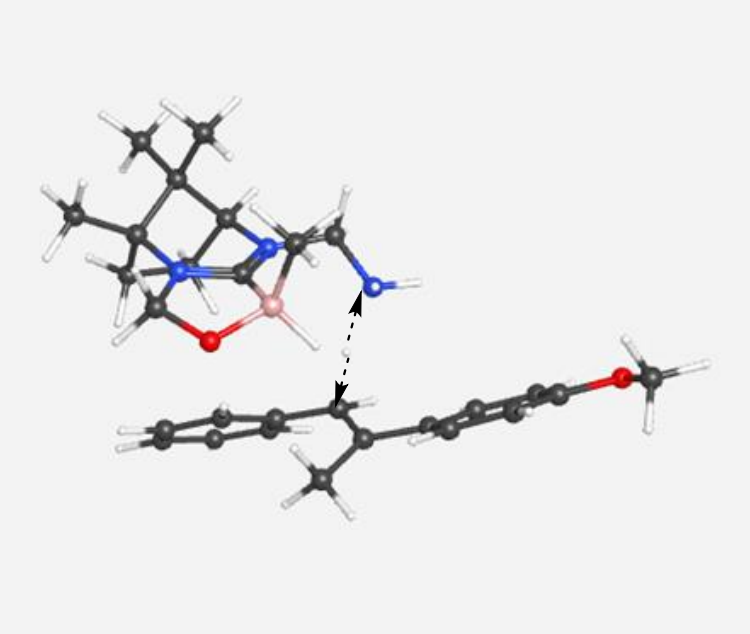

Figure 5.28 Optimized geometry for the transition state.

IRC calculation was run to find if this TS connected the reactant and the product. Figure 5.29 displays the IRC plot for the reaction.

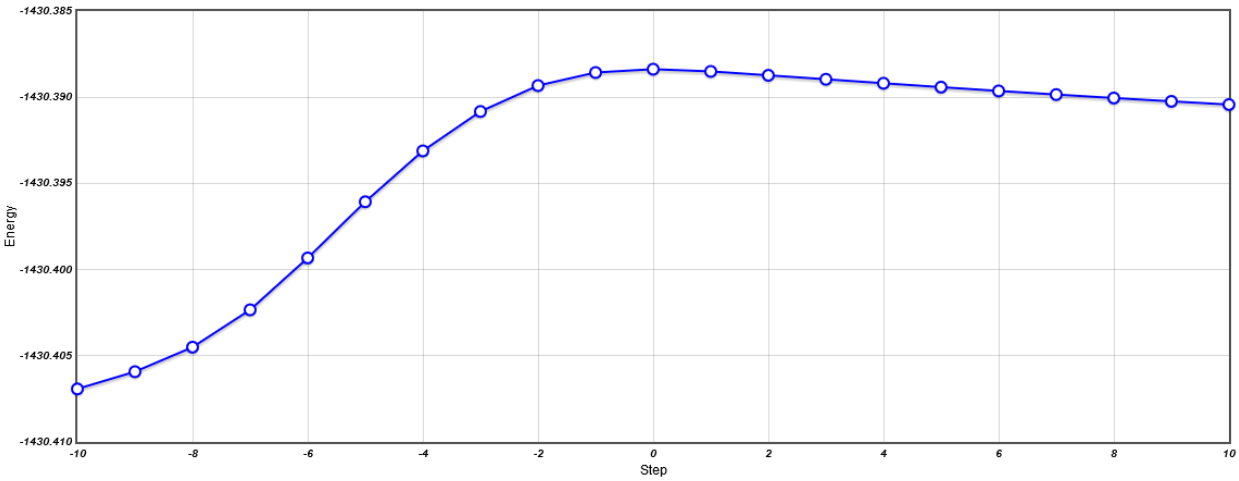

Figure 5.29 IRC plot for hydrogenation of (E)-α-Methyl-4-methoxystilbene) through its Si-face.

It was found that contrary to the previous case the TS connected reactant on one end and an intermediate on the other end. Figure 5.30 depicts the optimized geometry of

reactant (Si-face of (E)-α-Methyl-4-methoxystilbene) from the IRC. Energy of the geometry of the reactant optimized from the IRC is very similar to the starting Si-conformer. The difference between the two 0.000866 kJ mol^{-1}.

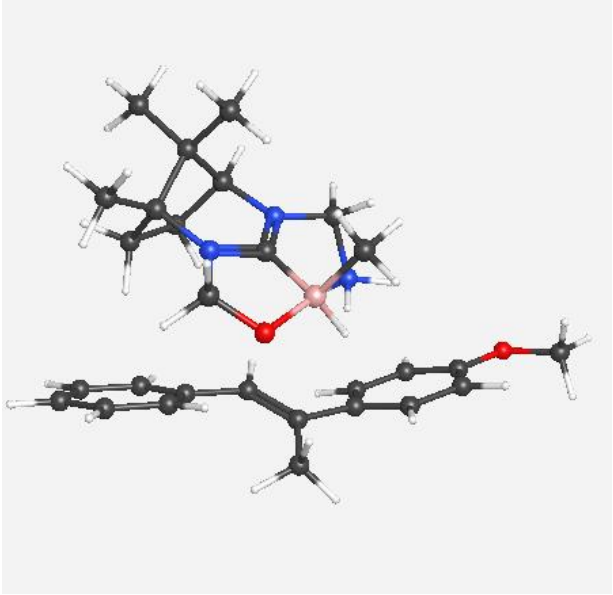

Figure 5.30 Optimized geometry of the Si-face of reactant from IRC.

The other end of the IRC which was the intermediate in which the hydrogen attached with nitrogen in FLP had migrated to olefin, but the hydrogen attached with the boron had not migrated yet. Figure 5.31 represents the optimized geometry of the intermediate.

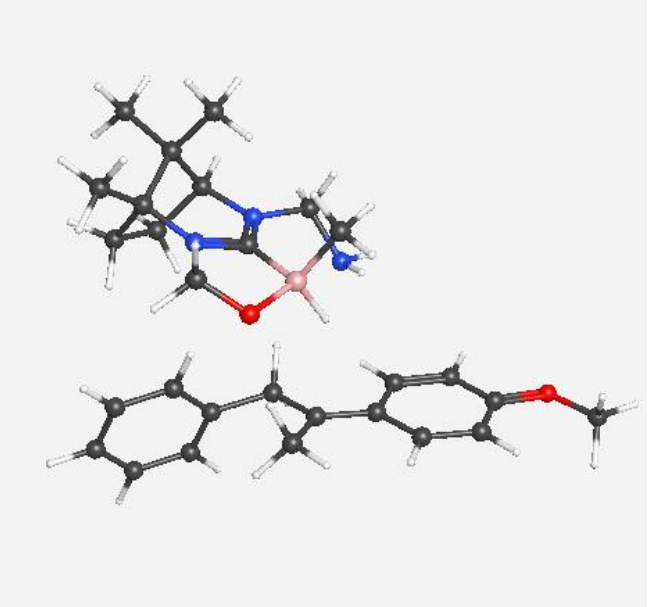

Figure 5.31 Optimized geometry of the intermediate from IRC.

In the next part scan (from intermediate) was done of B-H…C=C distance (starting from H (36)….C (43) distance 2.48 Å and then reducing it gradually). Transition state search connecting intermediate and product was tried from various potential points from the scan plot. Transition state obtained as a result had only one imaginary frequency (-92.267i cm^{-1}). Figure 5.32 represents the optimized geometry of the second transition state for Si face of (E)-α-Methyl-4-methoxystilbene).

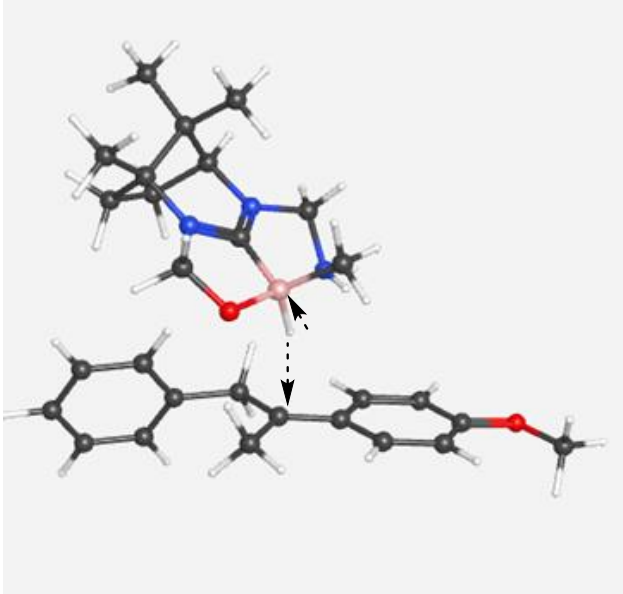

Figure 5.32 Optimized geometry of the second transition state connecting intermediate with the product.

IRC calculation was run to find if this TS connected the intermediate and the product.

Figure 5.33 displays the IRC plot for the reaction.

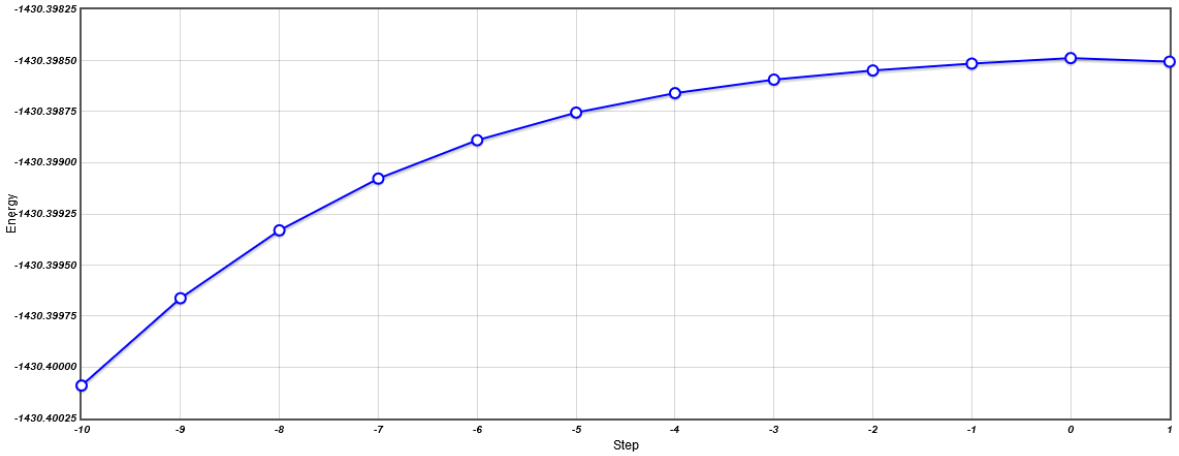

Figure 5.33 IRC plot for hydrogenation of intermediate involved in hydrogenation of (E)-α-Methyl-4-methoxystilbene) through its Si-face.

It was found that the TS connected intermediate on one end and the product on the other end. Figure 5.34 depicts the optimized geometry of the product from the IRC.

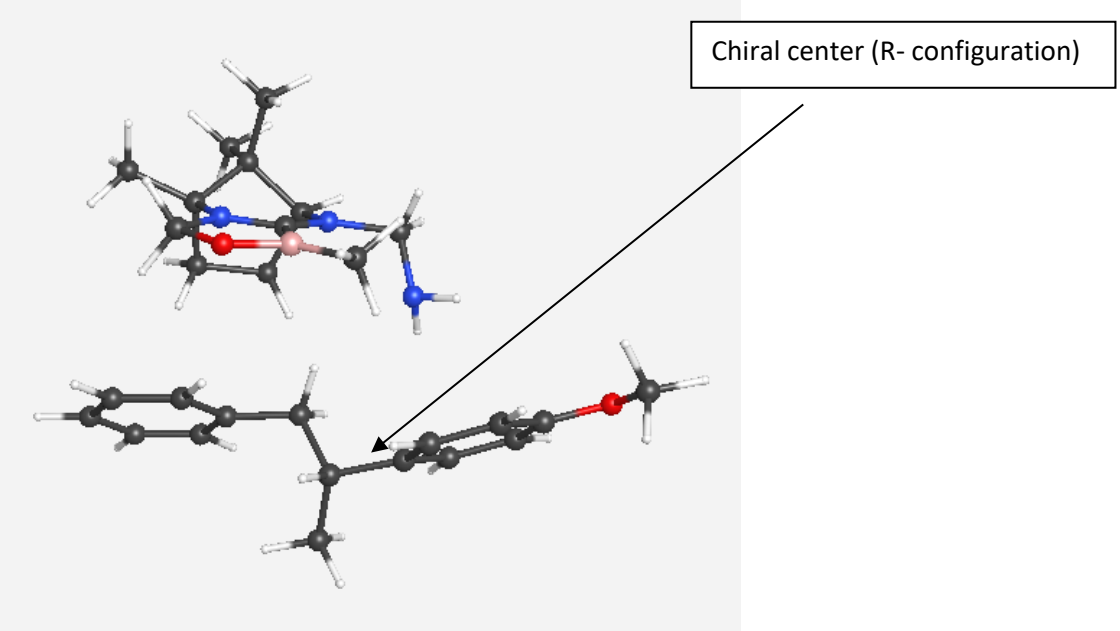

Figure 5.34 Optimized geometry of the product from IRC.

It was observed that the newly formed chiral center in the product has R-configuration. Therefore, attack from Si-face of the reactant leads to the formation of R-product. Energetics for the whole pathway is depicted in Table 5.6.

Substrate	**Electronic E /Hartrees**	***Δ‡E* /kJ mol^{-1}**	***Δ‡H* /kJ mol^{-1}**	***Δ‡G* /kJ mol^{-1}**	***ΔE* /kJ mol^{-1}**	***ΔH* /kJ mol^{-1}**	***ΔG* /kJ mol^{-1}**
Reactant	-1430.422043				-153	-148	-158
Intermediate	-1430.399592				59	56	44
TS1	-1430.388471	88	72	73			
TS2	-1430.398757	2	-1.79	5			
Product	-1430.480388						

Table 5.6 Energetics for hydrogenation of Si-face of (E)-α-Methyl-4-methoxy stilbene).

5.2.3 Comparison of Hydrogenation via Re- and Si-face of (E)-α-Methyl-4-methoxystilbene)

Energy profile diagram in Figures 5.32 – 5.34 compares the overall energetics of the attack on both faces of (E)-α-Methyl-4-methoxystilbene).

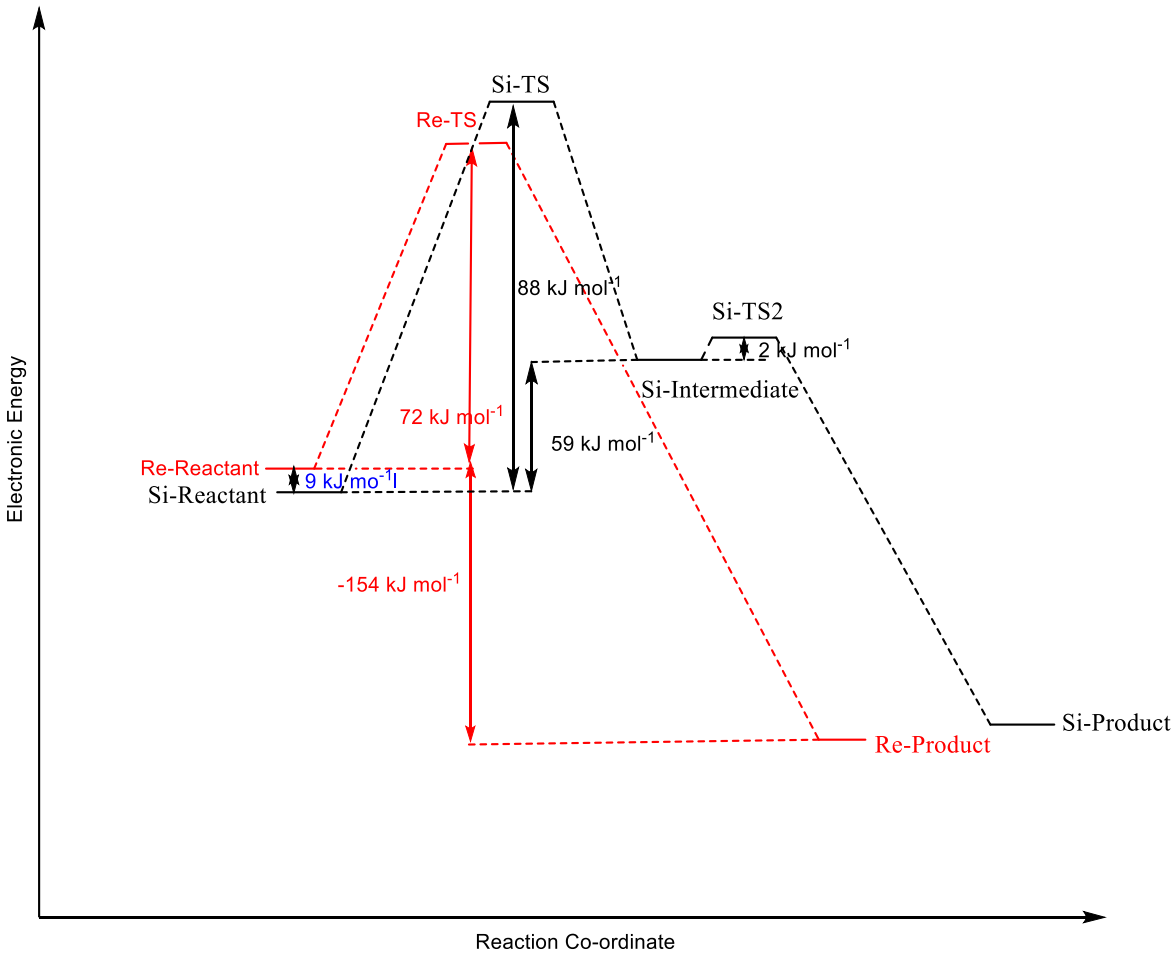

Comparison of Electronic Energies

Figure 5.32 Comparison of electronic energy for attack of FLP on Re- and Si-face of (E)-α-Methyl-4-methoxystilbene).

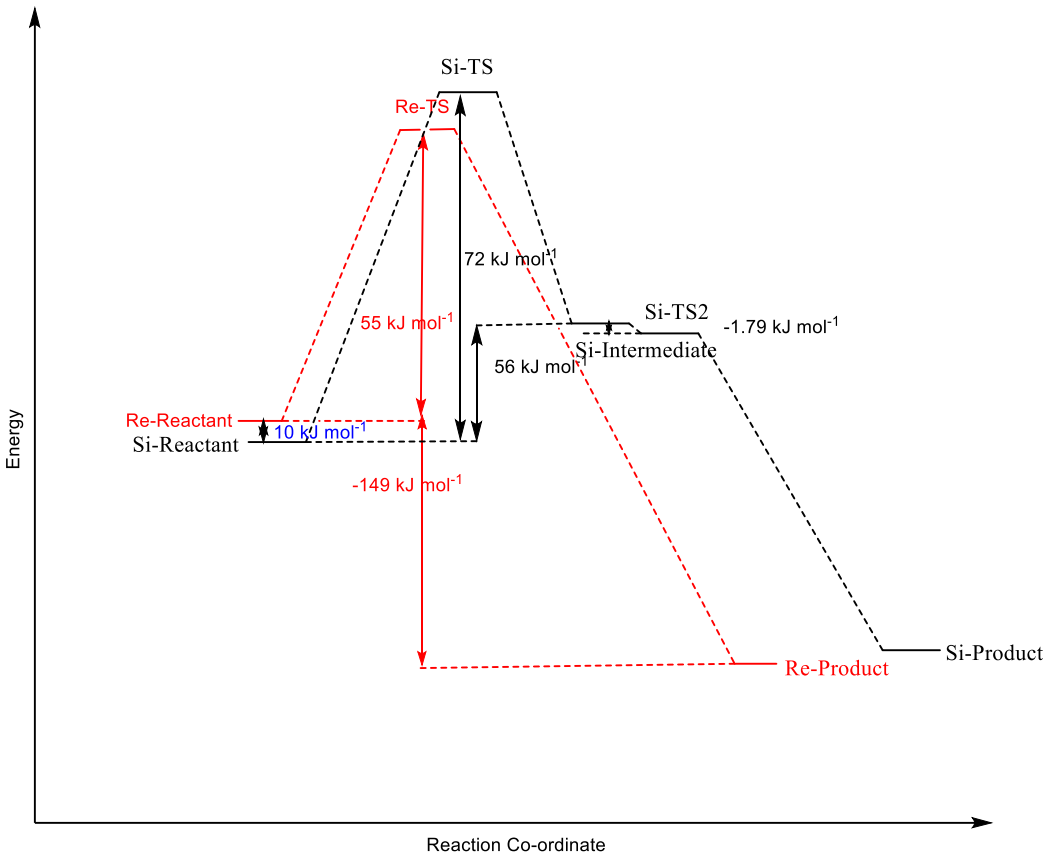

Figure 5.33 Comparison of enthalpy for attack of FLP on Re- and Si-face of (E)-α-Methyl-4-methoxystilbene).

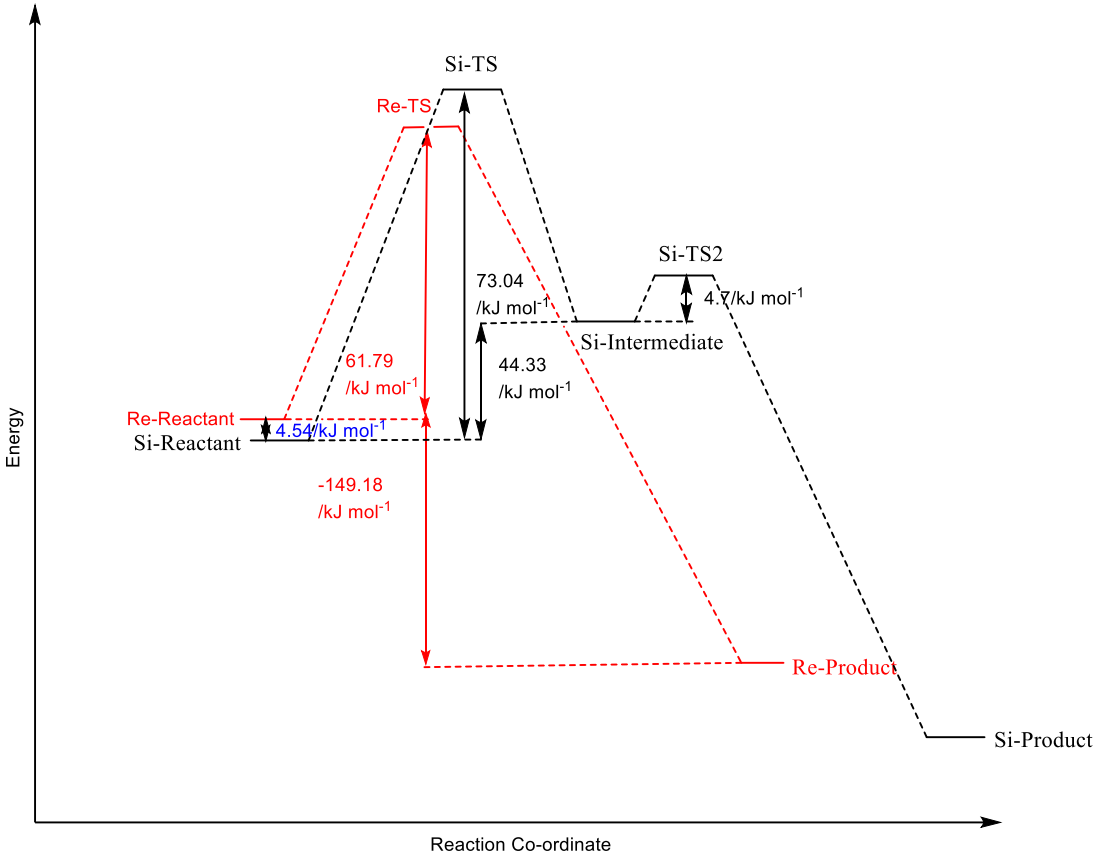

Figure 5.34 Comparison of free energy for attack of FLP on Re- and Si-face of (E)-α-Methyl-4-methoxystilbene).

Table 5.7 presents the energetics of whole conversion in a concise way.

Substrate	***E*** **/Hartrees**	***Δ‡E*** **/kJ mol^{-1}**	***Δ‡G*** **/kJ mol^{-1}**	***ΔE*** **/kJ mol^{-1}**	***ΔG*** **/kJ mol^{-1}**
Reactant-Re	-1430.418437			-154	-149
Product-Re	-1430.477072				
TS-Re	-1430.390905	72	62		
Reactant-Si	-1430.422043			59	44
Intermediate-Si	-1430.399592				
TS-Si	-1430.388471	88	73		
TS2-Si	-1430.398757	2	5		
Product	-1430.480388			-153	-158

Table 5.7 Energies of all the steps involved in hydrogenation of (E)-α-Methyl-4-methoxystilbene.

After studying the complete pathway in gas phase single point calculations for all the steps were done in the presence of solvent (toluene) also to study its effect. Table 5.4 depicts the results of calculations done.

Substrate	***E*** **/Hartrees**	***Δ‡E*** **/kJ mol^{-1}**	***Δ‡G*** **/kJ mol^{-1}**	***ΔE*** **/kJ mol^{-1}**	***ΔG*** **/kJ mol^{-1}**
Reactant-Re	-1430.484027				
Product-Re	-1430.537584			-141	
TS-Re	-1430.45206	84	73		
Reactant-Si	-1430.487556				
Intermediate-Si	-1430.457857				
TS-Si	-1430.44796326	104	89		
TS2-Si	-1430.45690523	3	5		
Product	-1430.5391458			-135	

Table 5.8 Energies of all the steps involved in hydrogenation of (E)-α-Methyl-4-methoxystilbene in solvent (toluene).

Apart from comparing the energetics, enantiomeric excess was also calculated. To begin with the energy difference between two transition states (for Re and Si face respectively) was calculated and then enantiomeric excess was calculated at various temperatures. The plot of ee against temperature is depicted in Figure 5.35. The plot in Figure 5.35 predicts the enantiomeric excess at 298K to be 86%.

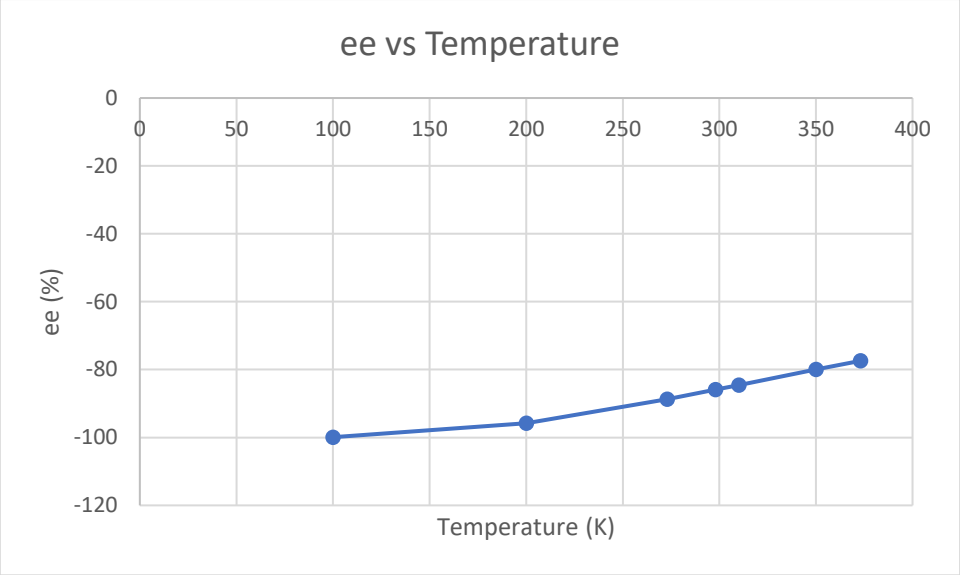

Figure 5.35 Plot of enantiomeric excess (ee) against temperature (K).

5.2.4 Further Analysis

In this study also non-covalent interactions between substrate and FLP were studied by constructing NCI (Non-Covalent Interaction) plots that give an idea about inter- and intramolecular non-covalent interactions in the system. Figure 5.36 represents the NCI plots for hydrogenation via Re/Si face of (E)-α-Methyl-4-methoxystilbene in presence of FLP. NCI Plot indicates differences between transition states, most notably in the interactions of the aromatic ring of the substrate.

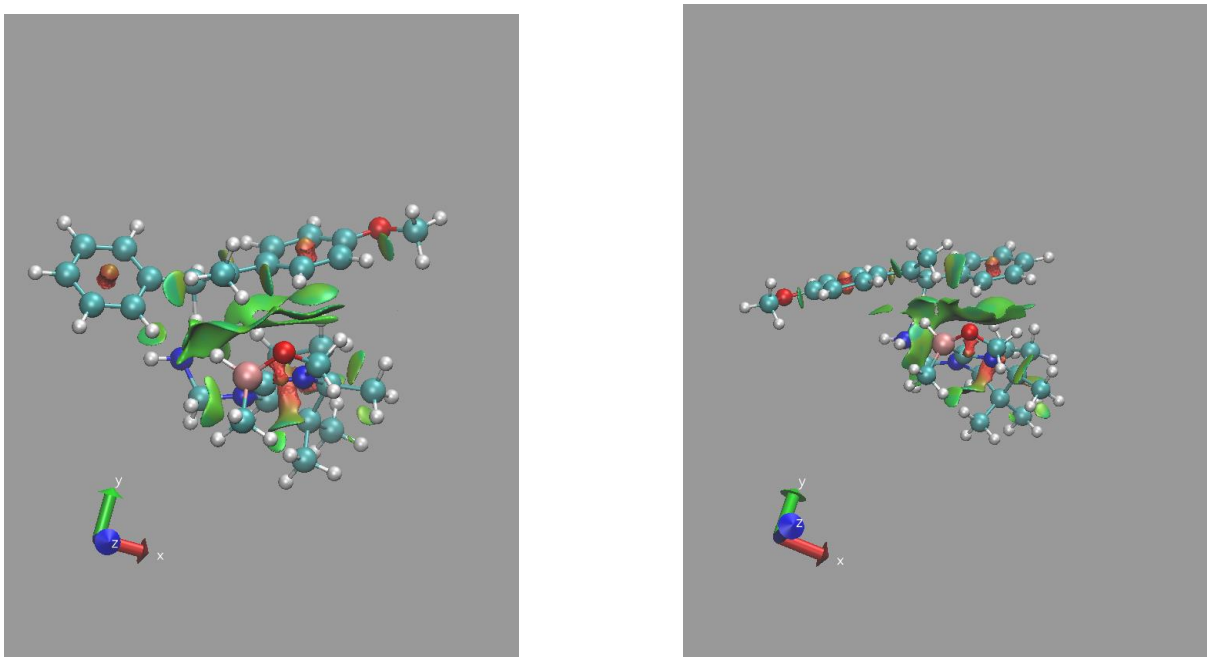

Figure 5.36 NCI plot for TS *via* Re/Si face of (E)-α-Methyl-4-methoxystilbene in presence of FLP.

As in the previous section here also distance between selected groups in Re- and Si-TS were measured to get an idea about the attractive or repulsive interactions that might take place. It was found that in Si-S H is attached with B in FLP comes very close to CH_3 group attached with double bond in substrate (2.1 Å). Similarly C(50), C(51) and C(52) in substrate come quite close to H(39) (2.9 Å), O(14) (2.4 Å) and H(42) in FLP respectively. C(51) in substrate also comes close to H(32) in FLP (2.8 Å).

In the case of Re-TS H attached to NH in FLP (2.6 Å) and H attached to B in FLP (2.3 Å) both come close to H(74) of aromatic ring in the substrate. H attached to B in FLP also comes very close to the H of CH_3 group attached to the double bond in the substrate (2.2 Å). Similarly, O in the FLP comes close to the H of CH_3 group attached to double bond in substrate (2.3 Å). Further, C (52) (2.7 Å) and H (55) (2.4 Å) of in the

aromatic ring attached with methoxy group in the substrate come close to H(42) and H(32) in the FLP respectively.

Si-TS	**Distance /Å**
H(8) (NH in FLP) - C(58) (of aromatic ring with methoxy group in substrate)	3.4
H(37) (H of B in FLP) - C(57) (of aromatic ring with methoxy group in substrate)	3.1
H(8) (NH in FLP) - C(44) (olefinic carbon in substrate)	3.0
H(37) (H of B in FLP) - C(73) (of CH_3 group attached with double bond in substrate)	2.1
H(39) (in FLP) - C(50) (of aromatic ring in substrate)	2.9
H(42) (in FLP) - C(52) (of aromatic ring in substrate)	2.4
O(14) (in FLP) - C(51) (of aromatic ring in substrate)	2.4
H(32) (in FLP) - C(51) (of aromatic ring in substrate)	2.8
Re-TS	
H(8) (NH in FLP) - H(74) (of aromatic ring in substrate)	2.6
H(37) (H of B in FLP) - H(74) (of aromatic ring in substrate)	2.3
H(37) (H of B in FLP) - H(46) (of CH_3 group attached with double bond in substrate)	2.2
O(14) (in FLP) - H(46) (of CH_3 group attached with double bond is substrate)	2.3
H(42) (H in FLP) - C(52) (of aromatic ring attached with methoxy group in substrate)	2.7
H(32) (H in FLP) - H(55) (of aromatic ring attached with methoxy group in substrate)	2.4
H(28) (H of CH_3 group in FLP) - H(61) (H of methoxy group attached to aromatic ring in substrate)	3.5

Table 5.9 Distance between selected groups in Re- and Si-TS

5.3 Conclusions

In this chapter, effort has been made to understand the hydrogenation of prochiral olefins and carbonyl compounds. Acetophenone and stilbene had been chosen as the

representatives of the class. Complete steps for the elucidation of the mechanism were tried from Re- as well as Si face of the substrates. It was found that the reaction was concerted and synchronous. Activation energy for Si- face was a little less than the Re face although this difference was not substantial.

In the case of (E)-α-Methyl-4-methoxystilbene the difference between Re- and Si-face was considerable. The barrier for Re-face was found to lower than the Si-face. Additionally, it was observed that the mechanism was concerted and synchronous for Re-face but in the case of Si-face mechanism was no longer concerted and synchronous. It became stepwise and proceeded *via* an intermediate.

It was also found that both in the case of acetophenone as well as (E)-α-Methyl-4-methoxystilbene Re-face conformer generated product with S-conformation while Si-face conformer gave rise to product with R-conformation.

It is difficult to draw generalizations at this stage as only two prochiral substrates have been studied but it is expected that after studying more prochiral substrates, in the near future we will be able to predict more trends for the whole class. Effort will also be made to understand the regioselectivity in addition to the stereoselectivity that was elucidated in the present study.

5.4 References

1. T. Mahdi and D. Stephan, *Journal of the American Chemical Society*, 2014, 136, 15809-15812.

2. S. Mummadi, A. Brar, G. Wang, D. Kenefake, R. Diaz, D. Unruh, S. Li and C. Krempner, *Chemistry - A European Journal*, 2018, 24, 16526-16531.

Chapter-6 Conclusions and Future Work

In this thesis, we have investigated the catalytic action of FLPs (chiral borenium compounds based on camphor scaffolds) on hydrogenation of olefins and carbonyl and imine compounds using DFT. Myriad of reactions of FLPs that occur with the help of DFT have been discussed at length in Chapter 1. Literature survey revealed that not much work has been done on DFT study of hydrogenation of small molecules by chiral borenium compounds based on camphor scaffolds. Hence it was thought worthwhile to explore the complete mechanism of action of these FLPs.

Initially (Chapter 3), two known borenium compounds which had similar skeleton to our target molecule were selected for preliminary screening of functionals. It was found that M06-2X/6-31G(d) is a functional of choice for this study. BP86/SVP functional was used to calculate HIA and FIA values. In the next phase M06-2X/6-31G(d) functional was employed to model the target compound using various Lewis acid and Lewis base linkers. In the last part of the chapter, the new molecules thus prepared were tested for FLP character. Those molecules which were frustrated Lewis pairs were then selected for the further studies. In the last part of the study, activation of hydrogen by FLPs was studied. In general, it was found that the activation barriers for activation of hydrogen were moderate and high I some cases like pyridine. Simulation of toluene solvent further reduced this barrier. Studies reveal that activation of hydrogen by FLP is a concerted and synchronous reaction.

Next part of the study (Chapter 4) was to explore the potential of activated frustrated FLPs to hydrogenate simple achiral substrates as olefins, imines and carbonyl compounds. Results of the calculations revealed that hydrogenation of olefins as well as carbonyl compounds is concerted and synchronous except imines where the

mechanism is stepwise. In the case of hydrogenation of aldehydes and ketones, the catalyst (FLP) has strong interaction with the product and in some cases, it fails to detach from the final product. All the hydrogenation reactions studied are exothermic in nature and have low to moderate activation barriers which are strongly dependent on the substituents as well as solvent.

The final part of the investigation was an endeavour to understand the hydrogenation of prochiral olefins and carbonyl compounds. The main focus of the study was to explore the stereoselectivity in this reaction which may lead to the formation stereospecific products. It was found that, as in the case of achiral substrates, the overall mechanism was exergonic, concerted and synchronous with moderate activation barriers primarily dependent on the substituents as well as solvent. It was seen found that there was a preference of attack from the less hindered side of the substituent and the products formed as result were also stereospecific. In addition, it was also observed that the reaction became stepwise from the more hindered side of the substrate (Si- face of (E)-α-Methyl-4-methoxystilbene).

The results obtained till now seem quite encouraging. In the near future effort will be made to model these FLPs with even more variety of Lewis acids and Lewis bases to get better catalysts. In the present work it was seen that in the case of some carbonyl compounds FLP was not able to detach from the final product. Hence, in future attempt will be made to design such FLPs which can detach easily form the final product, one way may be by increasing steric bulk at the borenium centre. Further, a computational study[1] on oxazaborolidine[2] (CBS) catalysts have emphasized the importance of THF as a donor solvent. It is found that the release of the product from the catalyst complex is facilitated by an S_N2 displacement of the alcohol as a leaving group by nucleophilic attack of THF on boron. THF may be tried in future to FLP catalysts, although

consideration would need to be given to how coordination of THF to boron would affect the H_2 activation step as well as the product release.

Although the outcomes in Chapter-5 are quite promising but they are based on the study on the study of only two prochiral substrates. Therefore, in the coming times this study will be broadened by employing more prochiral substrates so that generalizations for this mechanism can be drawn.

References

1. L. Linney, C. Self and I. Williams, *J. Chem. Soc., Chem. Commun.*, 1994, 1651-1652.

2. E. Corey and C. Helal, *Angewandte Chemie International Edition*, 1998, 37, 1986-2012.